Taking the Bull by the 'Horns'

Modelling the structure and kinematics of star-forming regions using *Gaia* DR2

by

Graham David FLEMING

A thesis submitted in partial fulfilment for the requirements for the degree of Master of Science (by Research) in Astrophysics at the University of Central Lancashire

Tuesday 8th December, 2020

University of Central Lancashire

Master of Science (by Research) Thesis

Taking the Bull by the 'Horns'

Modelling the structure and kinematics of
star-forming regions using *Gaia* DR2

Author:
Graham David FLEMING

Supervisor:
Dr. Jason KIRK

Second Supervisor:
Prof. Derek WARD-THOMPSON

A thesis submitted in partial fulfillment of the requirements for the degree of Master of Science (by Research) in Astrophysics

in the

Jeremiah Horrocks Institute
School of Natural Sciences

Tuesday 8th December, 2020

Declaration of Authorship

Type of Award: Master of Science (by Research) in Astrophysics

School: Jeremiah Horrocks Institute

I, **Graham David FLEMING**, declare that this thesis titled, "Taking the Bull by the 'Horns'" and the work presented in it are my own and was completed wholly whilst in candidature for a research degree at the University of Central Lancashire. In addition:

1. Concurrent registration for two or more academic awards. I declare that while registered as a candidate for the research degree, I have not been a registered candidate or enrolled student for another award of the University or other academic or professional institution.
2. Material submitted for another award. I declare that no material contained in the thesis has been used in any other submission for an academic award and is solely my own work.
3. Previously published works. Some of the work presented in this thesis has been submitted for publication by the author (Fleming, Kirk, and Ward-Thompson, 2019).
4. Collaboration. Where the thesis is based on work done by myself jointly with others, I have made clear exactly what was done by others and what I have contributed myself. I have acknowledged all main sources of help.
5. Referencing previous works. Where I have consulted the published work of others, this is always clearly attributed. Also, where I have quoted from the work of others, the source is always given. With the exception of such quotations, this thesis is entirely my own work.
6. Use of a Proof-reader. No proof-reading service was used in the compilation of this thesis.

Signed: G Fleming

Print Name: Graham David Fleming

Date: Tuesday 8th December, 2020

Supervisor's Declaration

I, **Dr. Jason KIRK**, as supervisor, hereby declare that this thesis titled, "Taking the Bull by the 'Horns'" written by Graham David FLEMING, is his own writing prepared under my supervision and that I supported his work with regular consultations.

I confirm that to the best of my knowledge, Graham David FLEMING has carried out his research according to the University of Central Lancashire requirements for a Master's degree.

I also declare that, based on its professional merits, the thesis meets the formal and professional requirements of the University of Central Lancashire and those of the Jeremiah Horrocks Institute, I therefore support its submission.

Signed: ______________________________

Print Name: Jason M. Kirk

Date: Tuesday 8th December, 2020

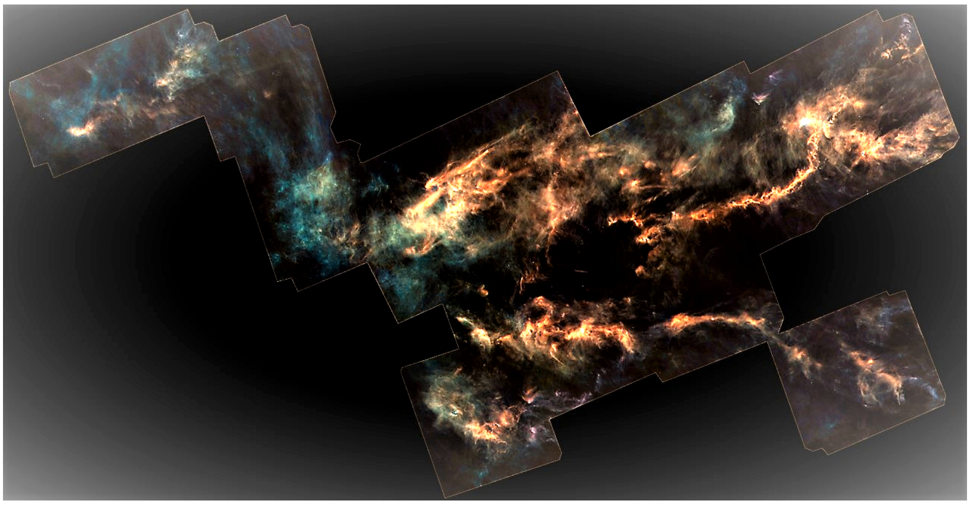

Figure 1 *Herschel*'s infrared view of the Taurus Molecular Cloud.
Image: http://sci.esa.int/jump.cfm?oid=59536. © ESA/Herschel/NASA/JPL-Caltech.

"I've been studying the Taurus Molecular Cloud for decades, and I had no idea I was looking at two clouds, one behind the other – we've never before had a three-dimensional view of anything so distant."

Derek WARD-THOMPSON (June 2019)

UNIVERSITY OF CENTRAL LANCASHIRE

Abstract

Jeremiah Horrocks Institute

School of Natural Sciences

Master of Science (by Research) in Astrophysics

Taking the Bull by the 'Horns'

by Graham David FLEMING

The Taurus Molecular Cloud (TMC) is a star forming region, containing all stages of pre-main sequence stellar types, lying at an accepted distance of approximately 140 parsecs from Earth, spread across the Taurus and Auriga constellations. This cloud has been extensively studied and is known to contain hundreds of young stellar objects in the form of deeply embedded protostars displaying disks and outflows, classical and weak-lined T Tauri stars, Herbig-Haro objects and low-mass brown dwarfs.

By using data obtained from the European Space Agency's *Gaia* space observatories second data release (DR2), an area of sky of 10°x15°, centred on right ascension (J2000.0)=68.5° and declination (J2000.0)=27.0° is studied, this being an area surrounding the Taurus molecular cloud. A preliminary investigation of a small sample of objects previously identified in the *Spitzer* catalogue found two main associations, hitherto unrecognised, centred at 130±6 pc and 160±4 pc at 1σ which also have different proper motions, of 24.5±2.8 and 20.1±2.4 mas yr^{-1} respectively. These associations are here named the 'Two Horns' of Taurus.

Applying the same procedures as those used in our preliminary study a sample of *Gaia* optical sources are investigated using quality filters identified in the literature. The existence of two populations at a mean distance of 139.7 pc centred on 130±3 pc and 159±12 pc at 1σ standard deviation is confirmed. These 'near' and 'far' groups are found to have proper motions of 25.2±3.4 and 22.1±4.5 mas yr^{-1} respectively at 1σ.

Using data from *Gaia* DR2, two previously unidentified populations of Young Stellar Objects are identified in the Taurus Molecular Cloud. This study investigates the positions, classifications, ages and kinematics of these groups and 3-dimensional visualizations of these populations are presented.

Publications and Conferences

Paper Title: Revealing the Two 'Horns' of Taurus with *Gaia* DR2. Pre-print submitted to arXiv https://arxiv.org/abs/1904.06980. 16th April 2019.

STARRY Final Conference: *Gaia*'s view of Pre-Main Sequence Evolution - Linking the T Tauri and Herbig Ae/Be stars. Weetwood Hall, Leeds, UK. 18th - 21st June 2019. **Presentation Title:** Revealing the Two 'Horns' of Taurus with *Gaia* DR2. A copy of the presentation can be found at https://starry-project.eu/final-conference/programme/.

National Astronomy Meeting (NAM2019): Lancaster University, Lancaster, UK. 30th June - 4th July 2019. **Poster presentation:** Revealing the Two 'Horns' of Taurus with *Gaia* DR2. A copy of the poster can be found at https://lancaster.app.box.com/v/nam2019-posters/file/486068363251.

Acknowledgements

I would like to express my sincere gratitude to my supervisor Doctor Jason Kirk for his sustained support throughout the course of my research. His patience and guidance have helped on numerous occasions. Also, to Professor Derek Ward-Thompson who has given me encouragement and advice during the completion of my studies. I would also like to acknowledge the invaluable collaborative support given by Dr. Kate Pattle in providing the underlying `Python` code used in the analysis of our data using Hartigans' Dip Test (Section 3.2.1) and in her contribution to Section 3.4.3.

I also express my gratitude to Dr. Nigel Hambly of the Royal Observatory, Edinburgh and member of the European Space Agency's Gaia mission Data Processing and Analysis Consortium (DPAC) for his in-depth knowledge of the *Gaia* Archive and how to access it through the use of ADQL queries.

This work has used the NASA Astrophysics Data System (ADS) Bibliographic Services[1] as well as the VizieR catalogue access tool[2] and SIMBAD astronomical database[3], operated at CDS, Strasbourg, France.

During the early stages of this study I was grateful to be able to use the online *UVW Calculator*[4] created by David Rodriguez, UCLA (2010). Celestial coordinate conversions have been made using the online *RA DEC flexible converter*[5] provided by Jan Skowron at the Warsaw University Observatory.

Data products have been used from the European Space Agency (ESA) mission *Gaia*[6], processed by the *Gaia* Data Processing and Analysis Consortium (DPAC)[7]. Funding for the DPAC is provided by national institutions, in particular the institutions participating in the *Gaia* Multilateral Agreement.

Use has also been made of data from the Two Micron All Sky Survey, which is a joint project of the University of Massachusetts and the Infrared Processing and Analysis Center/California Institute of Technology, funded by the National Aeronautics and Space Administration and the National Science Foundation. Data from the Guoshoujing Telescope (the Large Sky Area Multi-Object Fiber Spectroscopic Telescope) has been used in Section 4.4.1. LAMOST is a National Major Scientific Project built by the Chinese Academy of Sciences. Funding for the project has been provided by the National Development and Reform Commission. LAMOST is operated and managed by the National Astronomical Observatories, Chinese Academy of Sciences.

[1] http://ads.harvard.edu/
[2] http://vizier.u-strasbg.fr/viz-bin/VizieR
[3] http://simbad.u-strasbg.fr/simbad/
[4] http://www.astro.ucla.edu/ drodrigu/UVWCalc.html
[5] http://www.astrouw.edu.pl/ jskowron/ra-dec/
[6] https://www.cosmos.esa.int/gaia
[7] https://www.cosmos.esa.int/web/gaia/dpac/consortium

Contents

List of Figures

Page

List of Tables

List of Abbreviations

ADQL	**A**stronomical **D**ata **Q**uery **L**anguage
AGB	**A**symptotic **G**iant **B**ranch
AU	**A**stronomical **U**nit
BaSTI	a **Ba**g of **S**tellar **T**racks and **I**sochrones
CMD	**C**olour **M**agnitude **D**iagram
CTTS	**C**lassical **T** **T**auri **S**tar
CU	**C**ordination **U**nit
Dec	**Dec**lination
DPAC	**D**ata **P**rocessing and **A**nalysis **C**onsortium
ESA	**E**uropean **S**pace and **A**gency
FCRAO	**F**ive **C**ollege **R**adio **A**stronomical **O**bservatory
Gaia	**G**lobal **A**strometric **I**nterferometer for **A**strophysics
GUI	**G**raphical **U**ser **I**nterface
HDS	**H**artigan **D**ip **S**tatistic
Hipparcos	**HI**gh Precision **PAR**allax **CO**llecting **S**atellite
HMC	**H**ot **M**olecular **C**ore
IAU	**I**nternational **A**stronomical **U**nion
ICRS	**I**nternational **C**elestial **R**eference **S**ystem
IMF	**I**nitial **M**ass **F**unction
IRAM	**I**nstitut de **R**adio**a**stronomie **M**illimétrique
JD	**J**ulian **D**ate
LAMOST	**L**arge Sky **A**rea **M**ulti-**O**bject Fiber **S**pectroscopic **T**elescope
LSR	**L**ocal **S**tandard of **R**est
MESA	**M**odules for **E**xperiments in **S**tellar **A**strophysics
MS	**M**ain **S**equence
NGP	**N**orth **G**alactic **P**ole
PARSEC	**Pa**dova and T**R**ieste **S**tellar **E**volution **C**ode
PMS	**P**re-**M**ain **S**equence
RA	**R**ight **A**scension
RVS	**R**adial **V**elocity **S**pectrometer
SED	**S**pectral **E**nergy **D**istribution
SGP	**S**outh **G**alactic **P**ole
SIMBAD	**S**et of **I**dentifications, **M**easurements and **B**ibliography for **A**stronomical **D**ata
SQL	**S**tructured **Q**uery **L**anguage
TCB	**B**arycentric **C**oordinate **T**ime
TDB	**B**arycentric **D**ynamic **T**ime
TMC	**T**aurus **M**olecular **C**loud
TMR	**T**aurus **M**olecular **R**ing

TT	**T**errestrial Dynamic **T**ime
UTC	**C**oordinated **U**niversal **T**ime
VLBA	**V**ery **L**ong **B**aseline **A**rray
WTTS	**W**eak-line **T** **T**auri **S**tar
YaPSI	**Ya**le-**P**otsdam **S**tellar **I**sochrones
YSO	**Y**oung **S**tellar **O**bject

Physical Constants & Definitions

arcsecond	$'' = 1/3600$ of a degree
Astronomical Unit	AU $= 149.5978 \times 10^{9}\,\mathrm{m}$
Parsec	pc $= 30.8567 \times 10^{15}\,\mathrm{m}$
Speed of Light	$c_0 = 299.7924 \times 10^{6}\,\mathrm{m\,s^{-1}}$

List of Symbols

b	Galactic latitude	deg
l	Galactic longitude	deg
z	Redshift	[unit-less]
V_{LSR}	Line-of-sight Velocity	$\mathrm{km\,s^{-1}}$
α	Right ascension (RA)	hh:mm:ss and deg
δ	Declination (dec)	deg
π	parallax	arcsecond

To those who have supported and encouraged me on this journey and have helped prove that it is never to late to learn . . .

1 INTRODUCTION

1.1 The Taurus Molecular Cloud

The Taurus Molecular Cloud (TMC) lies in the constellations of Taurus and Auriga and contains hundreds of newly formed stars (e.g. Luhman et al., 2009b). If you can see it at all, seen in visible light the TMC appears unremarkable. It is cool, dark and scarcely visible at optical wavelengths, even when using telescopes (Figure 1.1a) due to the fact that there are no large stars embedded in the cloud which can illuminate it.

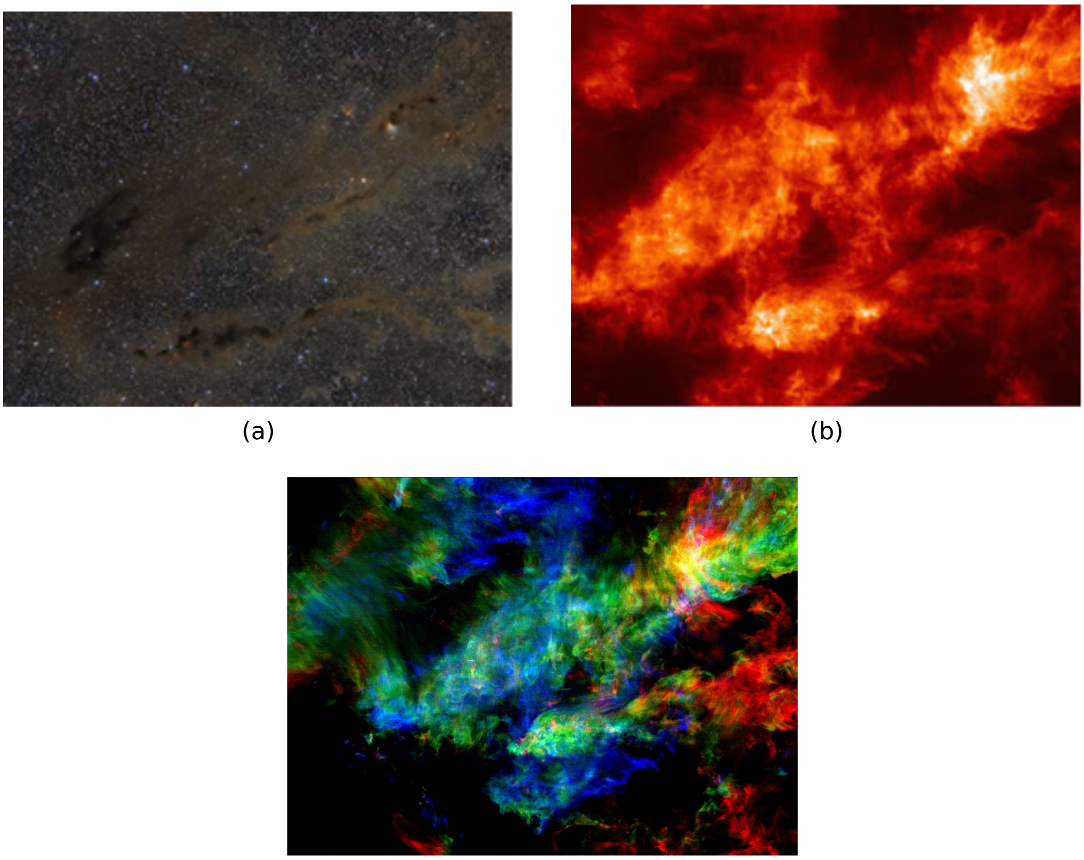

(a) (b) (c)

Figure 1.1 The Taurus Molecular Cloud. (a) In visible light. From: http://www.astrobin.com/228813/. © Tommy Nawratil, 2015. (b) At infrared wavelengths. Image Credit: FCRAO, Gopal Narayanan / Mark Heyer. (c) 3-colour image of ^{12}CO (J=1→0) emission highlighting complex gas motions within the cloud (see text). From: Dobbs et al. (2014: Figure 1).

In contrast, observatories, and especially space-based telescopes, equipped with infrared detectors see much more detail and star-forming activity becomes obvious (Figure 1.1b). Figure 1.1c shows a 3-colour ^{12}CO (J=1→0) emission image of the same region (Narayanan et al., 2008;

Dobbs et al., 2014) integrated over velocity dispersion V_{LSR} intervals of 0–5 km s^{-1} (blue), 5–7.5 km s^{-1} (green), and 7.5–12 km s^{-1} (red), illustrating the complex velocity fields within the Taurus cloud.

The TMC is one of the closest low-mass star-forming regions, lying at a commonly accepted distance of about 140 pc (Elias, 1978). The region covers some 10 to 15 degrees in extent which equates to about 25 to 30 pc at this distance. This makes comprehensive studies of the entire stellar population of the region difficult and few exhaustive studies of the three-dimensional structure of the cloud complex have previously been conducted (e.g. Luhman, 2018). Situated within the TMC are numerous filaments and smaller cloud structures (Hartmann, 2002; Schmalzl et al., 2010; Kirk et al., 2013; Panopoulou et al., 2014; Marsh et al., 2016). Previous studies have shown that young stars are grouped in and around these smaller structures (Gomez et al., 1993; Kirk et al., 2013). Early distance measurements (McCuskey, 1939) determined a distance of 142 pc to the Taurus star-forming region, whilst later studies (Straizys and Meistas, 1980; Meistas and Straizys, 1981) of a number of Lynds dark clouds in the region (Lynds, 1962) indicated that the TMC is more extended and exists between about 140 and 175 pc.

1.1.1 Evidence for star formation in the TMC

Young stars form in hot molecular cores (HMCs), which are dense condensations of gas with complex chemistries located within molecular clouds. There is strong evidence to suggest that active star formation, in all its stages, is ongoing throughout the TMC.

Studies of chemical structures within the TMC, associated with the star formation process, have identified warm water vapour (Rivière-Marichalar et al., 2012) and water vapour associated with a cold pre-stellar core within the Lynds 1544 cloud (Caselli et al., 2012). Complex organic molecules including HCnN, CH_3CHO, H_2CCO, and H_2CO have been identified (Freeman and Millar, 1983; Soma et al., 2018), indicating that such molecules can form during the early evolutionary stages of starless cores. Complementary studies of ^{13}CO (J=1$\rightarrow$0) emissions seen in the region (Qian, Li, and Goldsmith, 2012) indicate that molecular cores can condense out of the diffuse ambient gas without additional energy input from nearby stars.

The TMC contains hundreds of newly formed stars and embedded protostars (e.g. Kenyon et al., 1994; Sheehan and Eisner, 2017) which posses massive disks and which are a clear indication of star formation. There are low-mass classical and weak-lined T Tauri stars (Scelsi et al., 2007) undergoing gravitational collapse (Figure 1.2) and newly born Herbig-Haro objects (Sun et al., 2003) displaying directional jets of ejected material as well as numerous brown dwarfs (Grosso et al., 2007) which have not reached the critical mass for hydrogen fusion to be sustained.

Figure 1.2 The 10.5-magnitude pre-main sequence star T Tauri (upper left of picture), surrounded by its reflection nebula and dust cloud with a bright 8th-magnitude field star 7′ to the southwest. From: http://www.caelumobservatory.com/gallery/n1555.shtml. Image Credit: Adam Block, Mt. Lemmon Sky Survey, University of Arizona.

Using the Atacama Large Millimeter Array (ALMA) in Chile, a survey of young stars with protoplanetary discs in the Taurus star-forming region (Long et al., 2018), has shown that ∼40% of such stars contain rings, gaps and structures associated with the presence of embryonic planets. Also, the mass measurement of a number of Class I protostars in the TMC (Sheehan and Eisner, 2017) has been able to constrain the initial mass budget available for planet formation in the early stages of protoplanetary disk evolution.

Such studies, ranging from the early formation of protostars through to the development of planetary objects, in such a nearby star-forming region, indicate the importance of the TMC in this field of research.

1.1.2 Contextualising this study

There have been many investigations into the structure, stellar composition and kinematics of the Taurus cloud complex. The investigation of early-type O and A stars located in the Taurus-Auriga molecular cloud (Mooley et al., 2013) within 1σ parallax error of 6.2<π<7.8 milli-arcsec (128 to 162 pc), identified a significant number of previously unidentified A5 or earlier stars within the region. Mooley et al. (2013) also noted in their study that even their new distribution fell far short of the expected number of such stars if a standard log-normal IMF distribution applies to the region, adding to the discussion previously noted by Goodwin, Whitworth, and Ward-Thompson (2004) and other researchers (e.g. Kraus et al., 2017).

Comprehensive surveys of the TMC have been conducted by the *Spitzer* space telescope at submillimetre and infrared wavelengths (Nutter et al., 2008) and by *Chandra* and *XXM-Newton* in the X-Ray (Güdel, Padgett, and Dougados, 2006; Güdel et al., 2007). Observations at radio wavelengths have also been conducted using the Giant Metrewave Radio Telescope (GMRT) (Ainsworth et al., 2016) and the Five College Radio Astronomy Observatory (FCRAO) (Narayanan et al., 2008). These wide-field surveys have provided high resolution images of the molecular cloud and valuable insights into the distribution of the molecular gas and star forming regions within the cloud. More specific studies have investigated the radial velocities of pre-main sequence stars (Kraus et al., 2017) as well as the distribution of low-mass stars (Hartmann, 2002) in the region.

Bertout and Genova (2006) derived kinematic parallaxes of 67 members of the Taurus moving group with typical errors of 20% and identified weak-line and classical T Tauri stars spread over distances between 106^{+42}_{-24} and 259^{+61}_{-42} pc. Very Long Baseline Array (VLBA) parallax observations of individual stars (Torres et al., 2007; Torres et al., 2009) identified differences in distance to separate star-forming regions of the Taurus complex. They noted a distance of 161.2$\pm$0.9 pc for the star HP Tau/G2 and 146$\pm$0.6 pc for T Tau (Loinard et al., 2007) in the eastern part of the complex, and 130 pc to the central area of the star-forming complex, by observing the T Tau-type stars Hubble 4 (V* V1023 Tau) at 132$\pm$0.5 pc and HDE 283572 at 128.5$\pm$0.6 pc. A multi-wavelength photometric study of the Taurus region (Gudel, Padgett, and Dougados, 2007) using the Canada-France-Hawaii-Telescope, *Spitzer* and *XMM-Newton* data produced maps detailing the stellar and substellar distribution of the region. In a similar investigation, pre-main sequence members of the Taurus molecular clouds were identified (Rebull et al., 2010) using the *Spitzer* Space Telescope Taurus project (SSTtau) catalogue (http://cds.u-strasbg.fr/cgi-bin/Dic-Simbad?SSTtau) and Two-Micron All-Sky Survey (2MASS) data located at http://vizier.u-strasbg.fr/cgi-bin/VizieR?-source=B/2mass. This survey informs the findings of our own preliminary study presented in Section 3.1.

Galli et al. (2018) presented trigonometric parallax and proper motion observations of Young Stellar Objects (YSOs) in the Taurus region as part of the Gould Belt Distances Survey using the VLBA. Their data suggest a significant difference between the closest and farthest stars in their sample of about 36 pc with the closest lying at 126.6$\pm$1.7 pc and the most distant at 162.7$\pm$0.8 pc. The more recent comparison of *Gaia* DR2 and VLBI astrometry results (Galli et al., 2019) revise these distances but again confirm the existence of significant depth effects within the TMC.

As a successor to the successful *Hipparcos* astrometry mission to accurately measure the positions of celestial objects, the *Gaia* space telescope, launched in 2013, is designed to measure the parallaxes and proper motions of astronomical objects. *Gaia*'s second data release (DR2), based on 22 months of observations, happened on 25 April 2018. This data release contains five-parameter astrometric solutions detailing positions, proper motions and parallaxes for approximately 1.3 billion stars (Brown et al., 2018) and will present a significant increase in the accuracy of such measurements.

1.1.3 Contemporary studies

Studies of the TMC using *Gaia* DR2 data (Luhman, 2018; Esplin and Luhman, 2019) present comprehensive studies of the stellar membership of the Taurus region. In both studies extensive reference is made to earlier studies (e.g. Esplin and Luhman, 2017; Galli et al., 2018) with regard to the stellar membership of specific cloud complexes and the kinematics of their members. Proper motions, parallaxes and radial velocity data from *Gaia* DR2 is used in discussions identifying new members of the star-forming region. Within the census of members identified in Luhman (2018), the author finds no evidence for an older population of stars previously identified by Kraus et al. (2017) and Zhang et al. (2018). The study does however support the existence of a possible moving group of stars at a distance of 116 to 127 pc with ages of $\sim$40 Myr first identified in the *Gaia* DR1 data by Oh et al. (2017). Luhman (2018) also identifies two distinct populations of stars with proper motions and distances that are consistent with members of the Taurus group, one with ages within the range of known members ($\leq$10 Myr) and another with older members ($\geq$40 Myr). It is suggested that the older population consists of field stars not related to the Taurus clouds.

The precision and depth of data provided in the DR2 release allows for an investigation of the Taurus molecular cloud with new levels of accuracy.

In this study we use the newly available data from *Gaia*'s second data release (DR2) to identify all objects within a 15 x 10 degree region of the TMC within a depth of 100 parsecs. An examination of this data will present spatial velocities and Galactic space velocities for all objects with stated radial velocities. Transverse velocities and proper motions will be identified as the kinematic properties of objects within the various clouds and structures of the TMC, to show the relative motions of these regions within the larger cloud structure. The relative depths of objects within the TMC will be identified and, through the use of 3-D graphical representations, making use of the unprecedented accuracy of the *Gaia* parallax measurements, this study will better constrain the boundaries of the Taurus star-forming region and the objects within it (e.g. Brown et al., 2018; Luhman, 2018) and give perspective to the infrared structure of the TMC shown in Figure 1.1. Where our studies overlap, we will compare our findings to previous studies of the TMC (e.g. Luhman, 2018; Esplin and Luhman, 2019; Galli et al., 2019).

Some of the underlying concepts discussed above and presented later in this study can be found in Appendix F.

2 *GAIA*

The European Space Agency *GAIA* (Global Astrometric Interferometer for Astrophysics) space observatory (Lindegren and Perryman, 1996) was launched in December 2013. The spacecraft is designed to measure the parallax, positions and proper motions of stars, with the ambitious goal of producing a three-dimensional map of most of our Galaxy.

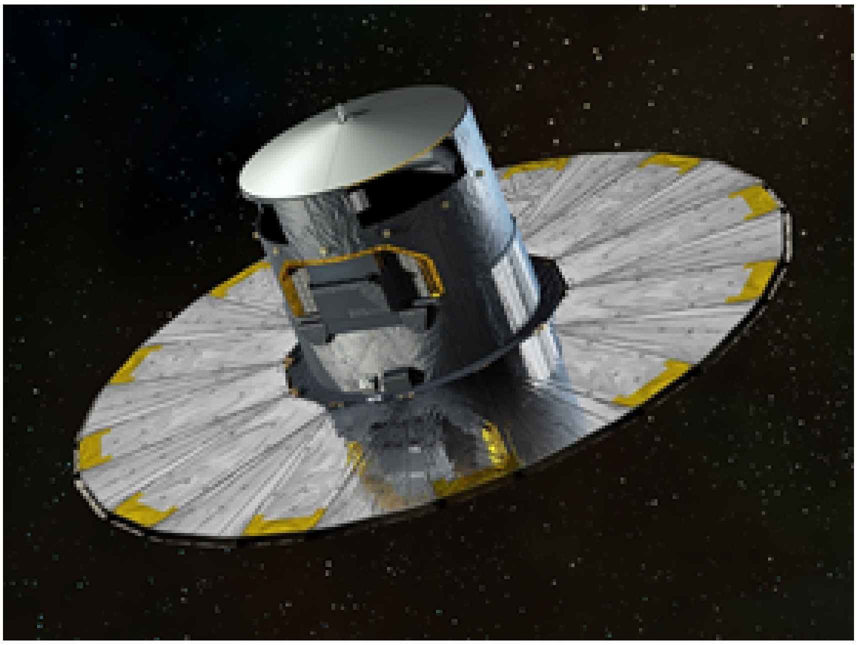

Figure 2.1 Artists impression of the *Gaia* space telescope.
Anon., 2016. *Gaia*. [online]. [Accessed 24 Jul 2019]. Available from: https://gaia-mission.cnes.fr/en/GAIA/index.htm.

The *Gaia* (Figure 2.1) mission design builds on its successful predecessor *Hipparcos* , which operated between 1989 and 1993. The *Hipparcos* catalogue (e.g. Perryman et al., 1997) was released in 1997 and contained the parallax, positions and proper motions of nearly 120,000 stars to an accuracy of about 0.001 arcseconds out to distances of approximately 92 pc.

Although very similar in their mission, the science payloads of *Hipparcos* and *Gaia* differ significantly. Whereas *Hipparcos* carried a single Schmidt telescope and employed a beam-combining mirror to superimpose two fields of view, 59 degrees apart, onto a common focal plane, *Gaia* uses two telescopes with individual fields of view separated by a large angle (the Basic Angle) (Mora et al., 2014) of 106.5°, which enables the sky to be systematically scanned (Figure 2.2), producing large-scale accurate measurements of absolute stellar distances through the determination of trigonometric parallax angles (Section F.2.2).

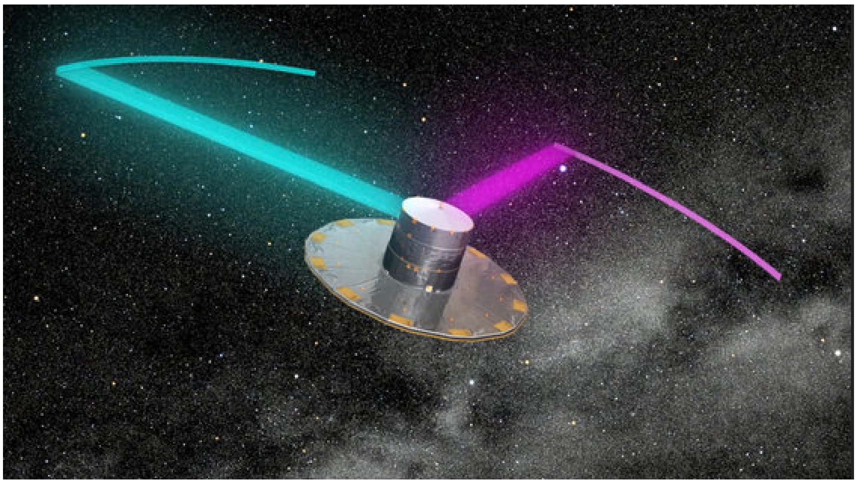

Figure 2.2 The spinning *Gaia* telescopes continually scan two different areas of the sky, registering the position and brightness of each object. Anon., 2016. *Gaia* | *Nova*. [online]. [Accessed 31 Jul 2019]. Available from: http://nova-astronomy.nl/gaia/.

The measurement of an object's distance through the use of parallax is not as straight forward as Figure F.3 might suggest though. From Figure F.4 it might be expected that the motion of a star against the sky would appear as a straight line between two points. But there are practical issues which prevent this from being the case:

1. The Sun moves through the Galaxy in much the same way that the Earth moves around the Sun.
2. The distant background (reference) stars have their own relative motions with respect to the Sun-Earth system causing them to move across the sky during the time it takes *Gaia* to make successive parallax measurements.
3. Since the Sun and the distant star both orbit around the centre of the Galaxy there will also be an apparent, slow, drift across the sky.
4. The star being observed has its own intrinsic 'random' velocity.
5. There is also a small effect due to the gravitational effect of Solar System bodies causing deflections in the light from distant objects due to General Relativity.

Note that items 1 to 3 above contribute to what is known as an objects **proper motion**. All of these effects cause disturbances in the apparent motion of an object as seen by *Gaia*, and other astrometric observatories such as *Hipparcos*. Figure 2.3 shows the overall effect for the star Vega, as seen by *Hipparcos*. The resultant observed motion is a combination of the linear drift due to proper motion and a 'yearly' cyclical corkscrew effect due to parallax which can be in the order of tens or hundreds of milliarcseconds in size. *Gaia*'s positional measurement accuracy of 24 microarcseconds (https://sci.esa.int/web/gaia/-/47354-fact-sheet), as opposed to *Hipparcos*'s positional accuracy of 2 milliarcseconds (https://sci.esa.int/web/hipparcos/-/47357-fact-sheet) is sufficient to resolve this effect and provide accurate measurements of stellar position.

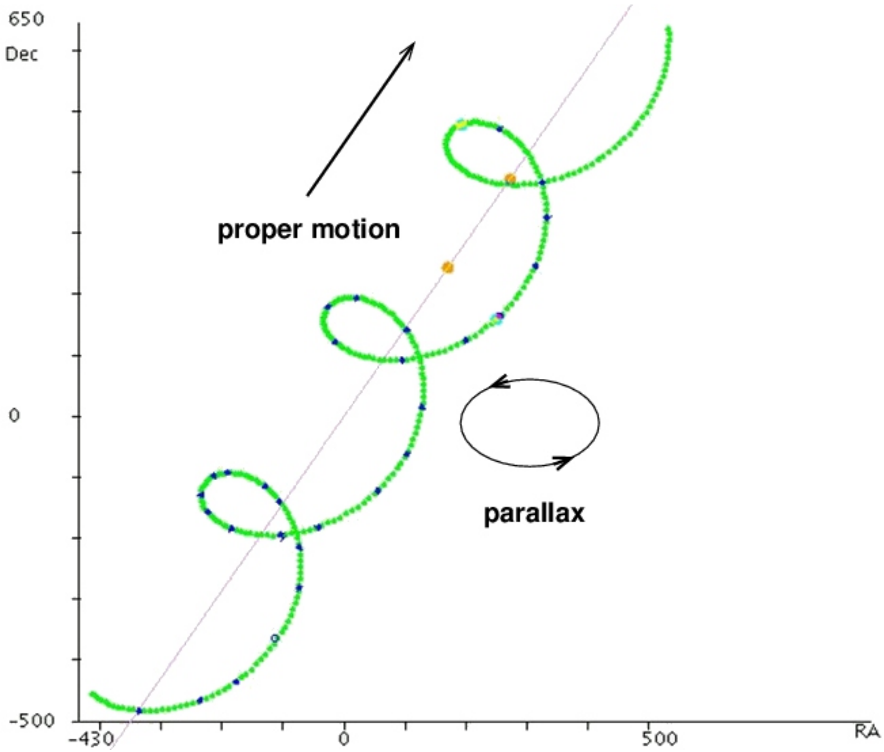

Figure 2.3 The 'real' motion of the star Vega over a 3-year period as viewed by the *Hipparcos* observatory. The straight line shows the object's barycentric motion viewed from the solar system barycentre, the green line shows the observed effect of parallax. Image modified by author from original by: Michael Richmond. 2014. *Vega motion*. [online]. [Accessed 24 Feb 2020]. Available from: http://spiff.rit.edu/classes/phys301/lectures/parallax/parallax.html.

The determination of stellar distance is fundamental to understanding many astronomical phenomena. The use of the parallax method of determining distance for objects not in our immediate solar neighbourhood, from ground-based telescopes, is problematic due to the fact that the Earth's atmosphere limits the sharpness (resolution) of stellar images. Ground-based radio interferometric observations made with instruments such as the Very Long Baseline Array, operated by the National Radio Astronomy Observatory, obtain trigonometric parallaxes of nearby stars with an accuracy often better than 1% (Galli et al., 2018). Even with such instruments, parallax measurements are time and labour-intensive and not conducive to the measurement of a large number of stars. As a result, ground-based astrometric observations are limited to the measurement of distances to about 100 parsecs or less (a parallax angle of 0.01 arcseconds).

Using space-based telescopes can reduce the measurable parallax angle to around 1 milliarcsecond (mas). The *Hipparcos* space telescope improved position accuracies by a factor of 100 compared to typical ground-based results (Eyer et al., 2011).

From its position 1.5 million km beyond Earth's orbit, at the L2 Lagrangian point (Figure 2.4), *Gaia* is able to determine the position of stellar objects with an astrometric precision of up to 0.00001 arcseconds depending on the colour of the star. *Gaia* can determine the distance to stars out to approximately 9,200 parsecs (https://www.esa.int/Science_Exploration/Space_Science/Gaia/Gaia_factsheet) away, about one hundred times farther than *Hipparcos* which could measure out to only about 92 parsecs (https://cerncourier.com/a/gaia-compiles-largest-ever-stellar-survey/). Initial published values for the formal errors on the parallaxes (Katz and Brown, 2017) give G-band values of 30μas at G=15, 150μas at G=18 and 700μas at G=20.

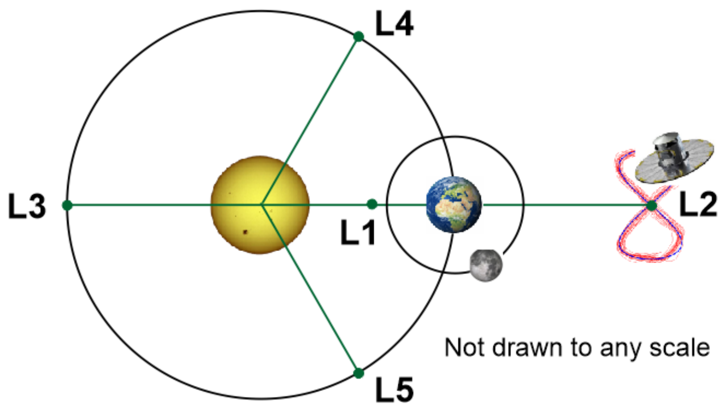

Figure 2.4 *Gaia* operates approximately 1.5 million miles from Earth at the second Lagrange point (L2), along the Sun-Earth line. *Gaia* prescribes a Lissajous orbit within L2 which is an unstable region of null-gravity where spacecraft can be maintained in orbit, over a number of years, using small economical manoeuvres. Credit: Author, 2019.

Gaia's aim is to measure the three-dimensional spatial and velocity distribution of approximately 1 billion (10^9) astronomical objects and to determine their astrophysical properties (Prusti et al., 2016). *Gaia* will do this by repeatedly surveying the sky and identifying the location of all objects down to a G-band magnitude of $\sim$ 20. The satellite reference frame known as the Gaia Celestial Reference Frame (Gaia-CRF2), is aligned with the International Celestial Reference System (ICRS). Gaia-CRF2 (Mignard et al., 2018) uses the accurate positions of 556,869 extragalactic sources (quasars) with a mean density of 10 quasars per square degree as a non-rotating full sky optical reference frame, with an accuracy within 0.15 mas yr^{-1} (Lindegren et al., 2018).

2.1 *Gaia*'s science payload

As mentioned, *Gaia*'s payload contains two triple-mirror telescopes sharing a common focal plane, each pointing through an aperture in the payload housing, separated by an extremely stable basic angle of 106.5°. The telescopes scan the sky as the satellite rotates about its axis, completing one revolution every 6 hours. The light from these instruments is fed into three main science instruments (Prusti et al., 2016).

The telescopes and science instruments are all built around an hexagonal optical bench, approximately 3 m in diameter, which provides the structural support (Figure 2.5).

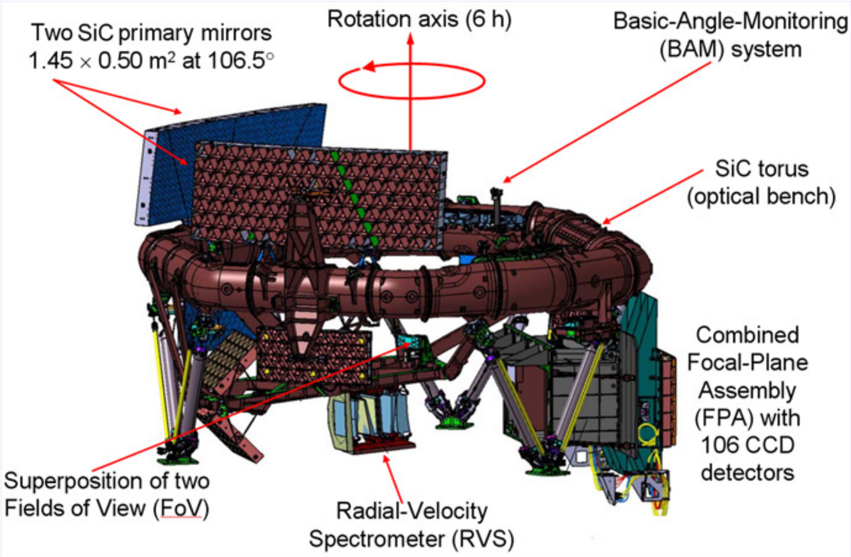

Figure 2.5 *Gaia*'s optical bench showing the mirrors of the two telescopes and the science instruments mounted on an hexagonal optical bench. Anon., 2014. *The payload | Gaia in the UK*. [online]. [Accessed 31 Jul 2019]. Available from: https://www.gaia.ac.uk/mission/payload.

In brief, the science instruments consist of:

- The **astrometric** instrument which measures stellar positions on the sky (Lindegren, 2005). Data is collected in the white-light G-band at 330 – 1050 nm. By integrating all the measurements made of a particular object, over the lifetime of the mission, it will be possible to accurately infer its parallax and thus its distance. In addition, the relative change in the position of the object between measurements can be used to determine its velocity as it moves across the plane of the sky.

- Low resolution spectrophotometric measurements are made using the **photometric** instrument (Riello et al., 2018). Colour information for astronomical objects is generated by Red (RP) and Blue (BP) prism photometers over the optical wavelength ranges 630 – 1050 nm and 330 – 680 nm respectively. These data will be used to determine major properties such as the temperature, mass and chemical composition of objects.

- The **radial velocity spectrometer** (Cropper et al., 2018) is a near-infrared medium-resolution ($\lambda/\Delta\lambda \sim$ 11,500), integral-field spectrograph operating in the range 845 – 872 nm. RVS measurements are used to determine the velocity of an object, along the line of sight, by measuring its Doppler shift using absorption lines in a high-resolution spectrum covering a narrow wavelength range.

2.2 Data Processing and Presentation

Data processing and its presentation falls under the remit of 9 distinct Coordination Units (CUs) which comprise the *Gaia* Data Processing and Analysis Consortium (DPAC)[1]. The DPAC is funded through national funding agencies of the participating ESA member states. The consortium (Figure 2.6) has the responsibility to develop and execute the processing algorithms which turn the raw telemetry from *Gaia* into the final scientific data products which are made available to the research community.

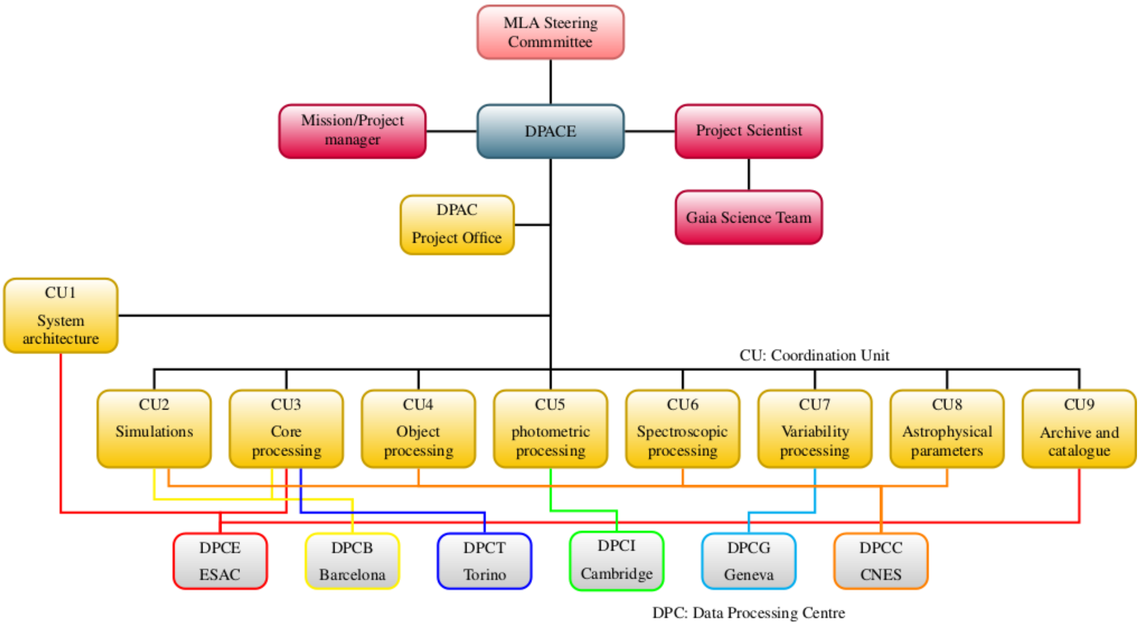

Figure 2.6 The DPAC is structured around specialized sub-units know as Coordination Units (CUs), each responsible for developing the scientific algorithms and software for a specific sub-system of the Gaia data processing system. Software developed by the CUs is run by one of the specialist data processing centres (DPCs). Anon., 2013. *dpac-organigram*. [online]. [Accessed 02 Aug 2019]. Available from: https://www.cosmos.esa.int/web/gaia/dpac.

The ultimate objective of the DPAC is to produce the *Gaia* Catalogue. Prior to the full catalogue release, data catalogues are to be released periodically throughout the mission lifetime. Data Release 1 (DR1), released on 14 September 2016 contained data collected between 25 July 2014 and 16 September 2015. This data release did not represent a complete survey, for a summary of the limitations of DR1 see Brown et al. (2016).

Gaia Data Release 2 (DR2), upon which this study is based, was released on 25 April 2018. DR2 data represents data collected between 25 July 2014 and 23 May 2016 and has a reference epoch of J2015.5 (see Appendix F.2.1). Source positions and proper motions are referred to the ICRS as described

[1] https://www.cosmos.esa.int/web/gaia/dpac

above. Brown et al. (2018) contains a comprehensive summary of the survey properties and contents of DR2.

The third data release is currently due to be released in two stages. An early release (EDR3) is on track to be released in late 2020 with the full DR3 catalogue expected in the latter part of 2021. Of interest here, DR3 will contain ∼30 million radial velocity (V_{LSR}) values (https://starry-project.eu/wp-content/uploads/sites/17/2019/07/mora_gaia.pdf) which would have greatly enhanced our study had they been available in DR2. Additional data releases are planned and are dependent upon approvals being given for mission extensions.

2.3 Data Release 2 (DR2)

Gaia DR2 occurred in April 2018 with a five-parameter astrometric solution for more than 1.33×10^9 sources (Brown et al., 2018).

DR2 is based on the first 22 months of the nominal 60-month mission lifetime and contains high-precision parallax and proper motion data for over 1 billion sources. This data release also contains precise multi-band all-sky photometry and radial velocity information, as described previously. Data collection for DR2 started at an on-board mission time (OBMT) 1078.3795 rev = J2014.5624599 TCB and ended at OBMT 3750.5602 rev = J2016.3914678 TCB (approximately from 10:30:00 UTC 25 July 2014 to 11:35:00 UTC 23 May 2016).

This data release provides the positions, parallaxes, and proper motions of 1.3 billion sources. For bright sources (G<14) the median parallax uncertainty is 0.03 mas and 0.07 mas yr^{-1} for the proper motions, the parallax zero-point uncertainty is about 0.03 mas. More details regarding the *Gaia* DR2 astrometric parameters can be found in Arenou et al. (2018) and Lindegren et al. (2018). The data descriptors collected and made available in the Gaia Archive are given in Table A.1, Appendix A.

2.3.1 Data Access

Data products from the *Gaia* mission are freely available through the online ESA *Gaia* Archive portal[2]. There are a number of other associate data centres which offer access to *Gaia* data which are coordinated through the auspices of DPAC by CU9. These are at: (1) the Centre de Données astronomiques de Strasbourg (CDS)[3], (2) The ASI Space Science Data Center (SSDC)[4], (3) the Astronomisches Rechen-Institut (ARI)[5], and (4) the Institut für Astrophysik Potsdam (AIP)[6]. Each of these partner data centres presents *Gaia*

[2] http://gea.esac.esa.int/archive/
[3] http://cdsweb.u-strasbg.fr/gaia
[4] http://gaiaportal.asdc.asi.it/
[5] http://gaia.ari.uni-heidelberg.de/
[6] https://gaia.aip.de/

data distributed from the central ESA *Gaia* Archive and it is from this portal that we have accessed DR2 data for this study.

The Gaia Archive home page provides access to the functionality of the archive through a number of search interfaces. The Archive interfaces and protocols are described in Salgado et al. (2017). Interaction with the data catalogue is achieved through using the ADQL structured query language described by Osuna et al. (2008). No specific software is required to access the archive, the only prerequisite being access to a web browser.

3 COMPARATIVE *SPITZER* INFRARED STUDY

Gaia data is accessed by submitting a query, written in the Astronomical Data Query Language (ADQL), via a Graphical User Interface (GUI) on the ESA *Gaia* webpage[1]. The ADQL is based on the Structured Query Language (SQL) which was developed in the late 1970's (Chamberlin, 2012) for managing data held in relational databases. ADQL is a specialised form of SQL developed for use with astronomical datasets. In ADQL, queries are written to the database and contain expressions indicating where the required data may be found (Ortiz et al., 2008). These expressions identify the data source (the **SELECT** statement), the table or tables that store the required data (the **FROM** statement) and the parameters required to limit the data you obtain (the **WHERE** statements).

An ADQL query was constructed to identify sources towards the Taurus region using a $10^{\circ}\times15^{\circ}$ 'box' centred on RA (J2000.0)=68.5° and Dec (J2000.0)=+27.0°. This effectively defined an area on the sky of roughly 126 pc^2 at the approximate distance of the Taurus cloud. Parallax values were set between 5.0 and 10.0 mas defining a box covering a distance range from 100 to 200 pc designed to 'bracket' the expected distribution of sources around 140 pc. The query was uploaded to the *Gaia* Archive, Advanced (ADQL) search engine and, once compiled, the output file was downloaded in comma-separated (.csv) format (Shafranovich, 2005) suitable for analysis.

This initial query, detailed in Appendix B, Listing B.1 returned 4770 sources. These results were manually cross-referenced to the SIMBAD database and other literature sources to maximise the information known on each object, and to obtain relevant data from previous observations and studies. This cross-referencing exercise identified that some of the literature sources were not present in our DR2 query results. The original query was reviewed and it was decided to remove most of its quality statements and to re-run the code through the Archive. In reviewing the query, quality statements providing a lower limit to the signal-to-noise ratios in the red (R_P) and blue (B_P) bands were removed as were filters excluding stellar binary systems and measurements where crowding had seriously affected the photometry. It was recognised that the omission of these filters, whilst increasing the number of sources returned, would also provide some sources of 'poor' astrometric quality. To counteract this to some extent, the new query was set to only include sources with at least 5 independent astrometric measurements ($astrometric\_n\_good\_obs\_al > 5$) thereby ensuring a reliable selection of sources. To maximise the number of sources returned, no other quality flags were defined.

[1] https://gea.esac.esa.int/archive/

This subsequent query (Appendix B, Listing B.2) produced 7587 sources and the cross-referencing exercise with SIMBAD and the literature was repeated. When completed, additional data such as stellar type, archival radial velocities and UWV positional information from the on-line UWV Calculator[2] were added to the spreadsheet for subsequent use.

Due to the size of the final spreadsheet and the requirement to format data output consistently, it was decided to do all analysis and reporting using the `Python` (Van Rossum et al., 2007) general-purpose programming language. After performing distance calculations on the mean parallax values of our 7587 sources using the expression

$$d = \frac{1}{p} \tag{3.1}$$

where d denotes the distance and p is the *Gaia* parallax ($parallax$), see Appendix F.2.2, the results were plotted on a histogram in 1 pc bins. The subsequent distribution (Figure 3.1) showed no evidence of the expected peak in population at around 140 pc.

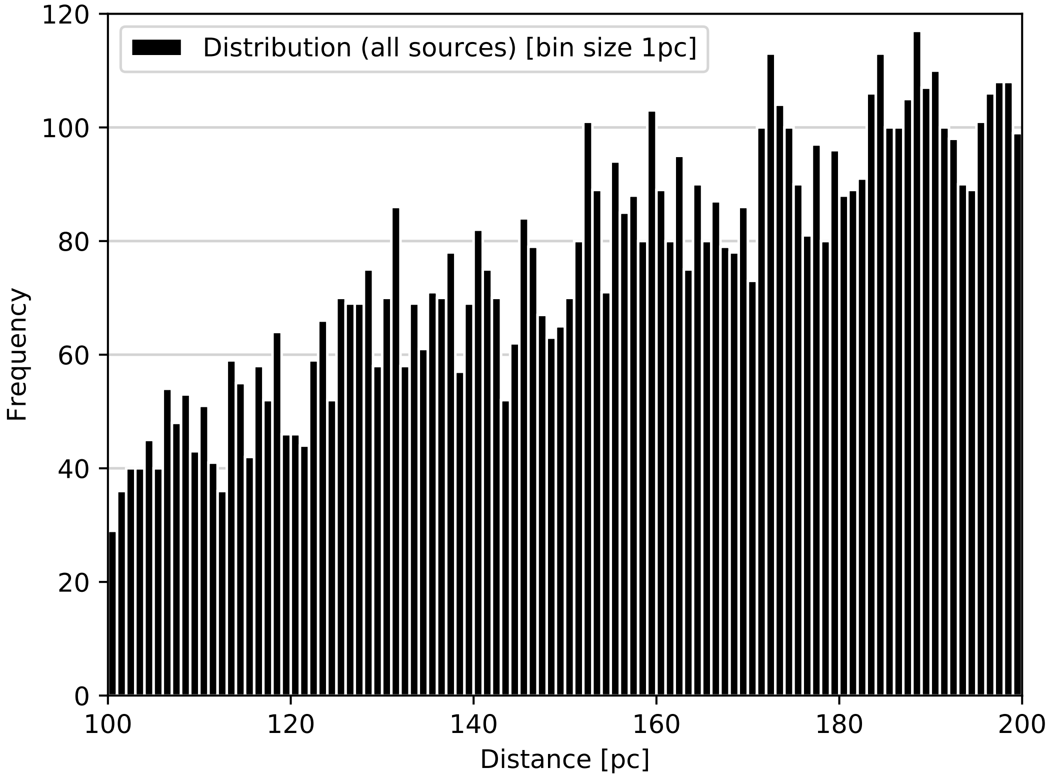

Figure 3.1 Distribution of 7587 *Gaia* DR2 sources identified in the *Gaia* Archive query.

The rising slope of detected sources in Figure 3.1 was recognised as being a two-dimensional representation of an increase in spatial volume, caused by the expansion in the bounded area of our query 'box' over the distance from

[2]http://dr-rodriguez.github.io/UWVCalc.html

100 pc to 200 pc. Assuming an almost near-constant density of the interstellar medium on such a small scale, it is expected that the number of stars should increase as R^2 mirroring the increase in cross-sectional area of each equal-width distance bin. The distribution seen in Figure 3.1 suggests that the Taurus sources are being totally swamped by foreground and background objects. To visualise the spatial distribution of these sources the visual extinction map from the Two Micron All-Sky Survey (2MASS) infrared survey presented in Schneider et al. (2011) is used as a background and our query results have been over-plotted (Figure 3.2) to identify their location within our study area.

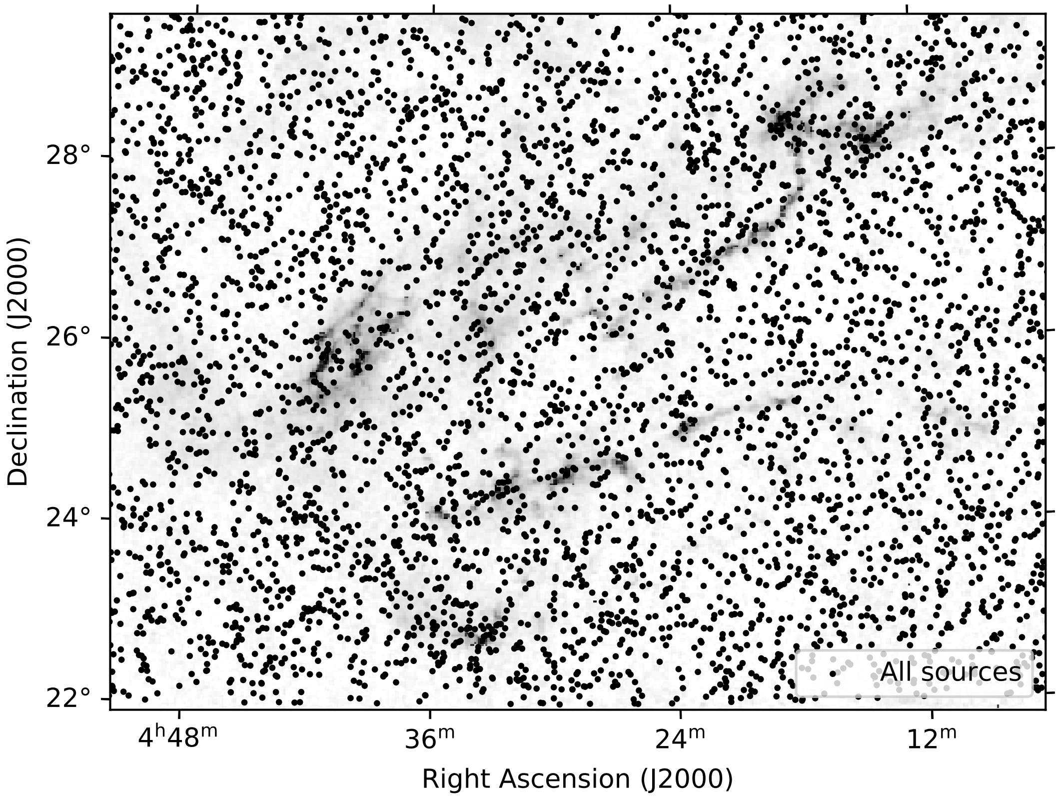

Figure 3.2 Sources have been overlaid on a visual extinction map calculated from the 2MASS survey (Schneider et al., 2011).

The distribution seen in Figure 3.2 confirms the likely contamination of our study by coincident field stars, although obvious features in the cloud are apparent through the over-density of stars in certain regions.

3.1 Identifying the study group

To remove possible contamination of our sample by foreground and background field stars they were cross-referenced with the *Spitzer* SSTtau catalogue (Rebull et al., 2010) of known infrared identified YSO's. 168 objects in our search area with known *Gaia* parallaxes and proper motions were identified. Within this subset the largest parallax error is ±1.214 mas for object Gaia DR2 151265002954775936 (KPNO-Tau 4), which is a classified L0 brown dwarf in the SIMBAD database (Canty et al., 2013).

Figure 3.3 shows the parallax errors in relation to *Gaia* DR2 G-band magnitude (*phot_g_mean_mag*) for the 168 sources identified in the *Spitzer* catalogue. It can be seen that brown dwarfs within the sample typically have larger parallax errors, suggesting constraints on the detection of such low luminosity objects. Parallax errors on the remaining sources are significantly lower, with a typical median value of ±2-3 pc.

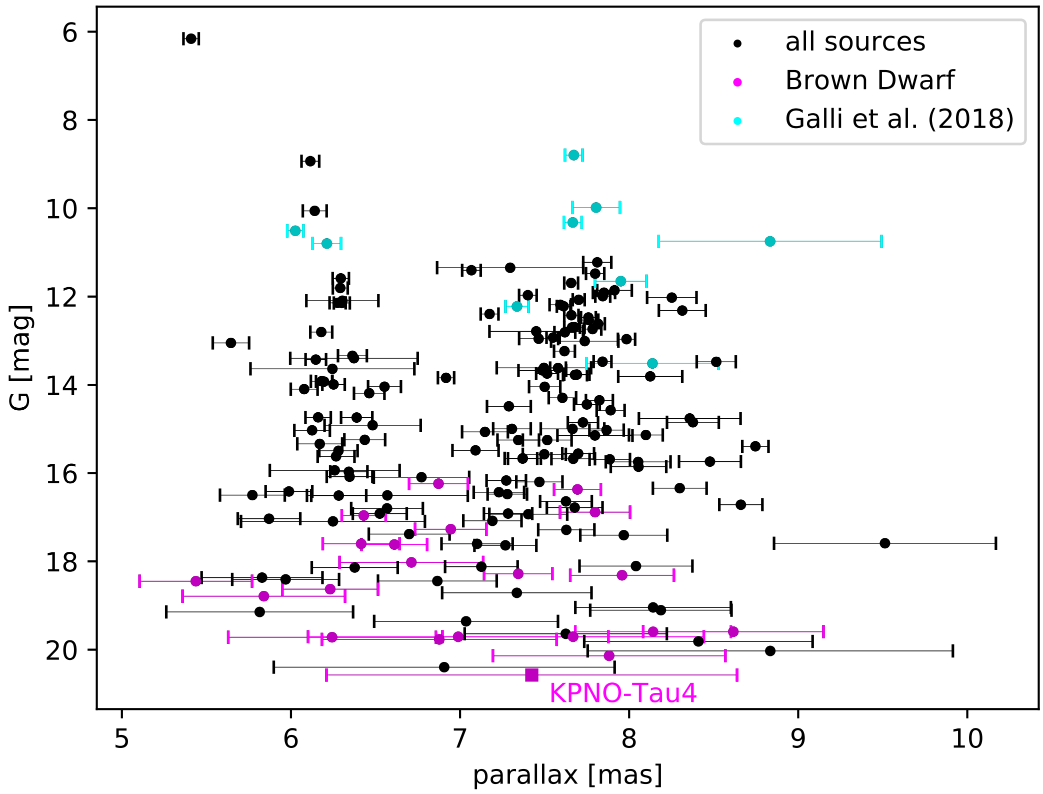

Figure 3.3 Parallax errors of the 168 *Gaia* DR2 sources identified in the *Spitzer* SSTtau catalogue of Taurus members, plotted against G-Band mean magnitude. Sources identified in the SIMBAD Astronomical Database as brown dwarfs are shown in magenta whilst those cross-matched to Galli et al. (2018) are in cyan (see Section 3.2).

From Figure 3.3 it can clearly be seen that there is a double peaked scattering in the parallax (and hence, distance) distribution of the sources. It should be noted that the parallax error bars shown in Figure 3.3 are symmetric about the sources, reflecting the values obtained in the data query, and are given to 1σ as defined in Appendix A, Table A.1. This symmetry in parallax errors, due to the inverse relationship between parallax and distance shown in Equation (3.1), do not transfer to the derived values of distance errors, where asymmetric errors result. This can be seen in the following example:

Suppose we measure the parallax to one of our query stars which has a value of 0.009±0.0006 arcsec (note the symmetric errors). Using Equation (3.1) *provides a mean distance of 111 pc but with asymmetric errors of* $^{+8}_{-7}$ *pc.*

The properties of the 168 *Gaia* sources discussed above are listed in Appendix C in Table C.1. Taking the distances of the 168 sources and binning the values at 3 pc intervals produces the distance distribution seen in Figure 3.4. The same double-peaked distribution seen in Figure 3.3 is visible. A double-Gaussian curve (shown in black) is fitted indicating a minimum in the bi-modal distribution at 147.9 pc (hereafter taken to be 150 pc) with the 'near' group (red) centred at 130±6 pc and the 'far' (blue) group centred at 160±4 pc at 1σ.

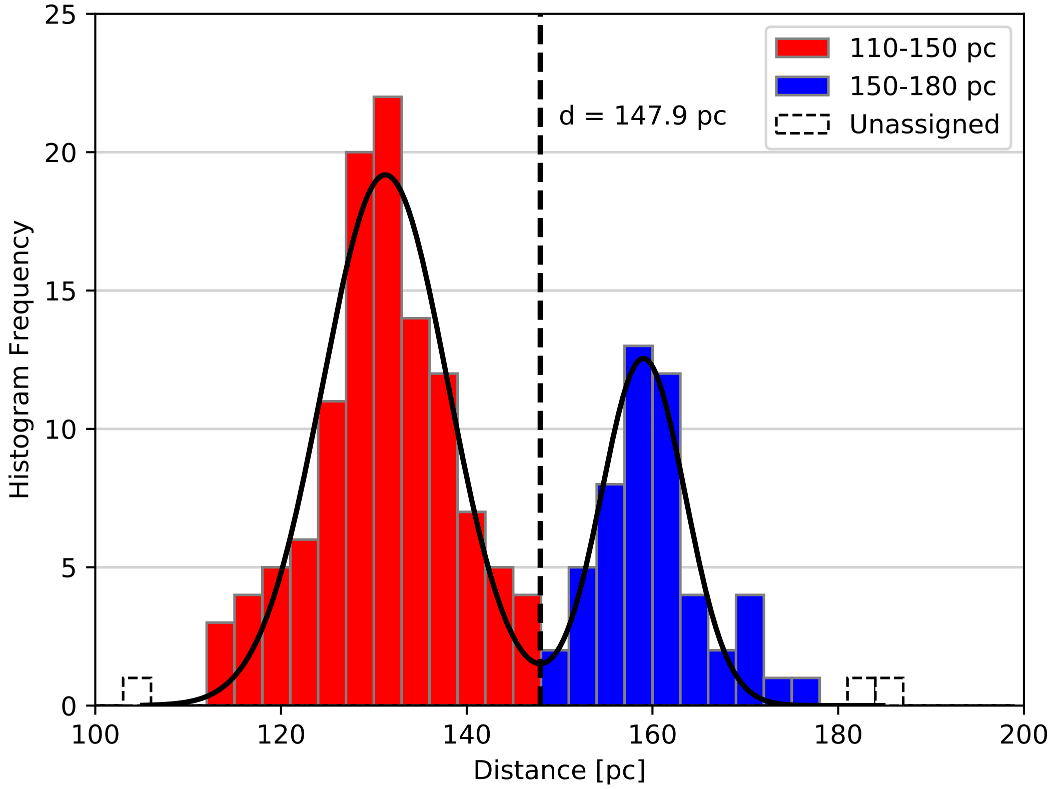

Figure 3.4 Distance distribution of 168 *Gaia* DR2 sources identified in the *Spitzer* SSTtau catalogue of Taurus members. Sources are grouped in 3-pc bins. Two distinct groupings are seen. A double-Gaussian curve is fitted identifying a minimum value at 147.9 pc (see text for details).

Whilst the double-Gaussian fit in Figure 3.4 clearly shows a bi-modal distribution this is not a conclusive statistical test of multi-modality. To determine the exact nature of the observed distribution a number of statistical tests have been applied to the data at various stages in our investigation.

3.2 Validation of *Gaia* DR2 distance data

Comparing the *Gaia* DR2 distance data with previous VLBA determinations (Torres et al., 2009; Galli et al., 2018) to draw comparisons between the two observational techniques finds nine sources common to both studies.

Table 3.1 presents the comparative distances of these sources along with their spectral type and classification from Rebull et al. (2010: Table 6). These sources are shown in cyan in Figure 3.3 which shows their *Gaia* G-Band mean magnitudes and associated errors. It can be seen that these sources are amongst the brightest and that they are distributed between the two groups identified.

Gaia DR2 Name	Common Name	Type/Class[a]	*Gaia* DR2 Dist. (pc)	VLBA[b] Dist. (pc)
147778490237623808	V807 Tau B	K7 II	113.2±8.5	$126.6^{+1.7}_{-1.7}$
148116246465275520	V999 Tau	K7 III	122.9±5.9	$143.4^{+4.2}_{-3.9}$
164513538249595136	V1023 Tau	K7 III	125.8±2.4	$130.1^{+0.5}_{-0.5}$
163184366130809984	V773 Tau A	K3 II	128.1±2.3	$130.0^{+1.5}_{-1.4}$
164536250037820160	HDE 283572	G5 III	130.3±0.9	$129.5^{+1.0}_{-0.9}$
164518589131083136	HD 2830518	K3 III	130.4±0.9	$129.0^{+0.5}_{-0.4}$
163233981593016064	V1096 Tau	M0 III	136.3±1.3	$124.4^{+8.2}_{-7.2}$
152104381299305600	HD 283641	K1 III	161.0±2.2	$159.1^{+1.8}_{-1.8}$
145213192171159552	HP Tau G2	G0 III	166.0±1.3	$162.7^{+0.8}_{-0.8}$

[a] Rebull et al. (2010: Table 6).
[b] Galli et al. (2018: Table 8).

Table 3.1 Comparison of *Gaia* DR2 and VLBA distances.

There is good agreement between the two data sets except for three sources, namely Gaia DR2 147778490237623808 (V807 Tau B), Gaia DR2 148116246465275520 (V999 Tau) and Gaia DR2 163233981593016064 (V1096 Tau). SIMBAD identifies V807 Tau B as a K7 Variable Star of Orion Type (Nguyen et al., 2012), V999 Tau as an M0.6 Variable Star of Orion Type (Herczeg and Hillenbrand, 2014) and V1096 Tau as an M0 T Tauri star (Rivière-Marichalar et al., 2012). The sources presented in Table 3.1 have *Gaia* G-Band mean magnitude values (*phot_g_mean_mag*) ranging between 8.79 to 13.51 mag. Within this range, the three sources under discussion have magnitudes of 10.75, 13.51 and 12.22 mag respectively and are within the five faintest sources presented in the table. V1096 Tau has a *Gaia* DR2 G-band extinction value (*a_g_val*) of 2.97 mag but values for the other two objects are not available. Although these three sources are intrinsically fainter than the remaining six it is not possible to make a definitive judgement concerning the large errors displayed by these sources.

Figure 3.5 shows the linear relationship between the two independently measured distance values, and their errors, of the sources presented in Table 3.1. The linear relationship between two such independent variables, that have a normal distribution, also have a normal distribution. As such, it is expected that approximately 33% (i.e. three) of our sources should lie beyond the 1σ linear relationship, as is seen in the figure. Other than for the three

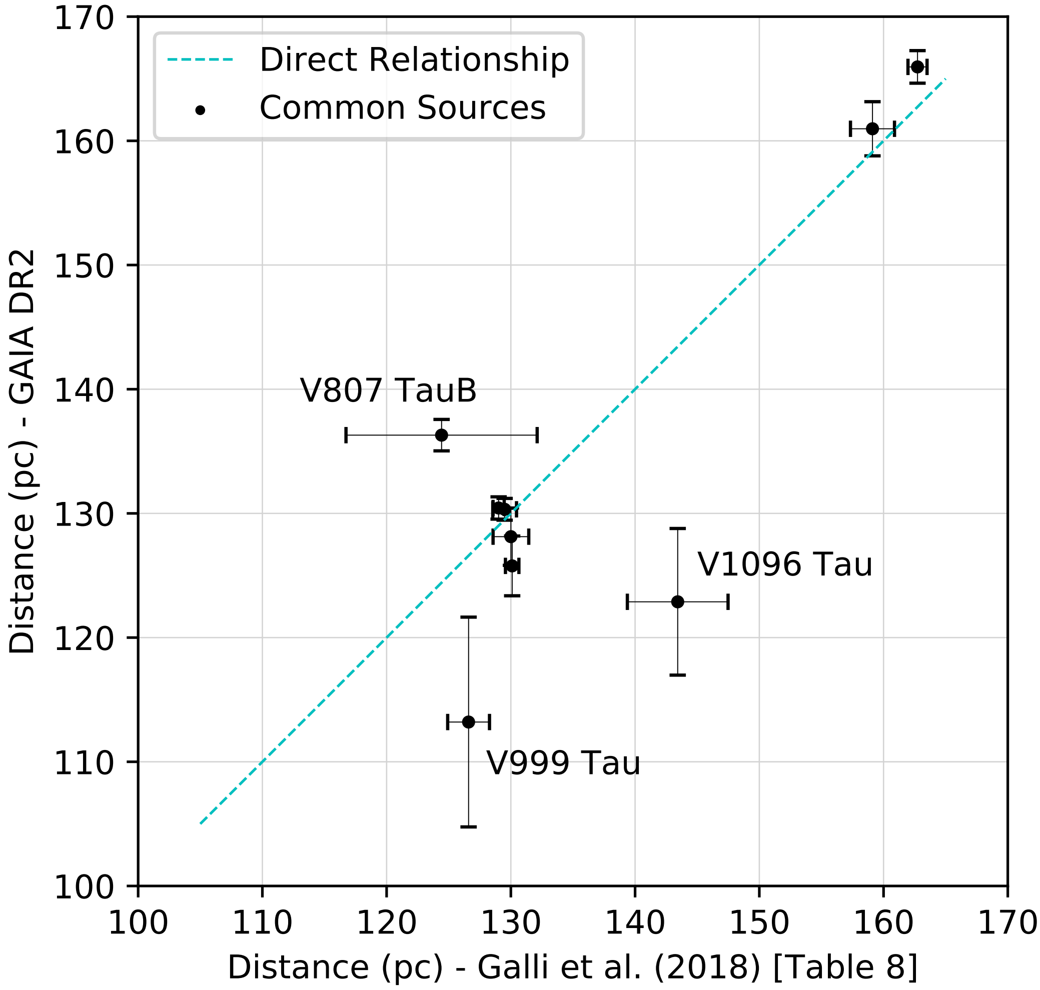

Figure 3.5 Comparison of *Gaia* DR2 and VLBI distance data.

sources with large errors mentioned above, the *Gaia* DR2 measurements are consistent with previous VLBA measurements.

3.2.1 Statistical analysis of distance distribution

Hartigans' Dip Test (Hartigan, Hartigan, et al., 1985) is recognised as being a robust statistical measure of the modality of a continuous distribution where the 'dip' measures the departure of a distribution from uni-modality. The Hartigan Dip Statistic (HDS), corresponding to the probability 'p-value', is determined by repeatedly sampling the maximum difference between the observed distribution of data and that of a uniform distribution that is chosen to minimize this maximum difference. P-values $<$0.05 are an indication of significant bi-modality and values greater than 0.05 but less than 0.10 suggest bi-modality with marginal significance.

To analyse the distribution of our sources we have used a `Python` implementation of Hartigans' dip test for uni-modality using the `NumPy` mathematical library and the `UniDip` clustering algorithm (Maurus and Plant, 2016) and obtained a p-value of 0.025. Figure 3.6 graphically represents the results of our analysis, the red and blue shaded regions show the modes identified in the analysis (Maurus and Plant, 2016), superimposed on the histogram plot of our groups. It can be seen that, statistically, two separate distributions are identified although neither region corresponds exactly with the normal distribution. This variation is due to the number size, extent and ’tightness’ of the stellar groupings.

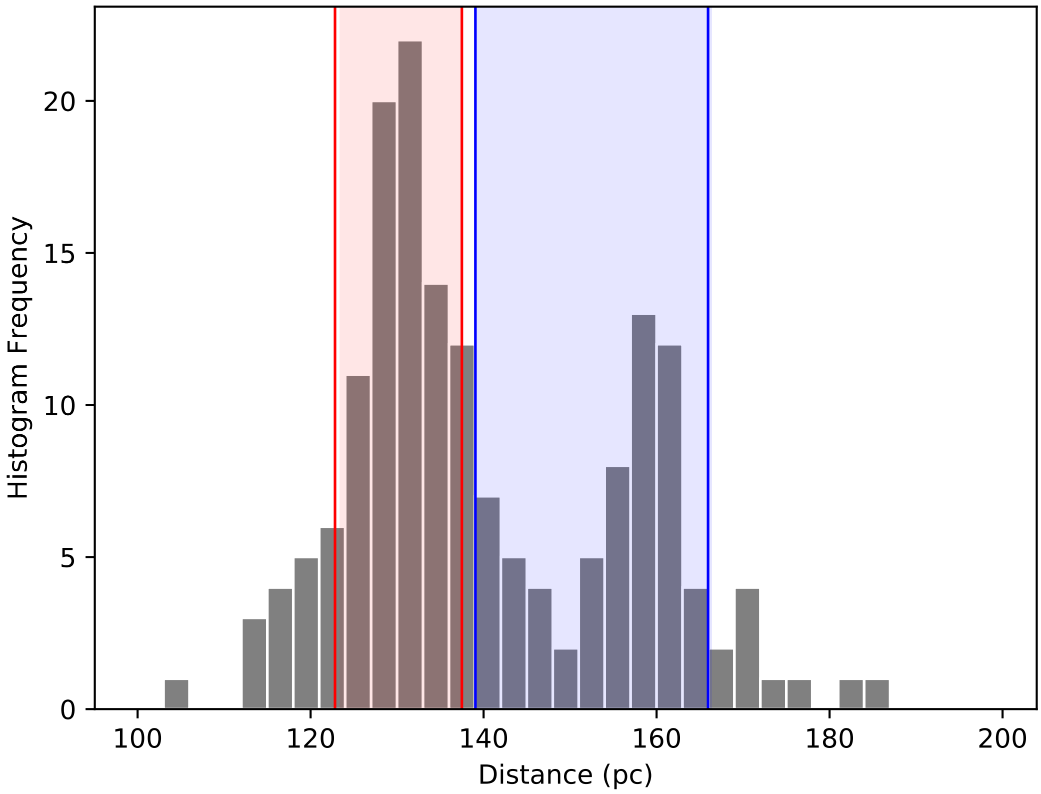

Figure 3.6 Results of Hartigans’ analysis of distance groupings. The multi-modal nature of this distribution is confirmed with a p-value of 0.025. The red and blue shaded regions show the modes identified in the analysis (see text for details).

The derived p-value of 0.025 suggests that we reject the null hypothesis of uni-modality and identify our distribution as bi-modal with a boundary between the two groups at ∼150 pc, as previously identified in Section 3.1.

Having statistically identified that our distance distribution represents two independent populations we split them into ‘near’ and ‘far’ groups and identify these as lying between 110 to 150 pc and 150 to 180 pc respectively. Figure 3.4 identifies our two groups, colour coded red and blue for the ‘near’ and ‘far’ groups respectively. The three sources coded white located outside the two main populations are taken to be un-associated with the two groups and are not discussed hereafter. We have called our ‘near’ and ‘far’ groups the **‘Two Horns’** of Taurus and they are the subject of our pre-print publication (Fleming, Kirk, and Ward-Thompson, 2019).

3.3 Proper Motion study

From the proper motion values presented in Appendix C, Table C.1 it is possible to study the distribution of proper motions for our sample of 168 sources. Figure 3.7 shows histograms of the relative distributions of proper motion within our sample, binned at 5 mas yr^{-1}. The distribution of the vector components pmRA, the proper motion value in right ascension, and pmDec, the motion value in declination are clearly seen as is the magnitude of the proper motion vector (μ).

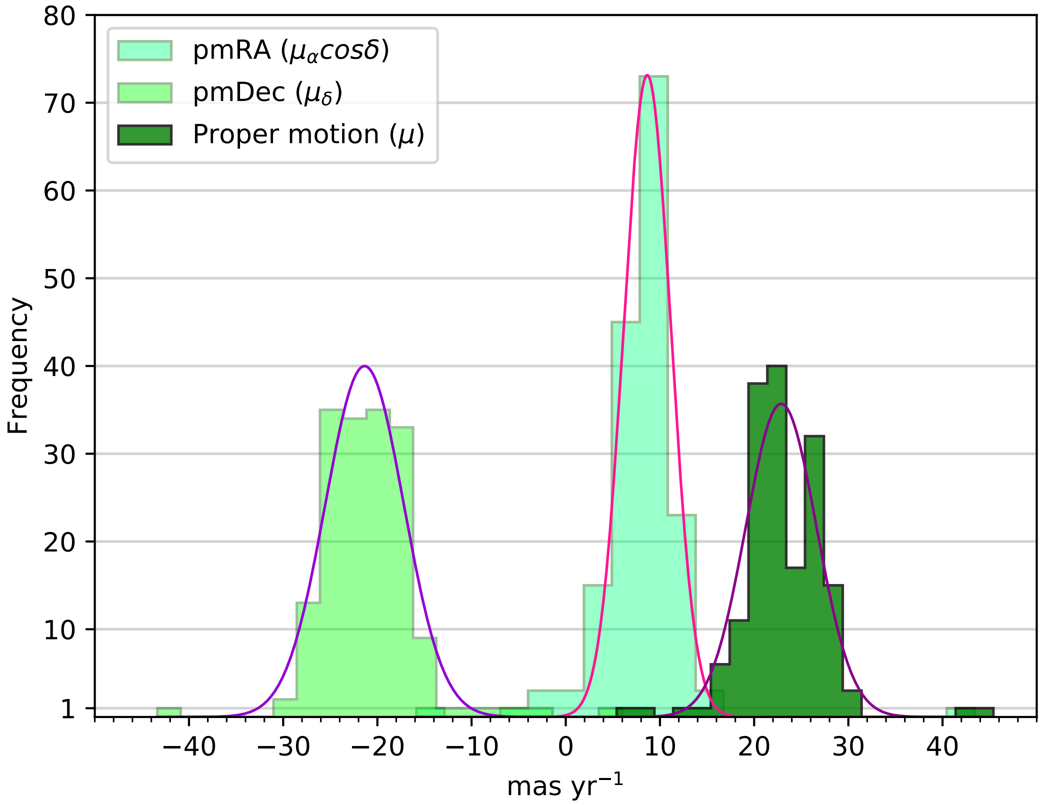

Figure 3.7 Proper motion distributions of the 168 cross-referenced *Spitzer* sources.

It can be seen that all three peaks follow a normal distribution, with outliers in each case. The distribution of pmRA is found to be centred on 8.03 mas yr^{-1}, pmDec on -21.06 mas yr^{-1} and the proper motion (μ) at 23.09 mas yr^{-1} with standard deviations of 4.52, 5.02 and 4.50 respectively. Analysing these distributions further shows that they are almost symmetrical with pmRA and pmDec having skewness values of 1.57 and 0.96 respectively. Skewness is a measure of the asymmetry of the data contained within a histogram. Histograms that are symmetrical have a normal distribution with a skewness value of zero. Distributions have a positive skew if their mean value is greater than its median, whilst a negative skew indicates that a distributions median is larger than its mean. Equation (F.6) defines the relationship between proper motions in right ascension and declination and an objects overall proper motion, shown here in dark green. This proper motion distribution has a skew of 0.65 and, disregarding the outliers, minimum and maximum values of ∼11 and 30 mas yr^{-1} respectively.

A number of proper motion studies have previously been undertaken of this region, notably those conducted by Jones and Herbig (1979); Walter et al. (1987); Hartmann et al. (1991); Gomez et al. (1992); Frink et al. (1997); Ducourant et al. (2005); Bertout and Genova (2006) and more recently Dzib et al. (2015) and Galli et al. (2018). In general, these are all studies of pre-main sequence stars, seeking to identify the proper motions of members of the Taurus moving group. Table 3.2 lists the values from these studies. We have used these to constrain the upper and lower limits of proper motion for this study.

Reference	μ_{min} (mas yr^{-1})	μ_{mean} (mas yr^{-1})	μ_{max} (mas yr^{-1})
Jones and Herbig (1979)	...	22.80	...
Frink et al. (1997)	...	21.24[a]	...
Bertout and Genova (2006)	9.37	22.38	41.22
Slesnick et al. (2006)[b]	13.89	...	43.05
Torres et al. (2009)[c]	...	∼20.0	...
Galli et al. (2018)[d]	15.00	∼22.0	39.00
Mean literature values[e]	12.75	22.14	41.09
This study	11.94	23.09	30.60

[a] Value given for the central part of the Taurus-Auriga cloud system.
[b] Values derived from their figure 9 (lower histogram).
[c] cited in Dzib et al. (2015).
[d] Maximum and minimum values obtained from their figure 2.
[e] Ignoring imprecise values from Torres et al. (2009) and Galli et al. (2018).

Table 3.2 Taurus proper motion values in the literature.

All 168 identified sources (see Table C.1, Appendix C) have *Gaia* DR2 proper motion values, and of these, 165 lie within the 'near' and 'far' populations mentioned above – the remaining 3 are shown in white in Figure 3.4. Based on the values given in Table 3.2, for the purposes of this study, upper and lower limits of proper motion for the Taurus moving group are taken as being 40 mas yr^{-1} and 12 mas yr^{-1} respectively. Within these limits there are 161 sources. These limits also correspond with those seen previously in Figure 3.7. Figure 3.8 provides a schematic breakdown of how these final 161 sources have been determined.

The proper motions of our two groups are shown in Figure 3.9 which shows the distribution of all 161 members in both 'near' and 'far' populations (the colour coding of the two groups is the same as in Figure 3.4). It can be seen that there are two distinct populations with outliers in each group.

To determine if the distribution of proper motions seen in Figure 3.9 is statistically significant (i.e. that it is not due to random chance), a K-Means

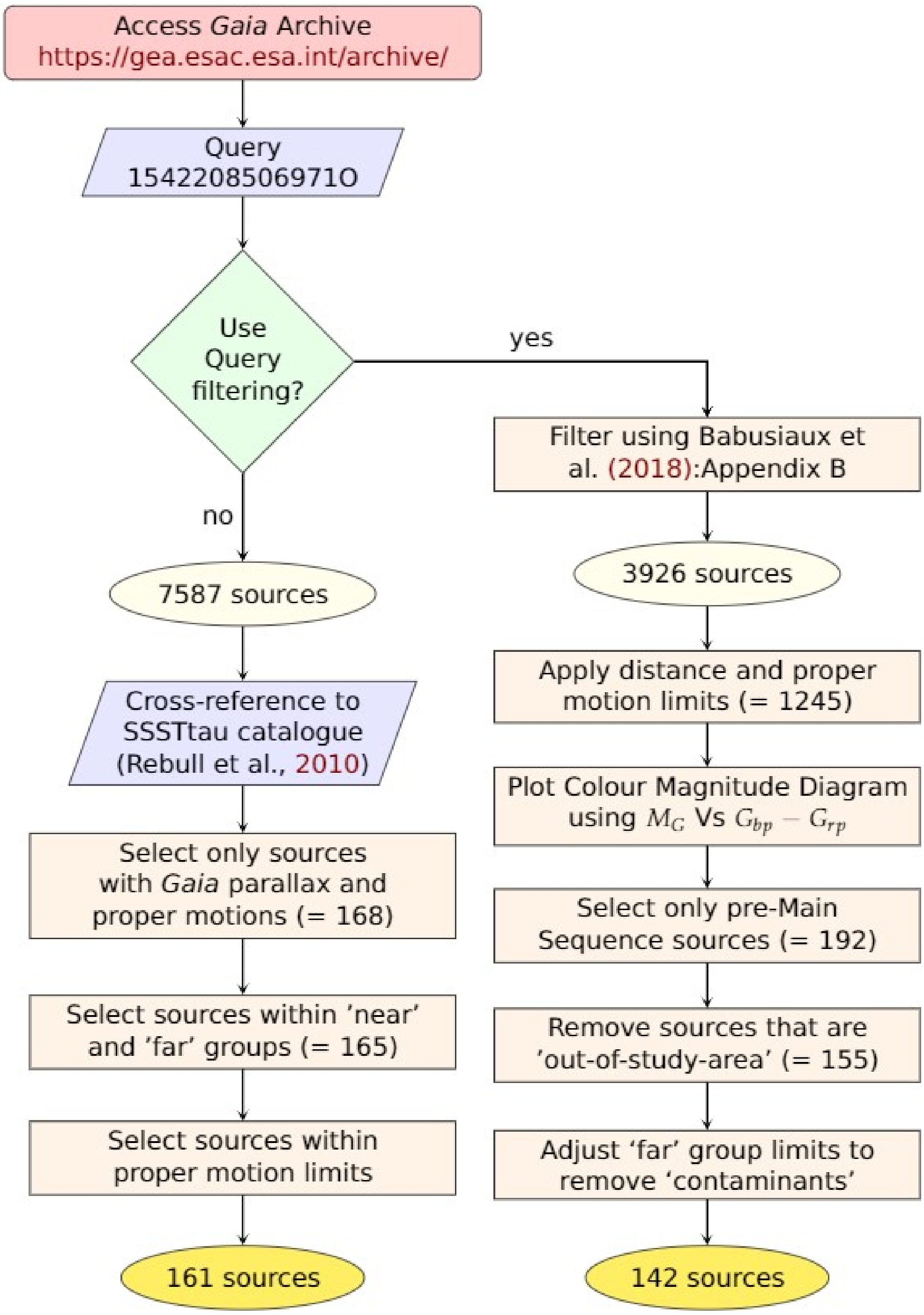

Figure 3.8 Graphical representation showing the determination of the sources from our *Gaia* Archive Query. The left column describes the process used in Chapter 3 whilst the right column defines the sources used in Chapter 4.

clustering algorithm was used to investigate the sources. This study can also be used to determine the centroids of the individual groups should the groups be found to have different proper motions. Each of the two groups identified in the distance distribution are found to have different mean proper motions. There are 111 members in the 'near' group and 50 in the 'far' group – the remaining 4 sources are rejected as lying outside of the 12–40 mas yr^{-1}

proper motion cut. The mean proper motion of the 'near' population is 24.5±2.8 mas yr^{-1}, and that of the 'far' population is 20.1±2.4 mas yr^{-1} as seen in Figure 3.10.

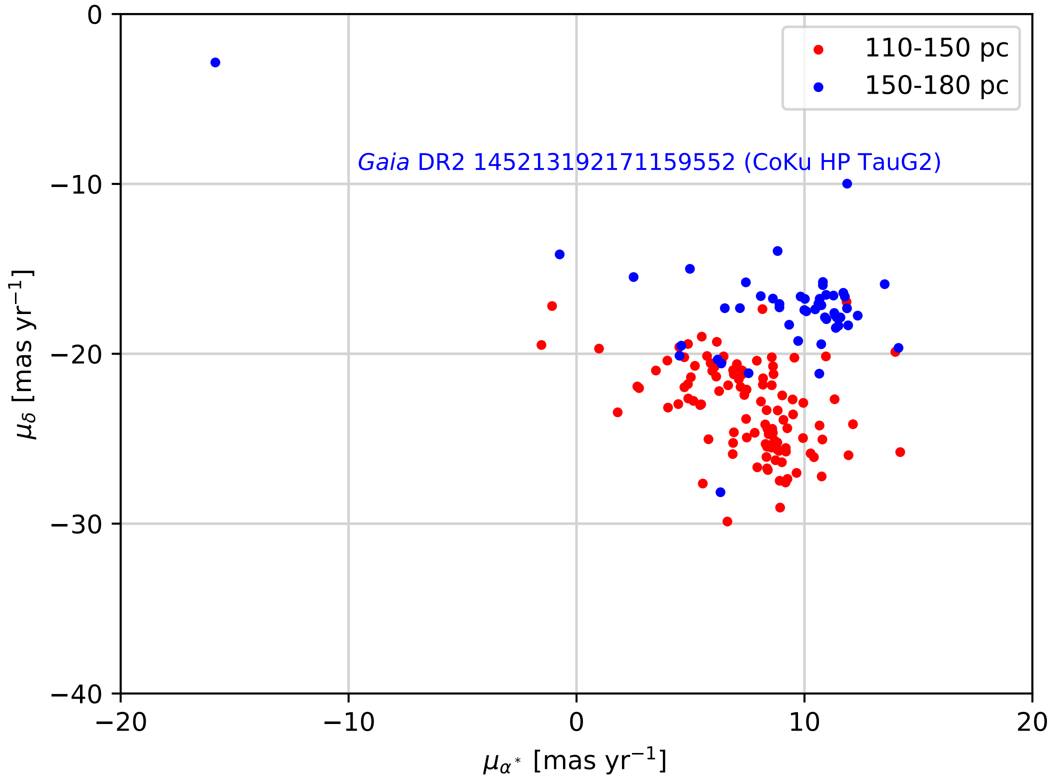

Figure 3.9 Proper motions of all 161 members of our 'near' and 'far' groups.

Figure 3.10 has been zoomed-in to show the bulk of the sources more clearly – there are five sources in Figure 3.9 which are within our proper motion limits of 12–40 mas yr^{-1} but which are outside of the plotted boundaries of Figure 3.10. Of these five, two lie in the 'near' population (Gaia DR2 146675954953119104 and Gaia DR2 147546080967742720), and three lie in the 'far' population (Gaia DR2 148116276529733120, Gaia DR2 147248216395196672 and Gaia DR2 145213192171159552). One of these sources, Gaia DR2 145213192171159552 (CoKu HP Tau G2) has been previously studied (Torres et al., 2009) using the VBLA, which determined a parallax of 6.2±0.3 mas. *Gaia* DR2 determines a value of 6.02±0.04 mas which is fully consistent.

For comparison against previous studies, 7 sources from the study of Galli et al. (2018) lie within our 'near' population and 2 lie in the 'far' group (Table 3.1). These numbers are statistically low, nevertheless they provide mean proper motions of 24.90±4.88 and 19.66±0.50 mas yr^{-1} for the 'near' and 'far' populations respectively, which are fully in agreement with the values found here.

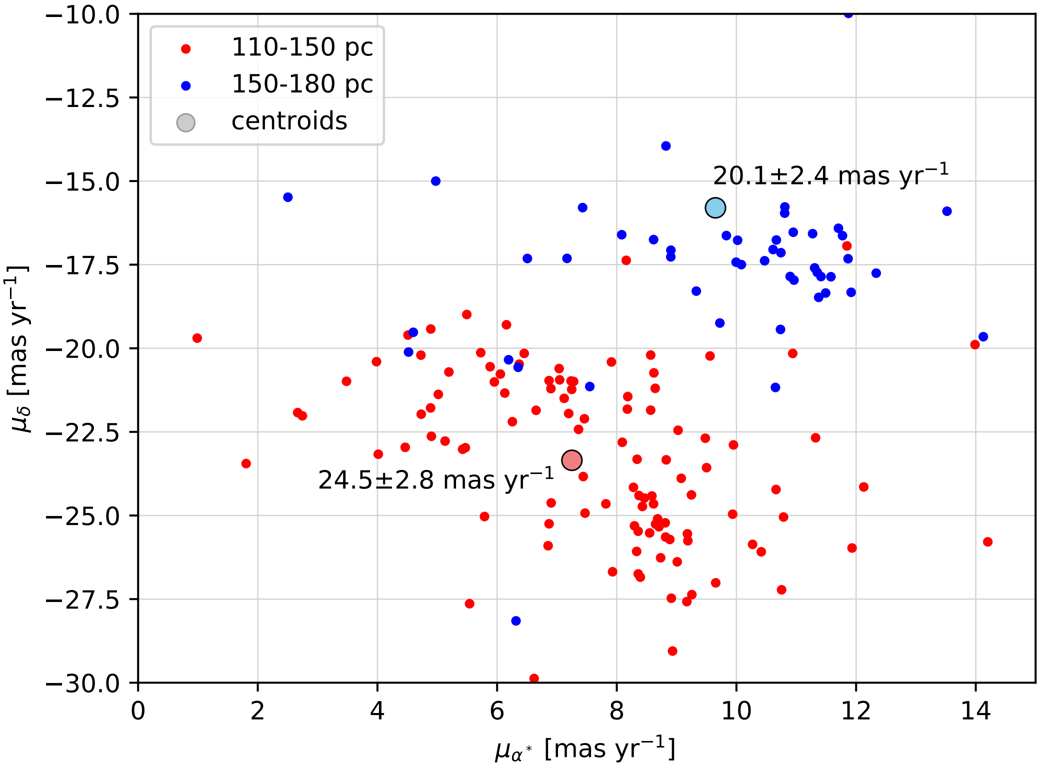

Figure 3.10 Proper motions of 156 of the stars shown in Figure 3.9 with proper motion limits of 12 mas yr^{-1} to 40 mas yr^{-1}. There are five outlying sources beyond the area shown on this plot (see text for details).

3.4 Discussion

This study has identified two significant peaks (see Figure 3.4) in the distance distribution of our query sample when compared to *Spitzer* data. These peaks are centred at approximately 130 and 160 pc. Separating these peaks into 'near' and 'far' populations, as indicated by the red and blue colouring in Figure 3.4, results in mean (and error on the mean) distances for each component of 130.6±0.7 and 160.2±0.9 pc respectively. For these groups, the standard deviation on the distance is ∼6 & ∼4 pc respectively versus a mean error on each measurement of ∼4-5 pc. It is probable that the standard deviations for the distances are broadened by these measurement errors. Table 3.3 shows the parameters of each group. These distributions are roughly consistent with the findings of previous studies mentioned in §1, but far more double-peaked than was previously realised.

For the purposes of simplicity, the groups are identified as lying between 110–150 pc and 150–180 pc respectively. From Figure 3.10 it can be seen that these two populations have markedly different proper motion characteristics. The populations fall within two separate and distinct proper motion groups, related to their distance. The mean proper motions of the two groups are listed in Table 3.3 and are 24.5±2.8 and 20.1±2.4 mas yr^{-1} for the 'near' and 'far' populations respectively. The mean angles, θ, of the proper motions of the two populations are also listed in Table 3.3, along with their standard deviations. These are 162±6° and 154±17° for the 'near' and 'far' populations respectively, where all angles are measured east of north.

	Near	Far
Number of Sources	111	50
Mean Distance [pc]	130.6±0.7	160.2±0.9
Standard Deviation [1σ]	6.7	4.5
$\mu_\alpha \cos\delta$ [mas yr^{-1}]	7.5	8.9
μ_δ [mas yr^{-1}]	-23.1	-17.3
μ_{Total} [mas yr^{-1}]	24.5	20.1
Standard Deviation [1σ]	2.8	2.4
Angle θ [degrees] (East of North)	162	154
Standard Deviation [1σ]	6	17

Table 3.3 Properties of the near (red) and far (blue) populations. Statistics are calculated after distance and proper motion cuts have been made.

To statistically check whether the two groups come from the same distribution a general-purpose non-parametric two-sample Kolmogorov-Smirnov (KS) test (Kolmogorov, 1933) is performed. The proper motion distribution is examined using an implementation of the Python `SciPy` routine. Figure 3.11 plots histograms of the pmRA and pmDec data sets (shown in Figure 3.10) that have been applied to the KS Test. The resultant p-value of 4.06 x 10^{-17} is also displayed.

This two-sample test is used to check whether the two groups come from the same distribution since it is sensitive to differences in both location and shape of the two samples. Peacock (1983) recognise this test as being a powerful tool in the analysis of astronomical data. However, it is acknowledged that caution is needed when using this test in astronomical applications (e.g. Feigelson and Babu, 2013; Stephens, 1974) since KS probabilities can be misleading if the model used is derived from the dataset itself. Figure 3.11 shows the results of this test where a p-value significantly $<$0.001 is derived, supporting our earlier identification of a non-unimodal distribution (see §3.2.1), and rejects the possibility that the two groups come from the same population.

3.4.1 Group and structure correlations

Having statistically determined that two groups exist in both the distance and proper motion distributions it is possible to use the data presented in Figures 3.4 and 3.9 to obtain a clearer picture of the distribution of objects within our sample region.

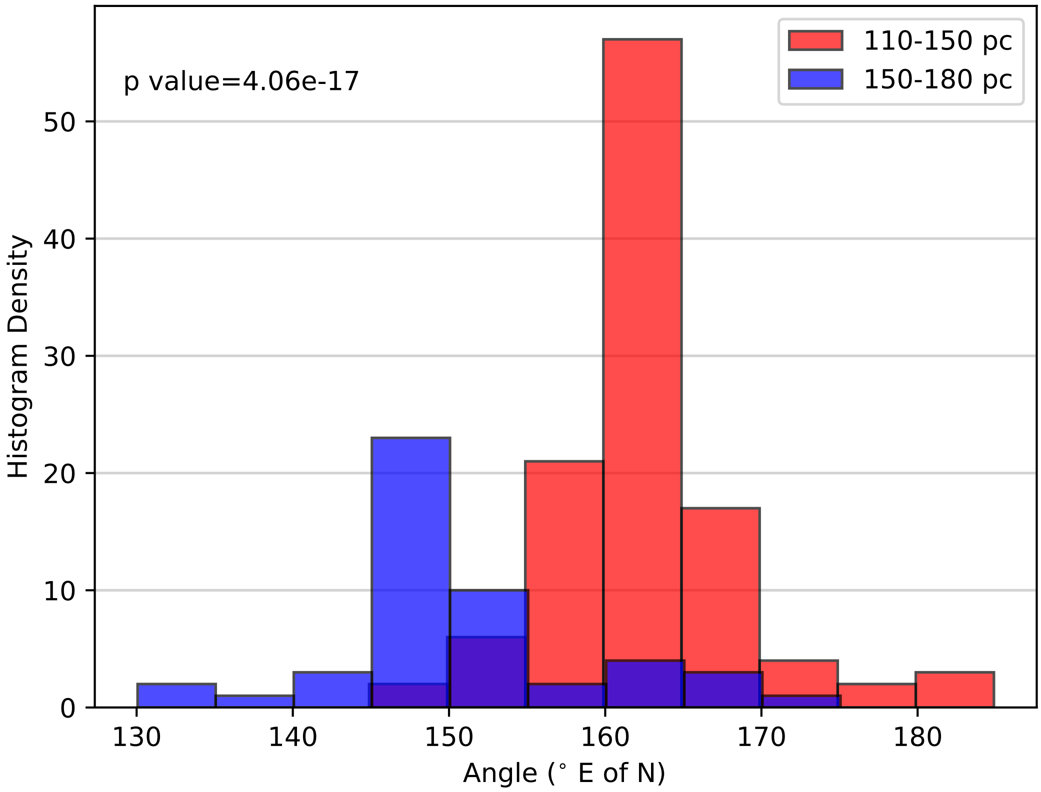

Figure 3.11 Result of two-sample KS test showing histograms of the underlying data sets. Note the x-axis is measuring angles East of North, hence the apparent reversal in the positions of the red and blue groups when compared to previous figures.

Figure 3.12 presents this distribution superposed on a visual extinction map of the region calculated from the 2MASS survey (Schneider et al., 2011). Obvious structures within the distance distribution of sources are identifiable within the cloud complex. For example, Gaia DR2 164422961683000320, which lies within the south-eastern area identified as B10 (part of the extended L1495 cloud), is seen here to lie at 126.4±1.6 pc, which is consistent with the value of 126^{+21}_{-16} pc found earlier by Bertout, Robichon, and Arenou (1999). The region around B10 can thus be seen to be part of the 'near' population, and the 31 sources associated with the 'near' group within B10 are found to have a mean distance of 131.9±3.2 pc, with a standard deviation of 5.0 pc.

Lying to the south-east of B10 are the B211/B213 filaments. There are a number of sources from both populations which lie directly within, or close to these structures. It is apparent that, if these sources are genuinely associated with the filament then there appears to be a double distance gradient along this structure. One interpretation of this apparent double gradient is that the cluster of 'far' population sources seen half-way along the filament, are actually background to it. For this to be the case, there would need to be gaps in the foreground cloud that allowed the background cloud to be seen. This explanation would be consistent with the findings of Hacar et al. (2013), if one interprets their line-of-sight velocity with distance. This hypothesis is pursued

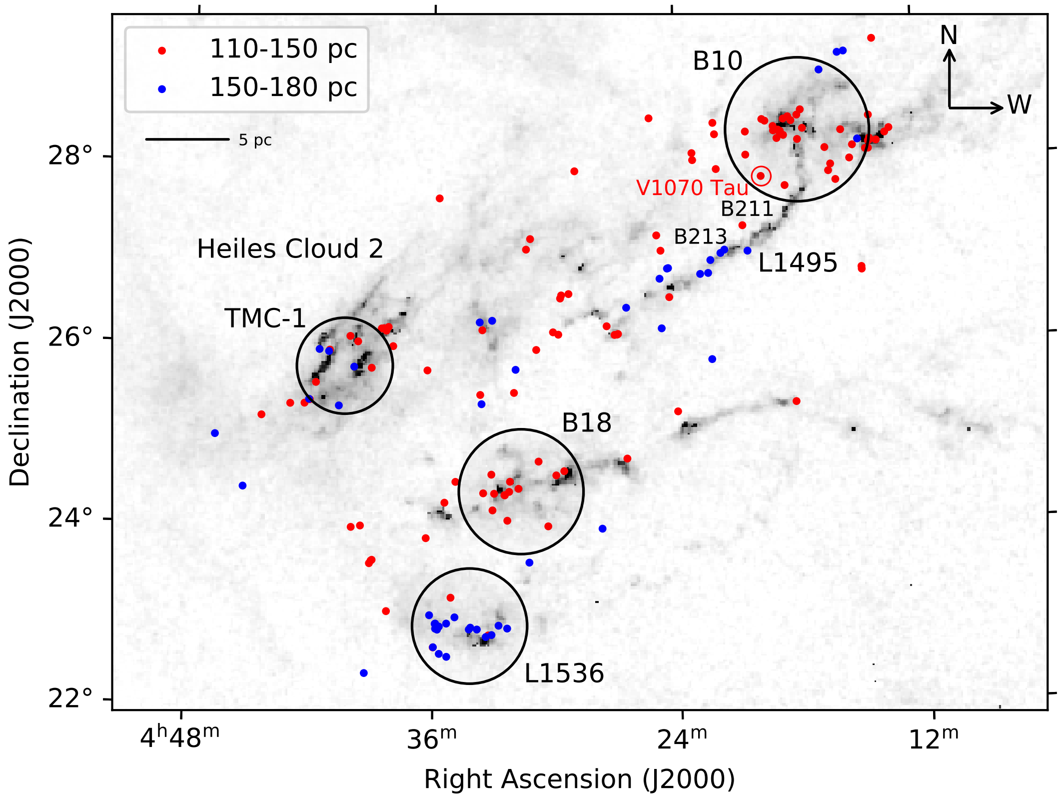

Figure 3.12 Spatial distribution of *Gaia* DR2 sources identified in the *Spitzer* SSTtau catalogue, using appropriate selection criteria (see text for details). Sources have been identified according to distance and overlaid on a visual extinction map calculated from the 2MASS survey Schneider et al. (2011). The colour coding is the same as previously identified. It can be seen that both B10 and B18 are dominated by sources in the 'near' group. L1536 is predominantly composed of sources from the 'far' population (see text for further discussion).

further in §3.4.3 below. Cloud B18 appears to be populated with a discrete population belonging to the 'near' group. Analysis of the data for this group shows that they are lying at a mean distance of 127.4 pc, with a standard deviation of 7.9 pc.

Looking at L1536, the VLBA derived parallax to the star HP Tau/G2 (Gaia DR2 145213192171159552) provides a distance of 161.2±0.9 pc (Torres et al., 2009). HP Tau/G2 also appears in the Galli et al. (2018) study with a derived mean distance of 162.7±0.8 pc, which is within 3σ of the *Gaia* value of 165.9±1.3 pc. This star is embedded within the reflection nebula GN 04.32.8, which appears as a crescent-shaped feature in the Herschel column density map of L1536 (Kirk et al., 2013). HP Tau/G2 lies within the area of L1536 (Figure 3.12). There are 20 'far' group sources identified in this area with a mean distance of 160.3±3.7 pc, and a standard deviation of 6.8 pc. The clear interaction of HP Tau/G2 with L1536 strongly implies that L1536 is at a comparable distance (Kirk et al., 2013). This is also supported by the earlier study of Bertout, Robichon, and Arenou (1999), which placed the southern region of the Taurus cloud at 168^{+42}_{-28} pc. There are also two members of the 'near' population situated within the L1536 area. These are Gaia DR2 145238687096970496 and Gaia DR2 145157937416226176 which have distance determinations of 130.0±2.3 and 140.3±4.2 pc respectively. When considering their maximum distances, they do not fall within the lower boundary of the 'far' group and we discount them as not being members of L1536.

The association of the 'near' and 'far' groups with the discrete structures within the Taurus cloud is graphically highlighted by Figure 3.12. With the addition of the *Gaia* DR2 derived distance data we are able to develop a three-dimensional picture of this region. Figure 3.13 shows the spatial distribution of the 'near' and 'far' groups within the equatorial coordinate system. From this perspective the sub-structures within the TMC are clearly seen, especially the regions associated with the B10 and L1536 clouds as the red and blue grouped populations in the top-right and bottom-left regions of the 3-D cube show.

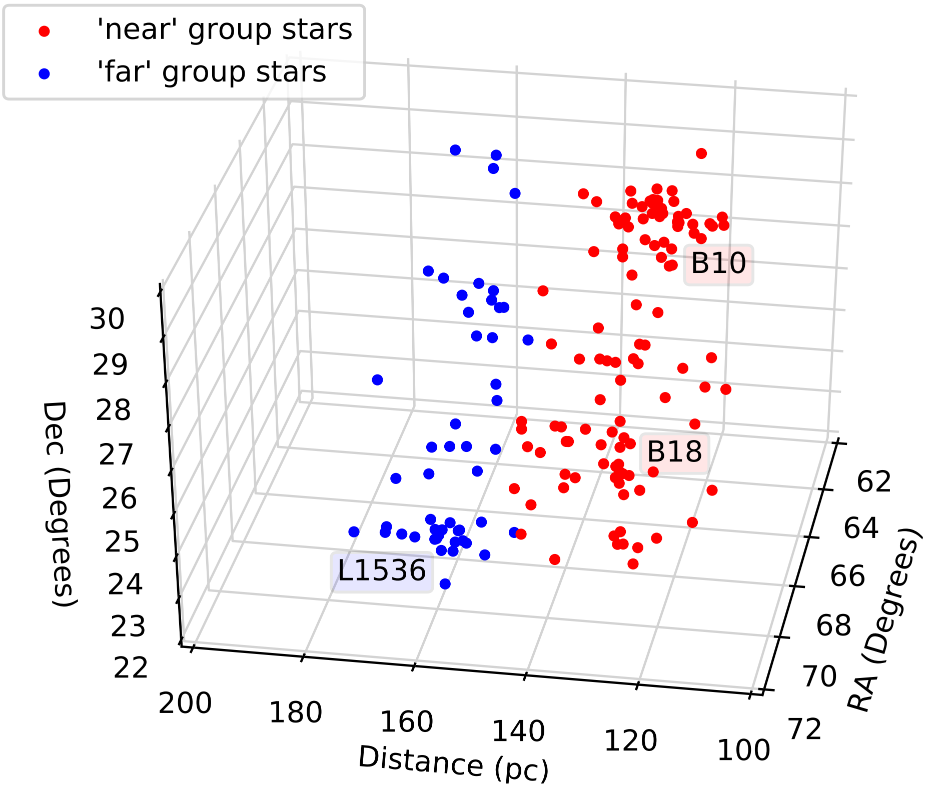

Figure 3.13 'Near' and 'far' groups plotted in 3-D space using equatorial coordinates. Over-densities associated with identifiable cloud structures are clearly seen.

As well as the three-dimensional format presented in Figure 3.13 it is also possible to examine the spatial structure of the 'near' and 'far' groups in the Galactic reference frame. Using the `SkyCoord` module within the `Astropy` common core package for astronomy, the study area can be investigated using the Cartesian (XYZ) system of Galactic coordinates rather than the celestial ICRS right ascension and declination shown in Figure 3.13.

Minimum spanning tree algorithms can be used to investigate the minimum (shortest) length, or 'distance' between objects in a population. In this way associated objects can be grouped together and defined by their distance from each other. Using this technique it is possible to identify related stellar associations through their distances from each other.

Figure 3.14 presents a minimum spanning tree showing our 165 sources in the Galactic reference frame. Of interest here are the lower panels which plot Galactic Z-Y and X-Y with the colour plots ordered by Right Ascension. The 'near' and 'far' group affiliations previously noted in the ICRS reference frame are clearly seen in Cartesian space suggesting that the TMC is consistent with a structure similar to that of an inclined sheet facing away from us, as suggested by Shimajiri et al. (2019) in their conclusions regarding the gas cloud surrounding the B211/B213 filament.

3.4.2 TMC-1 The Taurus Molecular Ring (TMR)

Here, the TMC-1 region is considered in more detail (see Figure 3.12). The area commonly referred to as the 'Bull's Tail' (Nutter et al., 2008) lies within a region known as Heiles Cloud 2 and has been the subject of many previous investigations (Hartigan and Kenyon, 2003; Tóth et al., 2004; Nutter et al., 2008; Malinen et al., 2012).

The region referred to in the literature as the 'Taurus Molecular Ring' (TMR) is shown to the east of $4^h\ 36^m$ in Figure 3.15. It can clearly be seen that objects in this area have a spread in distance of some 10 to 15 pc, with members of both the 'near' and 'far' populations being represented. This study is thus able to support the supposition made by Nutter et al. (2008) that the TMR is not a coherent structure but is rather a fortuitous alignment composed of disparate sources at different distances spread throughout the depth of the complex.

Objects Gaia DR2 148401565437820928 and 148400229703257856 lie towards the central region of the 'Bull's Tail' and have *Gaia* DR2 distances of 136.3±8.2 and 136.9±2.1 pc respectively, which are in general agreement with previous studies. Lying in the southern region of the 'Bull's Tail' is Gaia DR2 148374391180009600 which is a member of the 'far' group with a distance determination of 149.3±5.3 pc.

3.4.3 Velocity distributions within the TMC

Here, the 'true' proper motions of our two populations are discussed in the context of previous studies.

Distance & line-of-sight velocity comparison

In this section the three-dimensional nature of the TMC is presented with reference to existing line-of-sight velocity measurements of the region since it is well-established that the TMC has a complex velocity structure (e.g. Clark, Giguere, and Crutcher, 1977). In the context of the *Gaia* distance

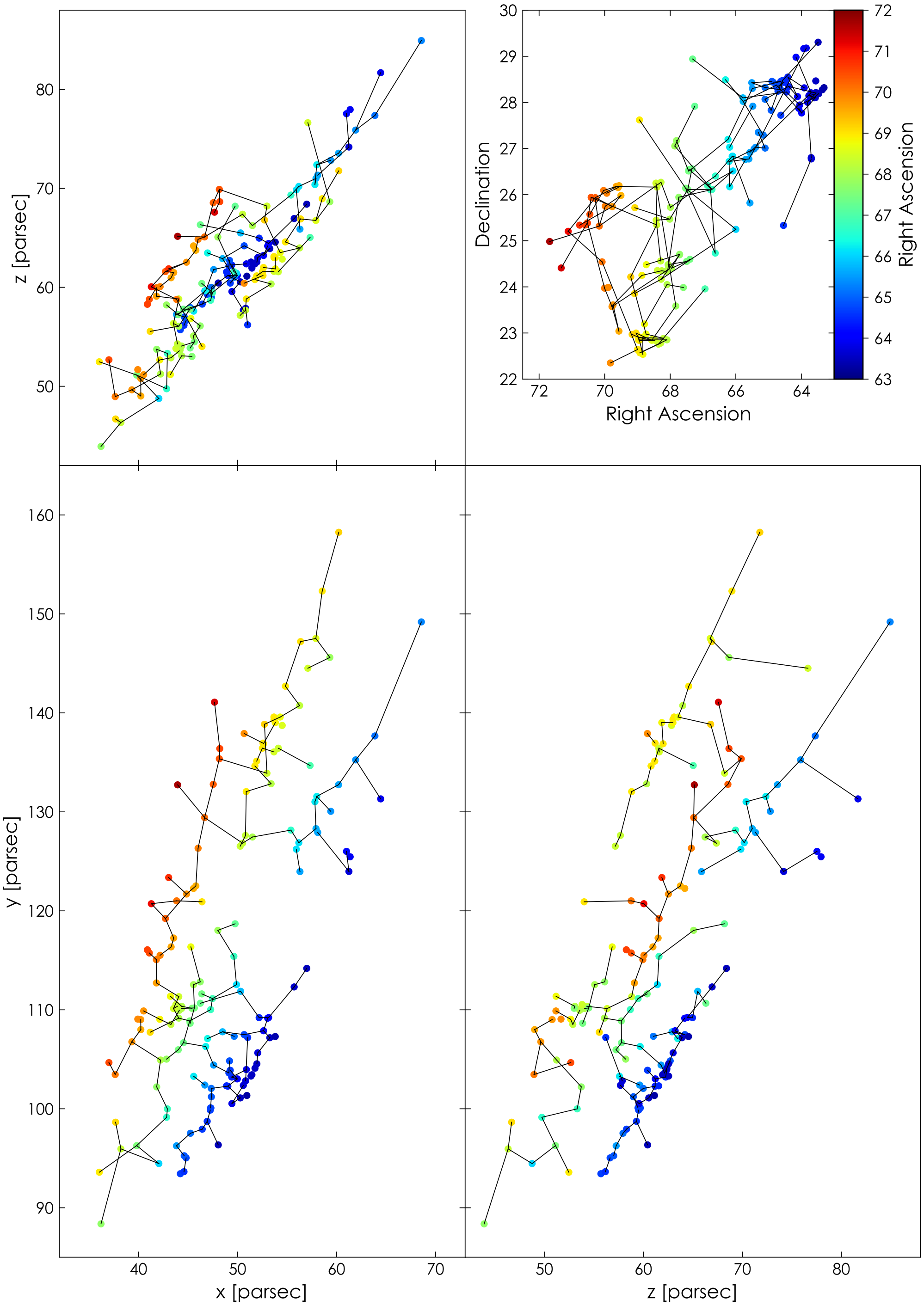

Figure 3.14 Distribution of 165 sources in the Galactic reference frame. The lower panels suggest that the stellar distribution resembles a 'sheet like' structure (see text).

observations, it is useful to undertake a comparison of the stars in our 'near' and 'far' groups with the major line-of-sight velocity components of the cloud.

The ^{12}CO emission associated with the TMC has systemic line-of-sight velocities ranging from 0-12 km s^{-1}, with the large majority of the emission having velocities in the range 4-8 km s^{-1} (Narayanan et al., 2008). The TMC has an overall east-to-west velocity gradient, with the eastern parts of the cloud preferentially having a lower systemic velocity than those in the west

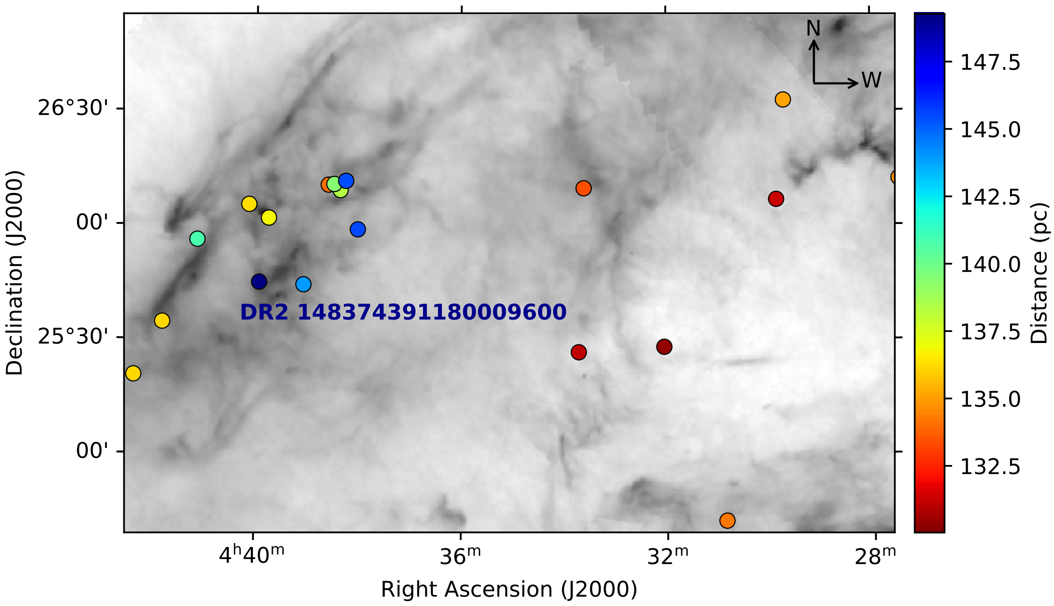

Figure 3.15 The region around the 'Bull's Tail' with sources colour coded by distance. The 'Taurus Molecular Ring' (in the east of the figure) has significant depth dispersion and is therefore not a coherent object.

(e.g. Goldsmith et al., 2008). However, there is a great deal of variation within this broad east-to-west trend. Particularly, the L1495 filament is known to have two distinct velocity components, separated by $\sim$1.5 km s^{-1} (e.g. Heiles and Katz, 1976; Clark, Giguere, and Crutcher, 1977). Hacar et al. (2013) used IRAM 30m telescope $C^{18}O$ observations to further separate these two components into multiple sub-filaments, with one set of sub-filaments having velocities $\sim$5-6 km s^{-1}, and the other having velocities $\sim$7 km s^{-1}. The well-defined plane-of-sky morphology of the L1495 filament is at odds with its apparent lack of velocity coherence, leading to suggestions that the 'filament' is in fact an edge-on sheet (e.g. Palmeirim et al., 2013). This is supported by the recent proposal of Shimajiri et al. (2019) that the B211/B213 filament system was initially formed through large-scale compression's from the Perseus OB2 association. Earlier studies (Könyves et al., 2007: Figure 8) suggest that the TMC is situated exactly at the wall of the Local Bubble raising the possibility that the 'sheet-like' Taurean cloud structure is the result of compression by the Per OB association in one direction and by the Local Bubble in the opposite direction.

Contradictory research (Li and Goldsmith, 2012), compared volume densities derived from dense gas tracers with 2MASS-derived column densities, and found that the high-density portion of the L1495 'filament' has a plane-of-sky depth of only $\sim$0.12 pc, suggesting that it is in reality a roughly cylindrical structure.

The stars associated with the TMC included in the *Gaia* DR2 catalogue are located at intermediate visual extinction and are therefore not associated with the densest star-forming gas. The distribution of the stars in our two distance groups are therefore compared to the velocities measured in ^{12}CO FCRAO observations of the TMC (Narayanan et al., 2008; Goldsmith et al., 2008). These observations traced moderately dense gas ($n(H_2)$ ~10^2-10^3 cm^{-3}) which is definitively associated with the TMC (see Figure 3.16), but which is not gravitationally unstable and actively forming stars (e.g. di Francesco et al., 2007).

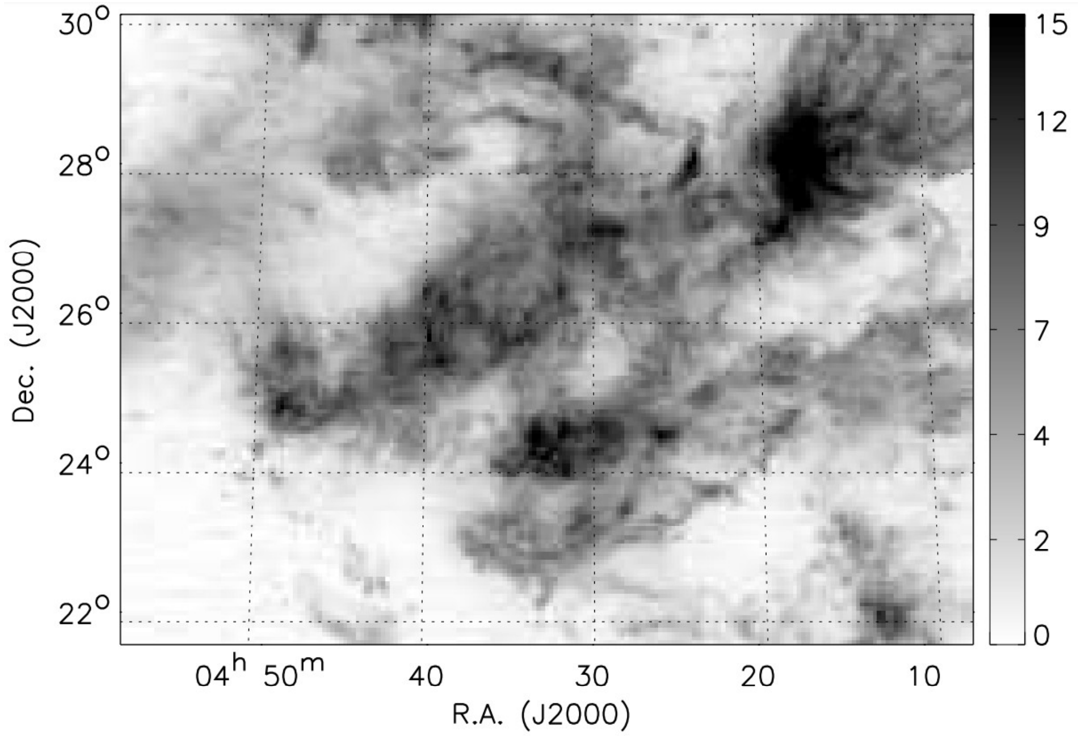

Figure 3.16 Integrated Intensity image of the ^{12}CO $(1 \rightarrow 0)$ transition over the range -5 to 20 km s^{-1}. The colour scale on the right shows the integrated intensity scale in K.km s^{-1}. From Narayanan et al. (2008): Figure 5.

^{12}CO velocity channel maps presented by Narayanan et al. (2008) show that the B10 and B18 regions have systemic velocities ~7 km s^{-1}, while the L1536 region has a systemic velocity ~5 km s^{-1}. The L1495 filament shows a double-peaked velocity structure, as discussed above. The TMC-1 region also has multiple velocities, with some suggestion that the eastern side of TMC-1 is at a lower systemic velocity (~5-6 km s^{-1}) than the western side (at ~7 km s^{-1}).

There is a striking similarity between these behaviours and the spatial distribution of the stars in our ‘near’ and ‘far’ groups (see Figure 3.12). B10 and B18 are both dominated by ‘near’ stars and have a systemic velocity of ~7 km s^{-1}, while L1536, containing ‘far’ stars, has a systemic velocity of ~5 km s^{-1}. The L1495 filament, with its two velocity components, contains stars from both groups, as does TMC-1. However, in TMC-1 the ‘far’ stars are preferentially located in the east, while the ‘near’ stars are preferentially located in the west, corresponding to a velocity gradient from ~5-7 km s^{-1}

across the region. There is thus a qualitative tendency for 'near' stars to be associated with $\sim$5 km s^{-1} sight-lines, and for 'far' stars to be associated with $\sim$7 km s^{-1} sight-lines.

The results presented here tentatively suggest that the two main velocity components of the gas in the TMC are located at different line-of-sight distances, with the $\sim$5 km s^{-1} gas being located in front of the $\sim$7 km s^{-1} gas. The 'gaps' in the L1495 filament hypothesised in §3.4.1 are also seen in the velocity data.

Velocity vectors within the TMC

The right ascension and declination proper motions of our sample sources are detailed in Appendix C (Table C.1). When these values are converted into vectors, as shown in Figure 3.17a, a small difference in the vectors between the two populations is apparent. The mean values of proper motion for each population and their standard deviations are given in Table 3.3. The arrows indicate the direction of motion of the objects.

For a meaningful analysis of the relative proper motions to be made, the influence on these motions caused by the relative solar motion needs to be taken into account. It is therefore necessary to calculate the mean motion of the entire sample, which will be dominated by the relative solar motion, and subtract this value from each of the individual star's proper motion. Figure 3.17b plots the individual velocity vectors for the members of each group after subtracting the mean overall motion of the Sun relative to the TMC, and a clear distinction can be seen between the two groups. The arrows here indicate the proper motions of the stars, relative to this overall motion between the Sun and the Taurus cloud.

Considering Figure 3.17b, one star stands out from the rest. Within the 'far' population, HD 30067 (Gaia DR2 147248216395196672) is found to have a markedly different velocity profile to the rest of its group. This star is recorded in SIMBAD as being an A2/4 class star (Hou et al., 2015) located at 163.5$\pm$1.4 pc with a proper motion of μ=16.1 mas yr^{-1}. *Gaia* DR2 indicates a G-Band magnitude of 8.9 mag and an extinction of 4.5 mag for this source. We suggest that, although this star meets the distance and proper motion criteria described earlier, HD 30067 is actually a field star and not associated with the Taurus group.

For a proper consideration, removal of the effect of Galactic rotation on the proper motions of our groups must also be considered. The literature notes that this transform is particularly sensitive to the Oort constants used (Oort et al., 1927; Olling and Dehnen, 2003), in particular the 'V' component of the solar motion relative to the Local Standard of Rest, which seems variable to a factor 2 depending upon the observer.

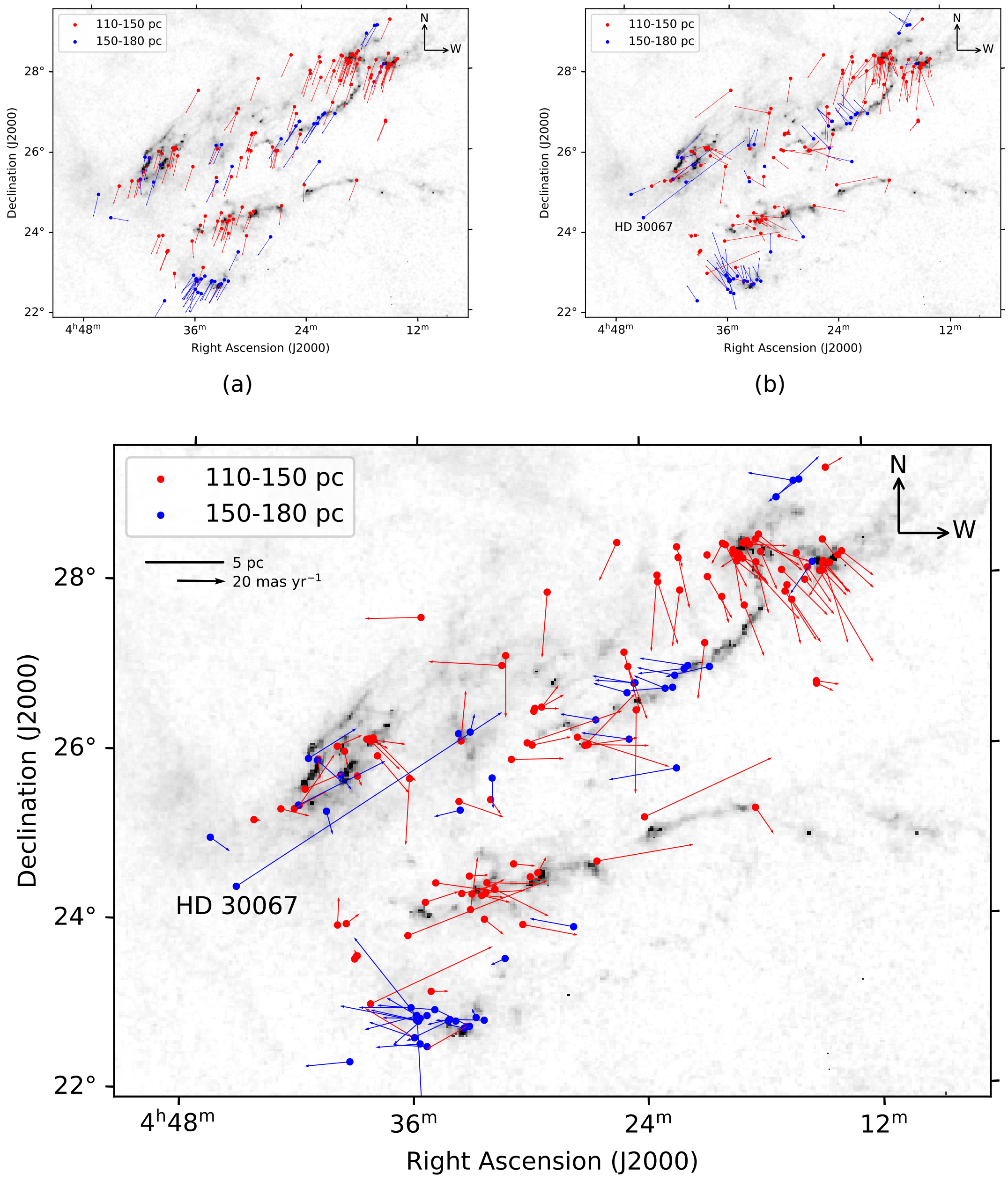

(c)

Figure 3.17 Group distributions and velocity vectors within the TMC. (a) Proper motions of the 'near' and 'far' groups identified in Figure 3.4. Individual star proper motions are displayed as vectors showing direction and relative magnitude of velocity. (b) Individual proper motions after the overall mean proper motion has been subtracted. (c) Proper motions after the removal of solar and galactic motions towards Taurus.

For this exercise the value of Oort constants from Li and Goldsmith (2012) and the Solar velocities from Schönrich, Binney, and Dehnen (2010) are adopted as is the convention for using solar velocities in the Galactic coordinate system as: U being the component toward the galactic centre; V the component along the line of galactic rotation; and W being the component out of the plane, towards the galactic north pole (see Figure F.7).

Since it is also necessary to use a rotation matrix in transforming between celestial ICRS RA/Dec and Galactic l/b coordinates the technique presented in Li, Zhao, and Yang (2019) is used. The treatment of barycentric stellar motion in astrometric and radial velocity data is also considered. The rigorous treatment of the epoch propagation including the effects of light-travel time was developed by Butkevich and Lindegren (2014). However, for the propagation of the prior information to the *Gaia* reference epoch, it is sufficient to use the simplified treatment, which was employed in the reduction procedures used to construct the Hipparcos and Tycho catalogues. This is only possible since the light-time effects are negligible at milliarcsecond accuracy. The resultant velocity vectors of the two groups, taking Galactic rotation into account is presented in Figure 3.17c.

The treatments of proper motion velocity vectors presented in Figure 3.17 clearly show a marked difference in the proper motions of the two populations, in particular those members of L1495 and L1536. In an X-Ray survey, Briceno et al. (1997) suggested that a population of stars discovered during the ROSAT mission (Trümper, 1985), located to the south of the Taurus clouds, might be an older population and have a different origin from the rest of the cloud, as well as being located at a different distance to the then commonly accepted distance of 140 pc. Our initial findings tend to support these ideas and further suggest that there may be a dynamic link between L1536 and L1495, particularly the B213 region.

3.5 Summary

This preliminary study has shown, through the use of trigonometric parallaxes from *Gaia* DR2 and the *Spitzer* catalogue, that there are significant differences in the distances to different structures within the Taurus molecular cloud complex. Since *Spitzer* conducted its survey in the infrared, the results we have used here have been more sensitive to radiation from Class II and some Class III YSO's as their discs become too diffuse to be detected. Since they are more enveloped in their discs it is unlikely that this study has identified either Class O or Class I objects although some Class I YSO's may be included as their discs begin to dissipate and they become visible (see Appendix F.1.1).

Nevertheless, two main associations have been located at 130.6$\pm$0.7 and 160.2$\pm$0.9 pc. These groups have different proper motions of 24.5$\pm$2.8 and 20.1$\pm$2.4 mas yr^{-1} respectively, and they appear to be moving in somewhat different directions. They also appear to have slightly different line-of-sight velocities. These newly recognised, discrete populations have been called here the **'Two Horns'** of Taurus.

With this new data it has also been possible to confirm that the so-called 'Taurus Molecular Ring' is not a coherent feature but has an extended depth of approximately 15 parsecs. Also, it is tentatively suggested that the structure of the TMC, in general, resembles that of an inclined sheet facing away from the observer.

A more detailed analysis of the region, using the complete data set obtained with our original query, is the main focus of this study and is discussed in the following Chapter.

4 UNBIASED *GAIA* DATA ANALYSIS

4.1 First look

Returning to our original sample of 7587 sources, obtained from the *Gaia* Archive query (Listing B.2), the 110–150 pc and 150–180 pc distance limits for the 'near' and 'far' groups were applied along with the proper motion limits of 12–40 mas yr^{-1} that were determined during our preliminary look at the data in Chapter 3. This filtering exercise identified 2372 sources within the limits stated.

Running this data set through the `Python` routines developed earlier produced the distributions presented in Figure 4.1 where it can be seen that the distance (Figure 4.1a) and proper motion (Figure 4.1b) distributions are not as well defined as in our preliminary study and contain numerous, possibly unassociated field sources.

Contrasting the result displayed in Figure 4.1b with that obtained in our preliminary study (Figure 3.10) shows a much wider, almost equal distribution of both 'near' (red) and 'far' (blue) sources across the field shown, suggesting that many of the field sources apparent in Figure 4.1a fall within the 12–40 mas yr^{-1} limits of this study. The discrete distributions identified earlier (Section 3.3) are still evident and interestingly, a closer examination shows a possible third grouping (of 'far' sources) centred around (5, -25) mas yr^{-1}.

By comparing Figure 4.1a with a figure showing all 7587 sources before filtering is applied (see Figure 3.2) it is apparent that some reduction in numbers has taken place. It is also apparent that further sampling and data reduction needs to be done before a clearer picture of the distributions can be obtained.

4.2 Data Reduction

In their discussion on generating evolutionary diagrams for stellar populations using *Gaia* DR2 data, Babusiaux et al. (2018) presented a set of filters designed to ensure the accuracy of their Hertzsprung-Russell diagrams. These filters perform a number of functions, namely:

- *visibility_periods_used>8*, which ensures that the five-parameter solution described by Lindegren et al. (2018) is met. This filter also has the effect of removing strong outliers at the faint end of the CMD Arenou et al. (2018);
- *astrometric_chi2_al/(astrometric_n_good_obs_al-5)<1.44*greatest(1,exp(-0.4*(phot_g_mean_mag-19.5)))*, which filters the astrometric excess noise

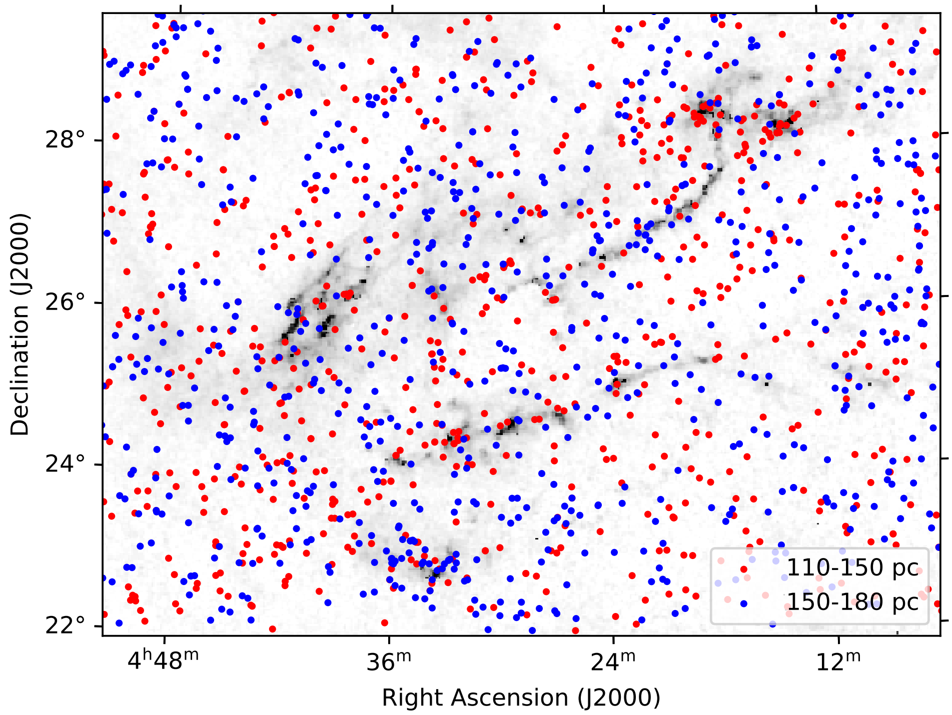

(a)

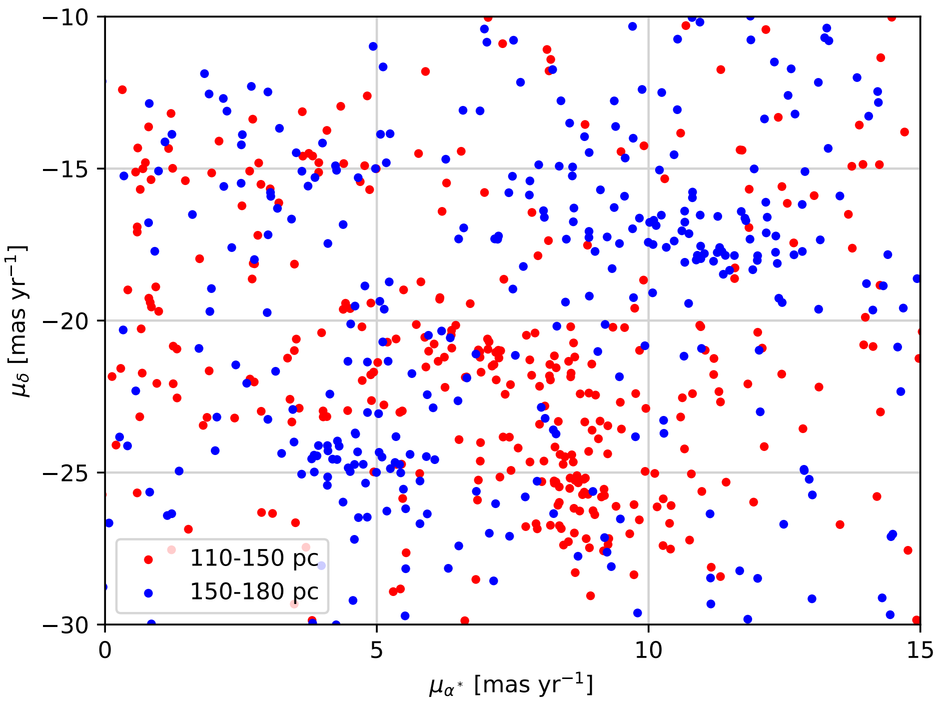

(b)

Figure 4.1 Distance (a) and proper motion (b) distributions for 2372 sources obtained through filtering of the *Gaia* Archive results. Both plots have been colour coded according to the scheme identified in our preliminary study.

and removes artefacts, particularly between the white dwarf region and the main sequence;

- *parallax_over_error*>10, which limits the relative precision on the parallax values of 10% to ensure an uncertainty on the *Gaia* absolute magnitude smaller than 0.22 magnitude;

- *phot_g_mean_flux_over_error*>50 AND *phot_rp_mean_flux_over_error*>20 AND *phot_bp_mean_flux_over_error*>20, to ensure that variable stars are removed, and
- *phot_bp_rp_excess_factor*<1.3+0.06*power(*phot_bp_mean_mag-phot_rp_mean_mag*,2) AND *phot_bp_rp_excess_factor*>1.0+0.015 power(*phot_bp_mean_mag-phot_rp_mean_mag*,2), to make certain that the contribution of flux from nearby bright sources is taken into account.

Applying these filters to our 7587 cohort reduced the source count to 3926. This number was further reduced to 1245 once our distance and proper motion limits were applied.

In our preliminary study, through the use of archival *Spitzer* data, we were able to present two, previously unidentified, groups of YSO's. Since this was primarily based on infrared observations it was more sensitive to early Class II and Class III objects. We now consider a similar study exclusively using *Gaia* optical results which will identify more developed Class II and Class III objects (see Appendix F.1.1). Previous studies in the literature provide useful insights into how this new group can be investigated further.

Gouliermis et al. (2006) conducted a photometric study of the star-forming region NGC 346 and its surrounding field in the Small Magellanic Cloud. In their first-order characterization of the observed stellar species they identified a clear turn-off point around $V \simeq 22$ mag between the upper and lower main sequence. Importantly, they identified a region to the right of the lower main sequence containing a concentration of low-mass stars which they speculated might be pre-main sequence (PMS) stars. This possible location of PMS stars was further discussed by Kenyon, Gomez, and Whitney (2008) in their study of the structure of star formation in the Taurus-Auriga dark clouds. In this study they identify previous works (e.g. Herbig, 1952) which suggest that pre-main sequence T Tauri stars are located 1 to 3 magnitudes above the main sequence.

Figure 4.2 presents a Colour Magnitude Diagram (CMD) of our sources using the findings of Gouliermis et al. (2006) and Kenyon, Gomez, and Whitney (2008) in an attempt to identify PMS sources in our population. In the following discussion it should be remembered that this study is considering the position of PMS stars within the Taurus star-forming region. In the TMC, extinction and reddening due to concentrations of dust and gas are sufficient to obscure and affect the apparent magnitude of sources and thereby their position on the CMD. This is also true of young stars that have circumstellar disks with significant amounts of dust, namely accretion on to the star from the disk creates a hot excess which makes blue photometry 'too blue', while thermal plus accretion emission from the inner disk makes red photometry 'too red'. It should also be remembered that, when solving for the astromtric parameters, *Gaia* sources are treated as single stars (Gaia et al., 2018). The TMC contains a large fraction of binary and multiple systems (e.g. Ghez, Neugebauer, and Matthews, 1993; Hartigan and Kenyon, 2003) and it is recognised that systematic errors deriving from unresolved multiplicity can result in luminosity (and therefore magnitude) overestimates (Simon, Ghez, and Leinert, 1993).

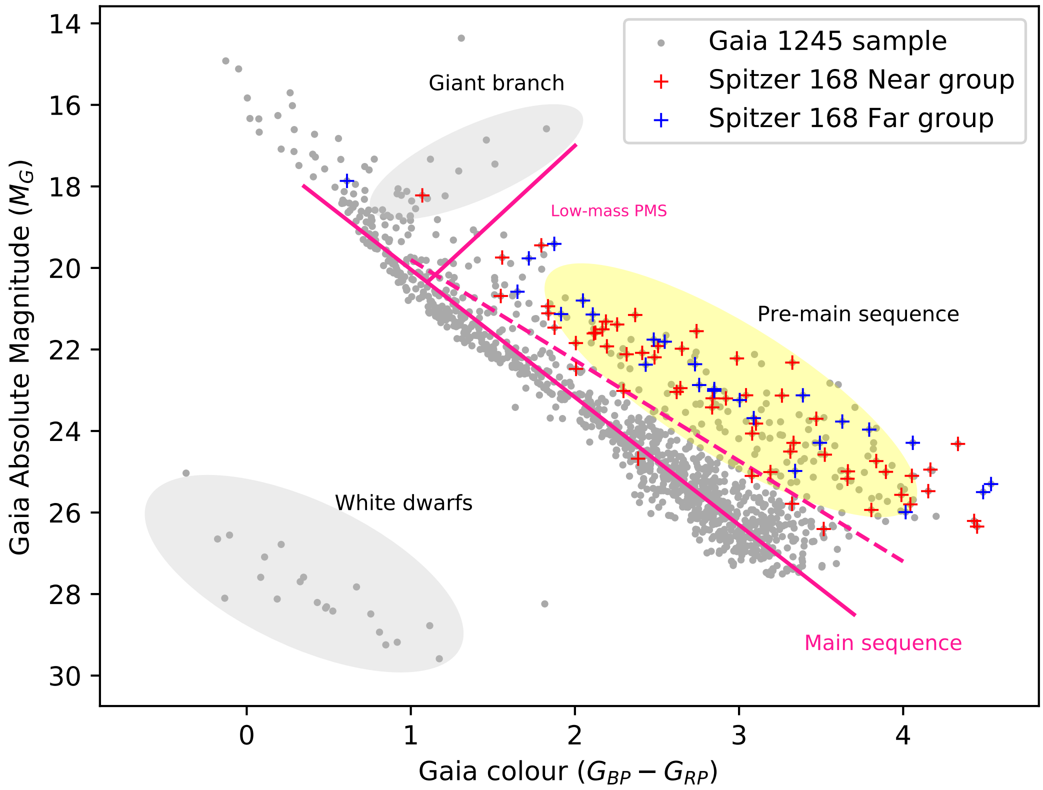

Figure 4.2 Colour Magnitude Diagram with *Gaia* 1245 cohort showing 'near' and 'far' groups from Chapter 3 (see text).

The diagram is plotted with G_{BP}-G_{RP} against the absolute *Gaia* magnitude in the G-band (M_G) for individual sources, with no correction for extinction, using the following expression to calculate M_G from the *Gaia* data, corresponding *Gaia* data field names are given in brackets:

$$M_G = \overline{M_m} + 5(log_{10}(p) + 1) \quad \textbf{(4.1)}$$

where $\overline{M_m}$ is the *Gaia* mean magnitude ($phot\_g\_mean\_mag$) computed from the G-band mean flux applying the magnitude zero-point in the Vega scale, and p is the *Gaia* parallax ($parallax$)

Figure 4.2 presents the CMD for our cohort of 1245 sources. The diagram is annotated with salient features and shows the Main Sequence (MS) line and our demarcation between the high and low-mass PMS. The dashed line denotes our demarcation between the MS and PMS - our subject sources lying above the line. We have overlaid the 'near' and 'far' groups from our preliminary study and it can be seen that the area above the dashed line contains the majority of the sources identified in Chapter 3 in support of the findings of Kenyon, Gomez, and Whitney (2008: and references therin).

There are two sources from our preliminary study in the region of the Giant Branch. These sources are Gaia DR2 164536250037820160 (HD 283572) designated by SIMBAD as a G5IVe Variable Star of Orion Type (Patterer et al., 1993) and Gaia DR2 147248216395196672 (HD 30067) an A2/4 star (Hou et al., 2015), from our previous 'near' and 'far' groups respectively. The location of these sources in the CMD suggest that these prospective YSO's are in fact giant stars which display an infrared excess in their spectrum, due to dusty winds caused by chromospheric activity, as noted in prior studies of YSO's in the Gould Belt (Dunham et al., 2015), the *Gaia* DR2 study of the Lupus V–VI clouds (Manara et al., 2018) and in the PhD Thesis study of Asymptotic Giant Branch (AGB) stars in the Milky Way galaxy (Martinavarro Armengol, 2015). Oliveira et al. (2009) report that such contamination by AGB stars can be as high as 26%, although other studies (e.g. Romero et al., 2012) have reported significantly higher figures depending on their study criteria.

Within the general PMS region identified in Figure 4.2 we find 192 sources, these sources are displayed in Figure 4.3 and detailed in Appendix D.

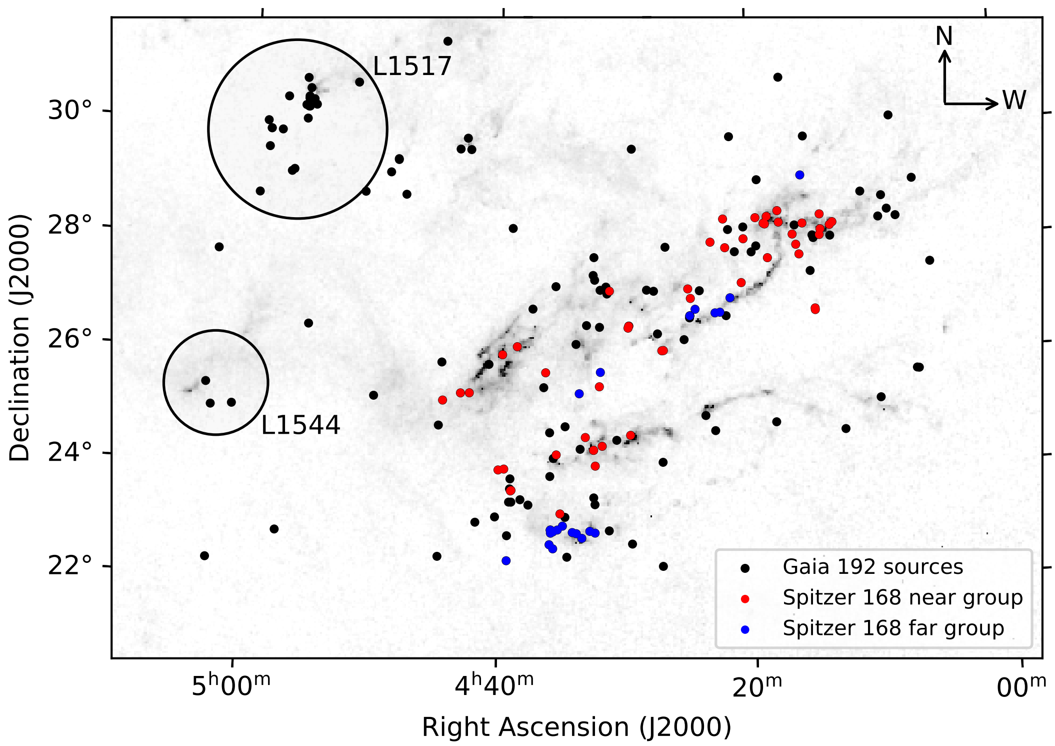

Figure 4.3 Spatial distribution of 192 sources with *Spitzer* 168 cohort overlaid. Out-of-study-area sources are clearly seen.

Figure 4.3 shows the full extent of the region covered by our initial *Gaia* Archive query. The 'near' and 'far' groups from our preliminary study have been overplotted to clearly show the new sources. It is apparent from the distribution that a significant number of the new cohort lie outside the chosen study area, some of which are identifiable as belonging to the L1517 and L1544 dark clouds. By confining these new sources to the region studied previously, 155 sources remain, of which 73 are common with the previously studied cohort of 161 sources and 82 are unique to this group. Details of these sources can be found in Appendix D and they form the basis for our continued investigation.

4.3 Follow-on Studies

Having identified the 155 *Gaia* sources to be used in this study the methods used in our preliminary study (see Chapter 3) are replicated to determine the population parameters. Having previously statistically verified the existence of two groups, we do not intend to duplicate these analyses.

4.3.1 The 'Two-Horns' distribution

As in Section 3.1, our distance sample is binned at 3 pc intervals between 110 to 180 pc for consistency. Figure 4.4 shows the distribution of our new 'near' and 'far' groups shown in magenta and cyan respectively to differentiate them from our preliminary study groups.

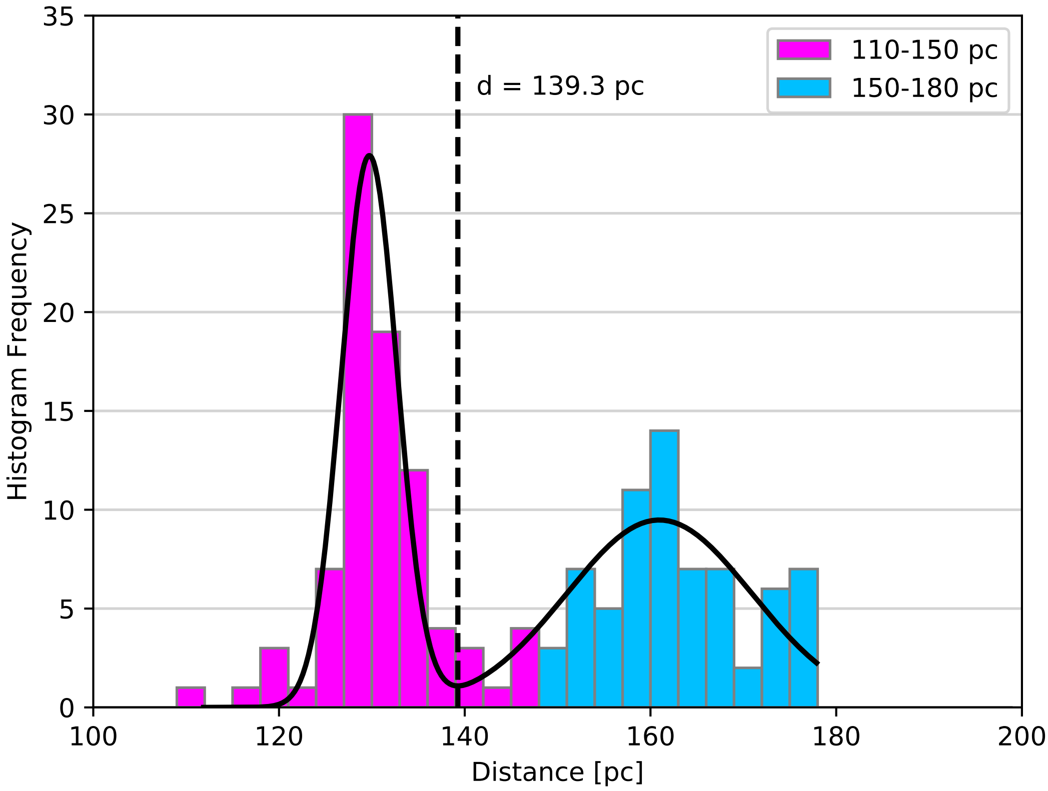

Figure 4.4 Two main populations are seen. A double-Gaussian curve is fitted identifying a minimum value. Following correction for outlying sources and adjustment of group members a new distribution of 142 sources is centered around 139.7 pc (see text).

Our initial analysis found the new populations centred at 139.3 pc, a difference of 8.6 pc from our preliminary study. In contrast to Figure 3.4 the bi-modal null does not fall naturally between the two distributions. This skew is possibly caused by the higher than expected number of sources in the two bins beyond 172 pc although it is also recognised that it may be an artifact of the binning process. Further investigation finds that the 'contaminating' sources belong to the L1517 group (Figure 4.3) and its outliers, which cannot be differentiated from our 'far' group. One consequence of this is that the 'minimum' boundary between the two groups now falls within the 'far' population rather than between the two groups as previously seen.

Redefining our 'near' and 'far' group limits as 106 to 145 pc and 145 to 172 pc respectively discounts 13 'far' group sources in the two bins beyond 172 pc (see Appendix D) and changes the affiliation of the bin at ~146 pc. These changes reduce our total source count to 142 with a mean distance of 139.7 pc (Figure 4.4). Of this group, 72 sources appear in our preliminary study whilst the remaining 83 sources are exclusive to this group. Our 'near' group in this study is centered on 130.0±0.6 pc and contains 82 sources whilst a more dispersed 'far' group is composed of 60 sources centered on 159.5±0.8 pc, these values remain within 1σ of the values obtained in our preliminary study. Specific values for each group can be found in Table 4.1.

	Near	Far
Number of Sources	82	60
Mean Distance [pc]	130.0±0.6	159.5±0.8
Standard Deviation [1σ]	2.9	11.8
$\mu_\alpha \cos\delta$ [mas yr^{-1}]	8.1	10.25
μ_δ [mas yr^{-1}]	-23.7	-18.9
μ_{Total} [mas yr^{-1}]	25.2	22.1
Standard Deviation [1σ]	3.4	4.5
Angle θ [degrees] (East of North)	161	151
Standard Deviation [1σ]	5	13

Table 4.1 Properties of the near (magenta) and far (cyan) populations after the distance and proper motion cuts have been made.

4.3.2 Scattering in $\mu_\alpha \cos\delta$ and μ_δ space

As completed in Section 3.3, an investigation into the proper motion distributions of our newly defined cohorts is performed using our previously defined limits of 12 mas yr^{-1} to 40 mas yr^{-1}. Figure 4.5 presents the pmRA, pmDec and μ profiles of our populations and is analogous to that found in Figure 3.7. The plotted responses reflect the smaller population sizes.

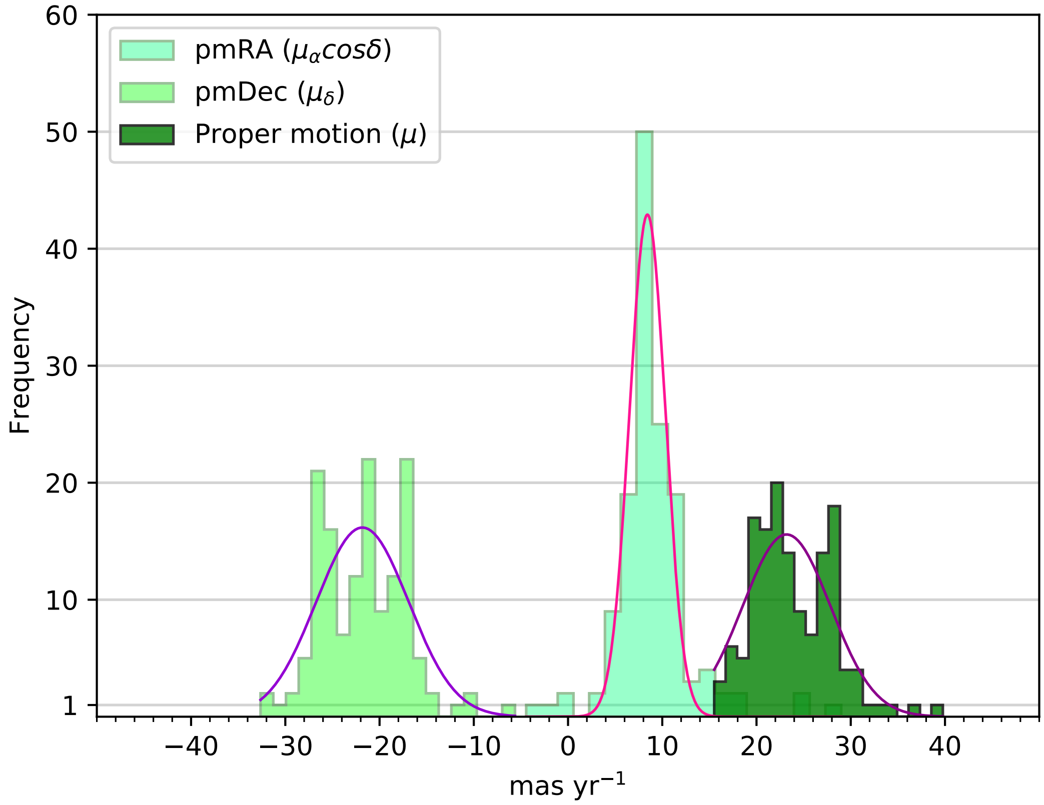

Figure 4.5 Proper motion distributions of the 142 *Gaia* sources.

The Gaussian responses shown in Figure 4.5 indicate that the proper motion (μ) is centred on 23.88 mas yr^{-1} with a standard deviation of 4.19, the contributory vectors pmRA and pmDec have values of 9.03 and -21.67 with standard deviations of 4.02 and 4.52 respectively. As seen in the preliminary study, the responses are almost symmetrical with pmRA, pmDec and proper motion skewness values of 1.38, 0.28 and 0.63 where a symmetric normal distribution has a value of zero. The skew value >1 returned by the pmRA response is a result of the high peak in the number of sources with values around ~8 mas yr^{-1}.

Figure 4.6 shows the locations of the two associations in μ_α and μ_δ space. The 'near' group is shown in magenta and the 'far' group in cyan, consistent with Figure 4.4. There is a suggestion in both Figures 4.6 (a) and (b) that the 'near' (magenta) population is itself formed of two groups, one with a pmDec vector of ~22 mas yr^{-1} and the other with a velocity of ~26 mas yr^{-1}. The greater dispersion of the 'far' group seen in Figure 4.4 is clearly apparent in Figure 4.6a and is also reflected in the position of the 'far' group centroid in Figure 4.6b.

Comparing the three peaks in the distribution of velocities shown in the pmDec response in Figure 4.5 with the distribution of the groups in Figure 4.6b (as noted above) suggests that, whilst both the 'near' and 'far' groups have an almost uniform motion in pmRA space, the three sub-groups have dispersed velocity vectors in the pmDec direction.

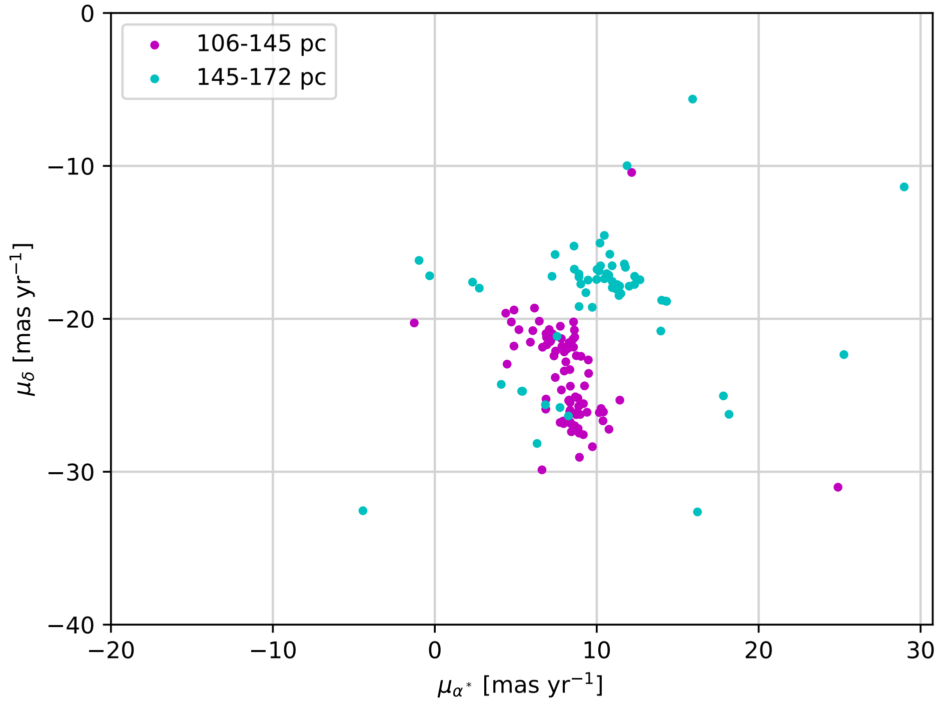

(a)

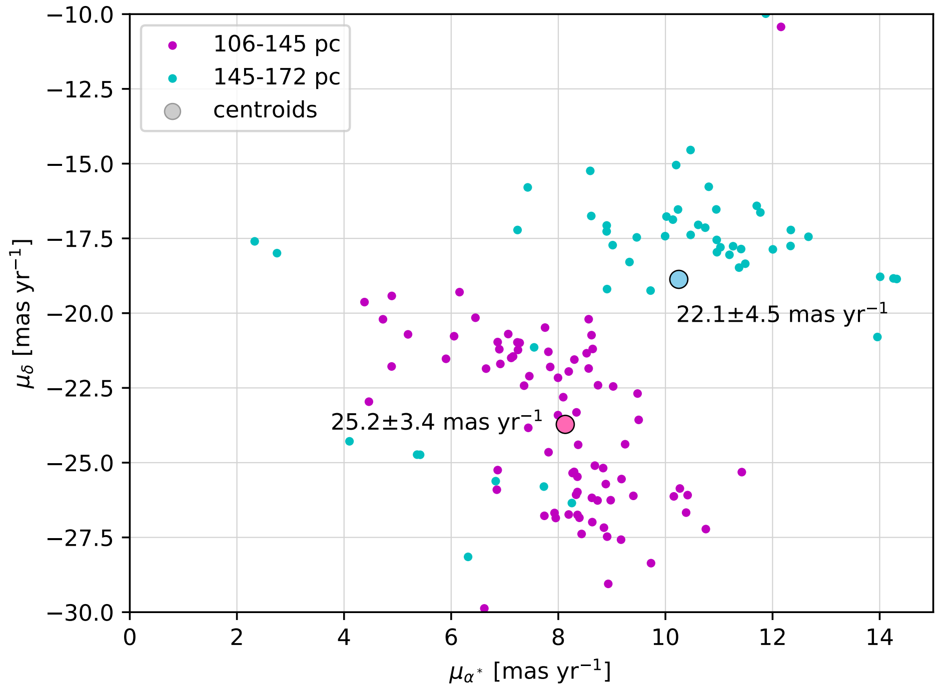

(b)

Figure 4.6 Proper motion distributions showing two populations which are consistent with the two distance groupings seen in Figure 3.4. (a) Proper motions of all 142 members of our 'near' and 'far' groups. (b) the central region of Figure 4.6a showing the centroids of each group.

The parameters discussed above are summarised in Table 4.1. The similarity of these results with those found in the preliminary study (Table 3.3) are evident.

4.3.3 ICRS Velocity vectors

Using the method previously described in Section 3.4.3 to remove the effects of solar and galactic motions, the ICRS velocity vectors have been calculated for our cohort of 142 sources and are presented in Figure 4.7.

In relation to other members of the 'near' group, it is immediately apparent that there are a number of high velocity sources with directions of travel different from the main body of the group. This is also true, but to a lesser extent, for members of the 'far' group. Convergent Point analysis, which studies the kinematic properties of group members which share the same spatial motion (e.g. Brown, 1950; Bruijne, 1999; Galli et al., 2012) would seem to suggest that these sources, as in the case of HD 30067 in our preliminary study, are not in fact members of their associated group.

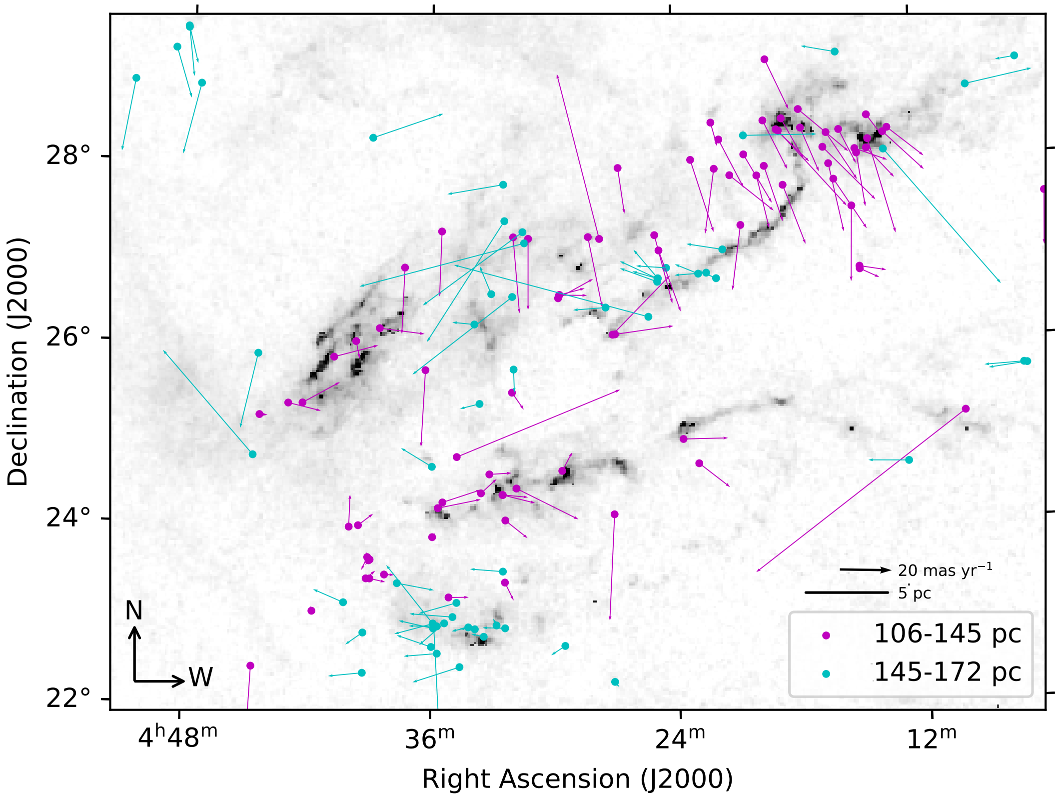

Figure 4.7 ICRS velocity vectors of sources identified in our *Gaia* 142 'near' and 'far' groups.

As also seen in our preliminary study, structures around B10 and B18 show high concentrations of 'near' group sources whilst the 'far' population is generally located around L1536 and is dispersed in filamentary structures throughout the region. Comparing the motions of these groups with those identified in our preliminary study (see Figure 3.17c) suggests that the vector directions displayed by the 'far' group are less coherent than those in our previous study.

4.4 Additional studies

In the following section, some of the complementary studies that have been undertaken to more fully understand the dynamics and kinematics of the region are described.

4.4.1 Redshift & V_{LSR}

The *Gaia* DR2 radial velocity (R_V) data set contains median R_V values averaged over the 22 months of observations (Gaia et al., 2018).

Comparing our two associations with the latest LAMOST data, which was released in June 2019, provides insights into their radial velocities i.e., their line-of-sight velocity (V_{LSR}) values. The Large Sky Area Multi-Object Fiber Spectroscopic Telescope (LAMOST) is a 4m Schmidt telescope operated by the National Astronomical Observatories, Chinese Academy of Sciences. For this study, data from release DR5_v3 which is available on-line[1] is used since it contains spectra for over 9 million sources along with a catalogue of general stellar parameters.

Velocity data were obtained by cross-matching the *Gaia* RA and Dec positional data for our 155 sources with the LAMOST DR5 using a separation radius of 2.0 arcseconds. This query returned 101 sources in common with our study, of which 98 (see Appendix E) contained redshift (z) values - 55 in our 'near' group and 42 in the 'far' group with mean z values of 6.98×10^{-5} and 2.92×10^{-5} respectively, giving an overall redshift value for the TMC in our study area of $z = 5.19\times10^{-5}$.

For such small values of z compared to 1.0 (the value of c_0) it is possible to convert from redshift to velocity (v) measured in km s^{-1} using the non-relativistic formula:

$$v = c_0 z \tag{4.2}$$

giving an overall mean recessional velocity for the TMC of 15.58 kms^{-1}.

Figure 4.8 presents the distribution of the *Gaia* 'near' and 'far' groups with respect to their redshift as given in LAMOST DR5.

Whilst the measured values are small there is a distinct difference in the redshift of the two groups. With a few exceptions, it is apparent that the 'far' group appears stationary whilst the 'near' group is moving away from the observer. To obtain a clearer understanding of the line-of-sight velocities involved, Equation 4.2 is used to obtain values for our cohort. The Gaia DR2 data contains 32 sources with radial velocity values and LAMOST DR5 has 98 that can be determined from their V_{LSR} values which define an objects mean velocity in the Milky Way, in the neighborhood of the Sun. Cross-matching these there are 22 sources in common with both data sets. Figure 4.9 shows

[1] http://dr5.lamost.org/

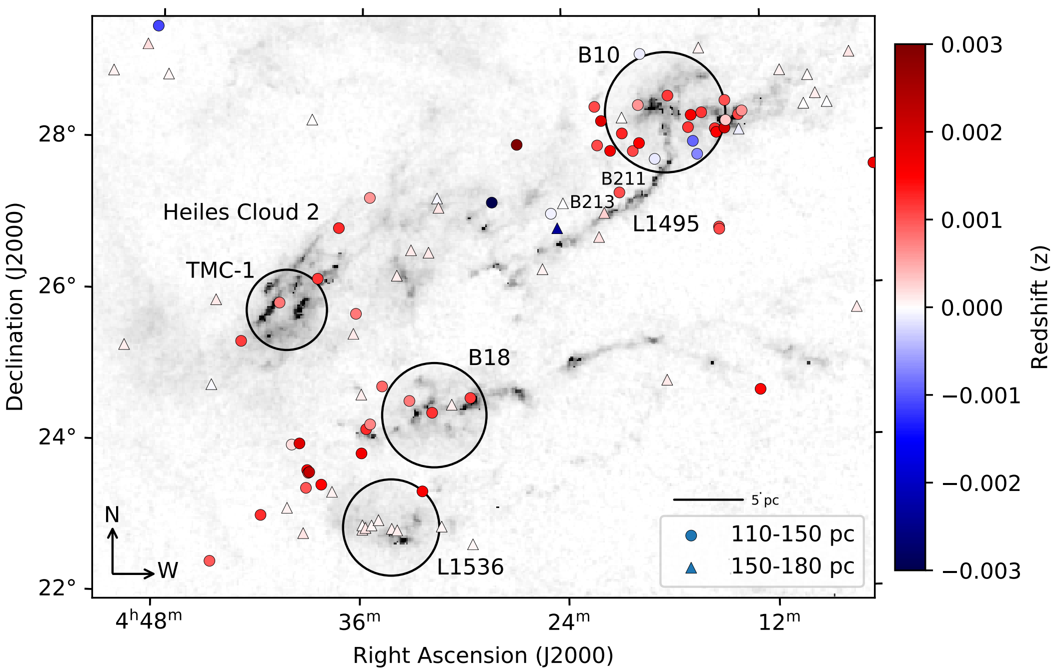

Figure 4.8 Redshift of sources identified in our *Gaia* 'near' and 'far' groups obtained from LAMOST DR5. It can be seen that the two groups have different values of z and hence recessional velocities.

the relationship between the radial velocity values (with errors) derived by *Gaia* and LAMOST.

There are three sources shown in Figure 4.9 that lie well beyond the linear relationship shown. These sources do not have a classification in SIMBAD, however in LAMOST DR5 they are recorded as being F-type stars. Although included in previous discussions in this study, there are no F stars associated with the Taurus group (Kenyon, Gómez, and Whitney, 2008; Rebull et al., 2010) and they can be discounted as members of our cohort.

The linear relationship seen in Figure 4.9 provides confidence that using the LAMOST DR5 as a proxy for *Gaia* allows a discussion of radial velocities to take place. Mooley et al. (2013) consider members of Taurus to have radial velocities in the region $9.8 \leq R_V \leq 17.5$ kms^{-1} in general agreement with the earlier study of Luhman et al. (2009a).

As previously noted (see Section 4.2), the TMC has a high multiplicity fraction, and as with the issues around observed magnitudes this can affect measurements of radial velocity (Cunha et al., 2013). Radial velocity variations are caused by the orbital motion of the stellar companion(s) and the resulting impact on the R_V calculation is a function of the difference between the main body R_V (R_V) and the secondary contaminant R_V (ΔR_V).

When considering radial velocity values it is also necessary to take the bulk gas motion of the TMC into account. The studies of Narayanan et al. (2008) into the structure and column densities of different regions of the

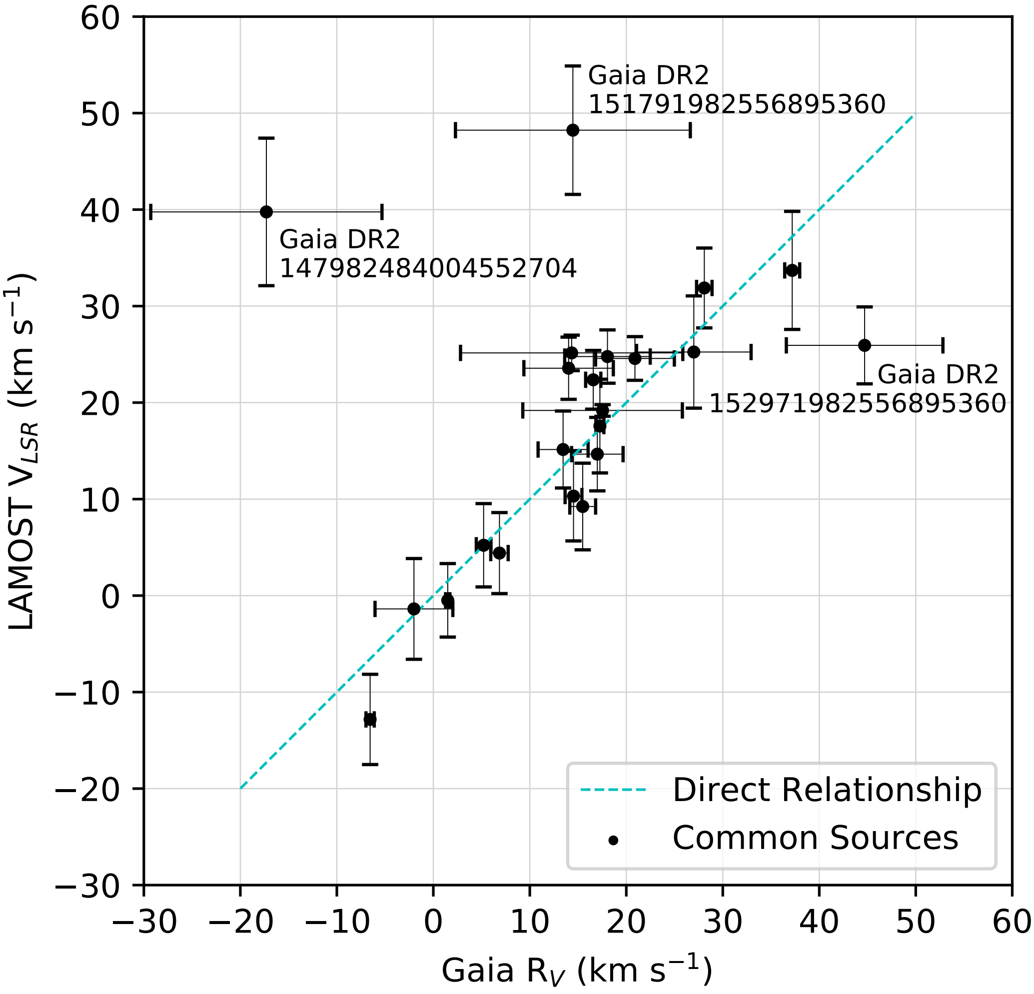

Figure 4.9 Comparison of *Gaia* DR2 radial velocity and LAMOST DR5 V_{LSR} data. There are 22 sources common to both surveys, the blue line shows a direct relationship between the two data sets. The three sources indicated do not have a *Gaia* classification but are all reported by LAMOST DR5 as being F-type stars.

TMC using ^{13}CO and ^{12}CO emissions, and the more recent work by Soma et al. (2018) looking at the rotational emission lines of the saturated CH_3OH organic molecule derive V_{LSR} values for the TMC of 6 kms^{-1} and 5.8 kms^{-1} respectively. Taking the value determined by Narayanan et al. (2008) and subtracting this from our derived values (i.e. $R_{V star}$ - $R_{V gas}$), it is possible to plot a histogram of V_{LSR} velocities for our 'near' and 'far' groups (Figure 4.10).

The distributions for both groups are plotted in Figure 4.10 with a bin size of 40 kms^{-1}. There are two sources with V_{LSR} in excess of -100 kms^{-1} not shown in the figure, one from each of the 'near' and 'far' groups. These are Gaia DR2 152178976290554496 (2MASS J04281566+2711110) an M5.5 Low-mass star (Esplin and Luhman, 2017) in the 'near' group with a velocity of -114.11 kms^{-1} and the 'far' group source Gaia DR2 152109054223716480 (SSTtau 042423.2+265008) an M3 Variable (Xiao et al., 2012) with a velocity of -711.40 kms^{-1}. Péricaud et al. (2017: Table D.1) indicate that this latter

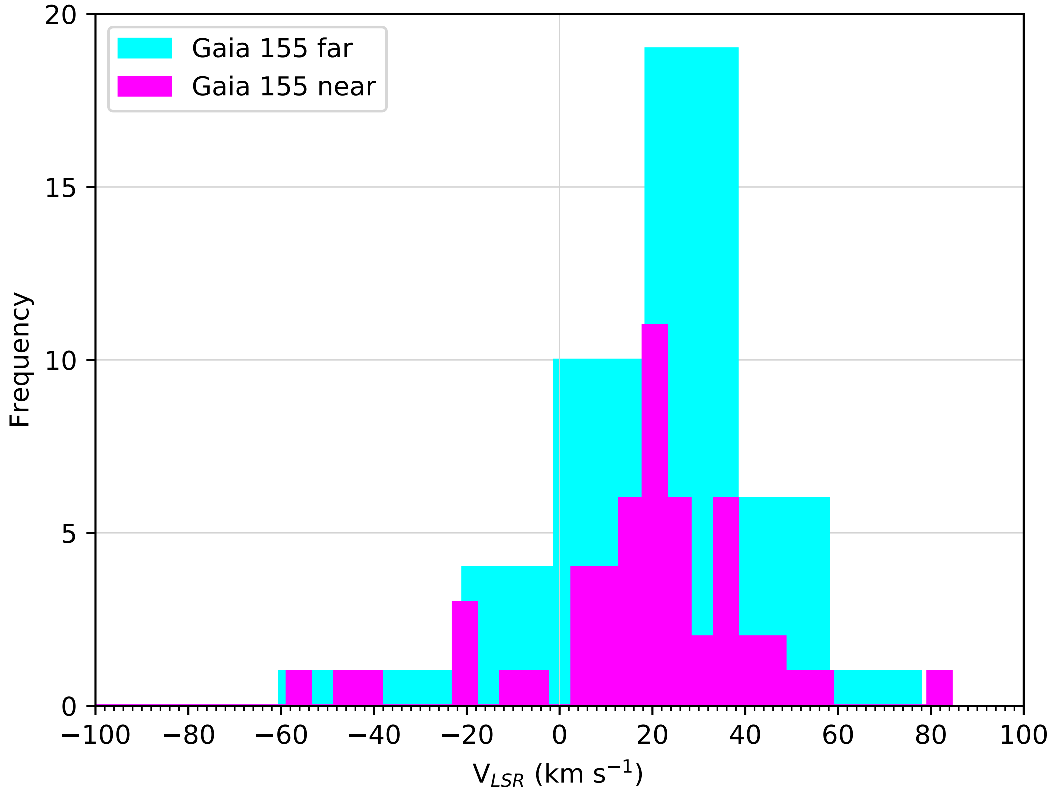

Figure 4.10 Vlsr distribution of our *Gaia* 'near' and 'far' groups showing a 'zoomed-in' view of our groups with outliers beyond -100 kms^{-1} removed.

source is a weak-line T Tauri (WTTS) star with a disk, suggesting the possibility that the presence of a rotating disk has adversely had an effect on the measured radial velocity of this star. The two sources mentioned above have not been shown in order to provide clarity on the main body of sources.

Figure 4.11 details the spatial distribution of our results with the radial velocity (V_{LSR}) scale centered on the velocity of the gas component of the TMC. Whilst the majority of sources studied are within a few kms^{-1} of this value it is notable that the 'far' group has velocities considerably in excess of this. There are a few exceptions to this in the upper central region of the map where high velocity sources from both groups can be seen, these sources may not be associated with the Taurus cloud. With our limited number of sources in discrete cloud locations it is not possible to identify a velocity gradient across the TMC as suggested by Narayanan et al. (2008).

Comparing the distribution of sources identified in the *Gaia* database in Figures 4.11 and 4.8 along with their respective velocity scales supports the conclusions made by Narayanan et al. (2008) and Soma et al. (2018) with regards to the bulk velocity of the surrounding gas in the TMC region. Although the scaling factors presented here are quite coarse, the results of this study support a V_{LSR} figure of ≈6 kms^{-1} for the bulk motion of the Taurus complex.

In their separate studies comparing stellar radial velocities and the velocity

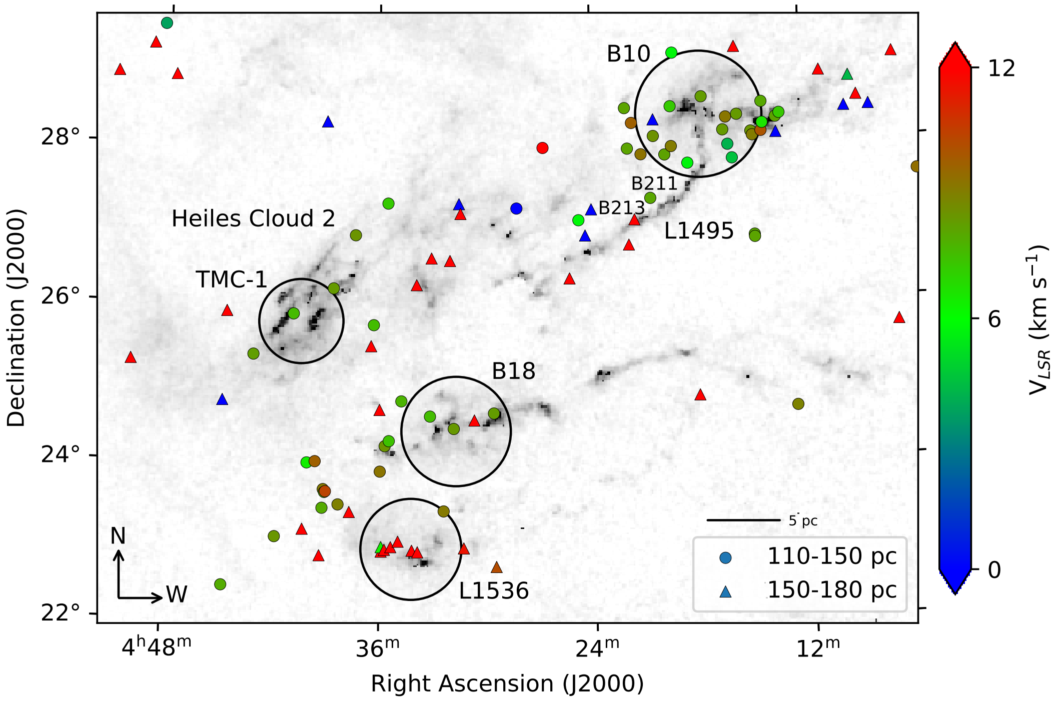

Figure 4.11 V_{LSR} of sources. There is no clear indication of a velocity gradient across the cloud structure. High velocity sources can be identified in the upper central region of the map (see text).

of the underlying molecular gas, Qian, Li, and Goldsmith (2012) and Galli et al. (2019) note that the gas and stars associated with the TMC are closely coupled. Our findings, presented in Figure 4.11 are consistent with this even though we have not calculated the numerical differences between the mean gas and stellar velocities.

4.4.2 Spectral classification and types

The low-mass stellar and sub-stellar populations of the TMC have been the subject of numerous studies (e.g. Rebull et al., 2010; Takita et al., 2010; Luhman et al., 2009b). Studies of early-type high-mass stars in the region are less numerous and it is generally accepted that the region is lacking in young stars of intermediate and high mass (e.g. Whittet et al., 2004; Mooley et al., 2013), and the findings of Rebull et al. (2010).

To investigate the demographics of our population, our 142 sources were cross-matched to the SIMBAD database to obtain spectral information. In SIMBAD the object type is based on the hierarchical system proposed by Ochsenbein and Dubois (1992), however there is some overlap between classifications. Figure 4.12 presents the distribution of spectral classes throughout the region under study. The sources are presented using a key adapted, and simplified, from Ducourant et al. (2005).

Not shown on Figure 4.12 are sources in our study that are not found in the SIMBAD database (52 sources) and those that are designated as ‘Star’

(18 sources), Brown Dwarfs (3 sources) and those that are identified as double or multiple systems (2 sources). Sources in our study that SIMBAD simply identifies as 'YSO' or 'PMS' are shown in Figure 4.12 as 'PMS' sources. Those identified as Intermediate Mass PMS stars, in the range $2 \leq M_\odot \leq 8$, include Herbig Ae/Be sources, emission-line stars and those that SIMBAD records as being variable. The sources shown as Low Mass PMS sources ($<2M_\odot$) include T Tauri stars (both CTT and WTT) and their candidates as well as active X-ray sources.

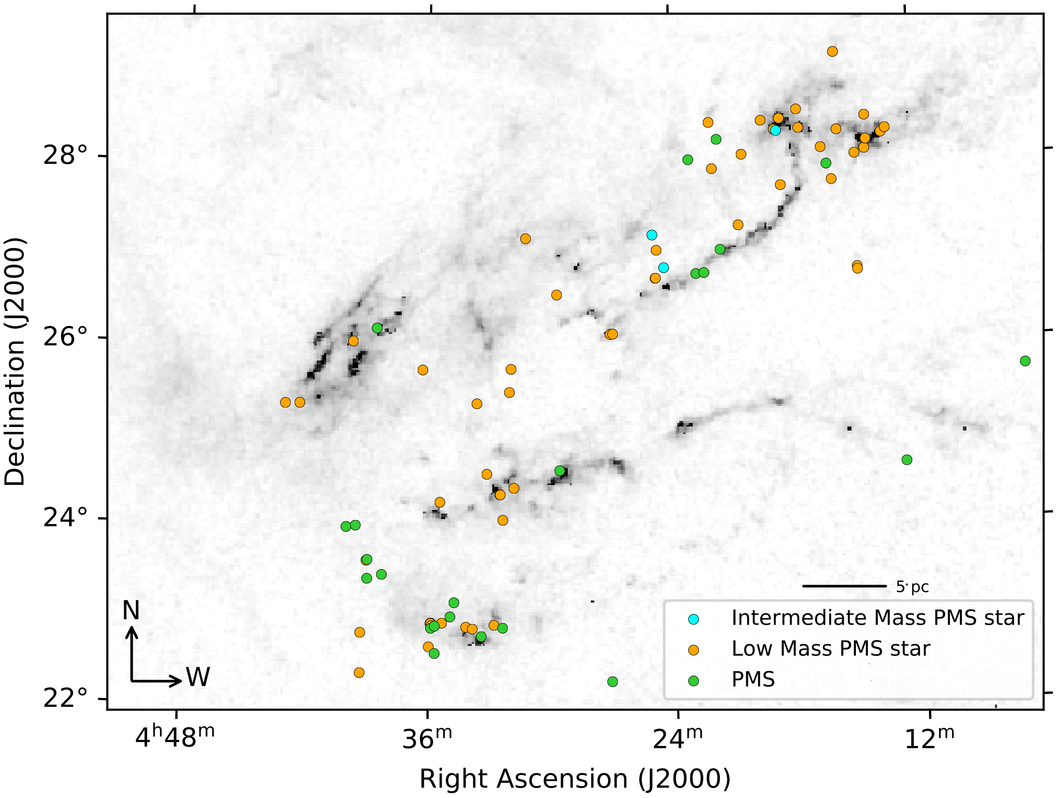

Figure 4.12 SIMBAD spectral classifications for our cohort of 142 *Gaia* sources, including candidate types (See text for legend description).

As to be expected in such a study, the areas discussed here, namely B10, B18, L1536 and TMC-1 show concentrations of young stellar objects. Notable exceptions to this are (1) Gaia DR2 152226491513195648, an Mo:Ve Variable (Orion Type) star (Herbig, Vrba, and Rydgren, 1986; Kazarovets et al., 2017) also classified as a Herbig Ae/Be star (Herbst and Shevchenko, 1999), (2) the M3 Variable star [XCR2012] TrES J042423+265008 (Gaia DR2 152109054223716480) described by Kraus et al. (2017), and (3) the M7 Brown Dwarfs [BLH2002] KPNO-Tau 5 and 2MASS J04350850+2311398, (Luhman et al., 2009b) and IRAS S04414+2506 (Luhman et al., 2006) recorded in the *Gaia* DR2 data as Gaia DR2 151327159721125888, Gaia DR2 145238687096970496 and Gaia DR2 147441558642852736 respectively.

Figure 4.13 shows that the distribution of YSOs in the form of K and M-type stars follows the major structure and filaments of the cloud and is consistent with previous studies of the area. The G-type (G2e) star in L1536 is Gaia DR2 145213192171159552 (CoKu HP Tau G2) (Xu et al., 2019; Rizzuto et al., 2020) which is a member of the multiple HP Tau group along with HP Tau and HP Tau G3 (König, Neuhäuser, and Stelzer, 2001).

The A-type star, V* V892 Tau (Gaia DR2 164513602672978304) is one of the few Herbig Ae/Be stars in the Taurus system, the others being AB Aur an A0Ve star (Mooley et al., 2013) and MWC 480 classed as A5Vep (Mora et al., 2001). Classified in SIMBAD as an A0Ve irregular variable (Skiff, 2010), V* V892 Tau illuminates an optical nebula and has been previously classified B8V (Hernández et al., 2004). The spectral energy distribution (SED) of V892 suggests that it is either a young embedded Class I object surrounded by a developing envelope or a more evolved Class II source seen through an edge-on disk. Mid-IR imaging of the V892 Tau system (Monnier et al., 2008) have confirmed the existence of a circumbinary disk and a binary companion. Mooley et al. (2013) confirm V* V892 Tau as a proper-motion member of the Taurus group.

4.4.3 Age determination of PMS study groups

Determining the ages of PMS and Young stars is highly problematic. One of the most useful tools for investigating the age of stellar populations is the colour-magnitude diagram (CMD) used in conjunction with model isochrones derived from an observational photometric system.

The use of theoretical stellar evolutionary sequences, or isochrones, is one of the few methods used in determining stellar ages on a large scale. There are many different models that can be used in their generation e.g. Yale-Potsdam Stellar Isochrones (YaPSI) (Spada et al., 2017), Padova stellar evolutionary tracks and isochrones (e.g. Bressan et al., 1993), BaSTI (a Bag of Stellar Tracks and Isochrones (Pietrinferni et al., 2013), and Modules for Experiments in Stellar Astrophysics (MESA) (Paxton et al., 2010). The choice of which model to use is largely dependant on the input data available and the desired outcome.

From the many models available, the PARSEC (PAdova and TRieste Stellar Evolution Code) model developed by Bressan et al. (2012) was chosen to produce isochrones to describe the age relationship between our sources. This model was chosen because it is currently one of the few available that can produce an output related to the *Gaia* DR2 G-Band photometric system.

Access to the PARSEC model is via the online 'CMD 3.3 input form'[2] maintained by Léo Girardi at the Osservatorio Astronomico di Padova. Users are required to define parameters related to their needs, i.e. what form of evolutionary track is required?, what photometric system is to be used?, what value of

[2] http://stev.oapd.inaf.it/cgi-bin/cmd

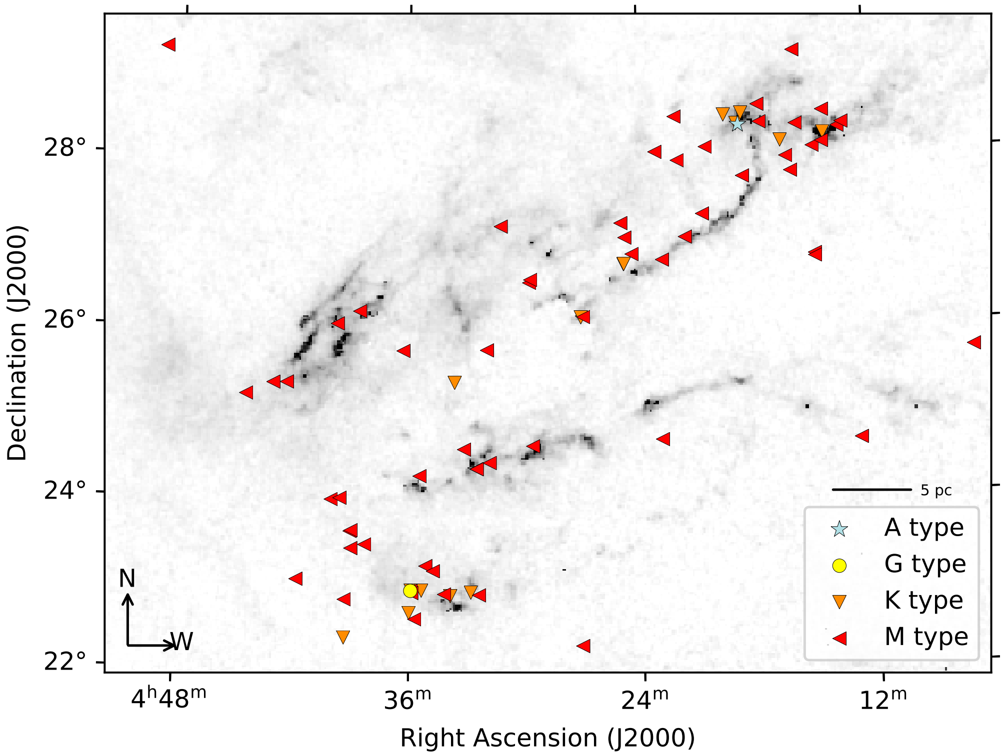

(a)

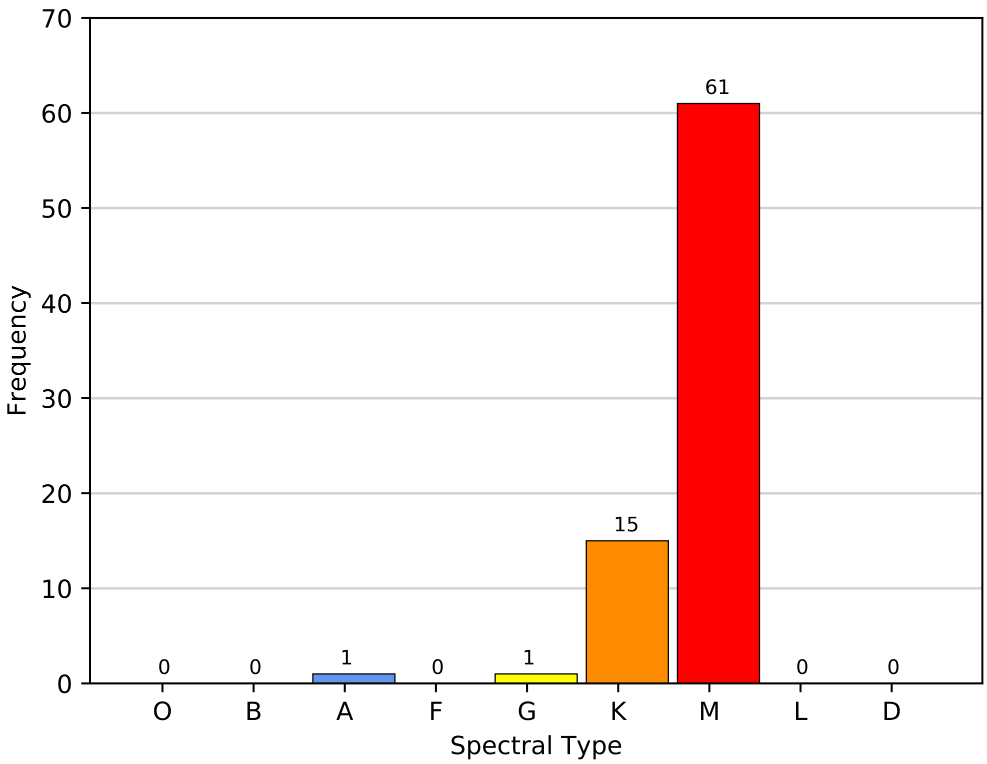

(b)

Figure 4.13 Only 78 (55%) of our 142 sources have SIMBAD determinations of spectral type, seen here as (a) a spatial distribution, and (b) as a histogram.

interstellar extinction is to be used? etc. Output from the system can be selected from a number of different options.

In defining our isochrones, the *Gaia* DR2 photometric system using Vega magnitudes as defined in Weiler (2018) was selected. A uniform metallicity fraction for our sources of Z = 0.02 was assumed, that being the value for solar mass (i.e. low-mass) pre-main sequence stars (e.g. Forestini, 1994; Tout, Livio, and Bonnell, 1999; Di Criscienzo, Ventura, and D'Antona, 2009) in the range 0.1 to 2.0 $M_{\odot}$, and in-line with the value of Z = 0.0189 for solar models at the beginning of the PMS stage (Anders and Grevesse, 1989). An interstellar extinction value (Av) of 0.85 mag kpc^{-1} (Gontcharov, 2016) was chosen with a Kroupa interstellar medium (Kroupa, 2001; Kroupa, 2002). A full list of our input parameters is given in Table 4.2.

Input Parameter	Solution
Evolutionary tracks	PARSEC version 1.2S.
Photometric system	Using *Gaia*'s DR2 G, G_{BP}, and G_{RP} (Vegamags, *Gaia* passbands from Weiler (2018)).
Bolometric system	OBC bolometric corrections are selected to convert the isochrones to photometric brightness in the *Gaia* optical passbands, see Girardi et al. (2008).
Circumstellar dust	For M stars: with fixed optical data sets from Nanni et al. (2013) & Nanni et al. (2014). For C stars: No dust.
Interstellar extinction	Av = 0.85 mag with constant extinction coefficients using Rv = 3.1 from Cardelli, Clayton, and Mathis (1989) and O'Donnell (1994).
Initial mass function	Canonical two-part-power law IMF, corrected for unresolved binaries (Kroupa, 2001) & (Kroupa, 2002).
Age / Metallicities	Linear age: initial & final values 0.5e6 yr to 30e6 yr in single steps. Metallicities: using metal fraction Z = 0.02 initial & final values with 0.0 step.
Output	Isochrone tables

Table 4.2 Input parameters used in defining the isochrones at 0.5; 1.0; 5.0; 10.0; 20.0 and 30.0 Myr used in our study.

Figure 4.14 shows the CMD and isochrones for our 'near' and 'far' groups. The plot shows the combined groups from both of our studies in order to produce a concise overview of our 'near' and 'far' distributions.

The grey dots show the distribution of 1245 foreground and background stars obtained using our filtered query (see Figure 3.8) that lie within the same 100 pc region covered by our studies, they are considered to be main-sequence stars here. The 'near' and 'far' groups shown are a combination

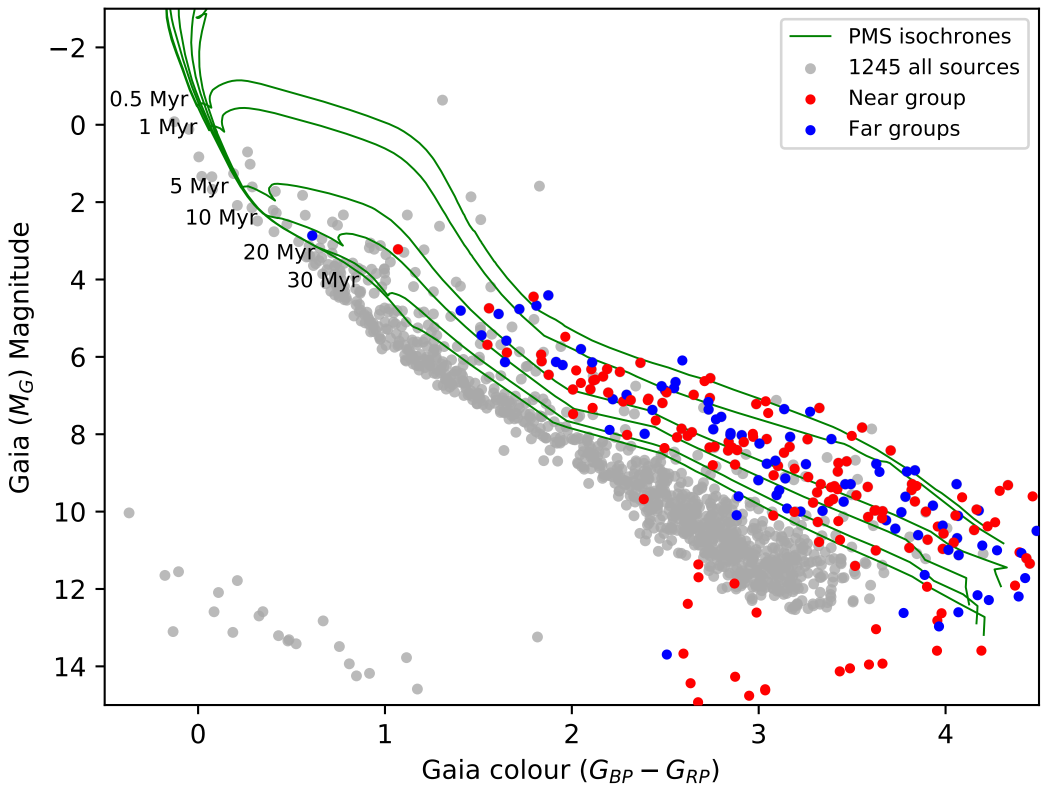

Figure 4.14 Age relationships of our combined 'near' and 'far' groups. The grey dots show the distribution of 1245 foreground and background stars (see text). The 'near' and 'far' populations shown represent the combined groups from our studies detailed in Chapter 3 and Chapter 4. The isochrones are spaced in intervals detailed in the text.

from the studies presented in both Chapter 3 and Chapter 4 and constitute 89 sources from our preliminary study, 70 sources from the final group of 142 identified in Section 4.3.1 and 72 sources which are common to both studies - a total of 231 sources. Our distributions are plotted against isochrones representing ages of 0.5; 1.0; 5.0; 10.0; 20.0 and 30.0 Myr. Within this range of ages, very young stars, associated with star-forming regions, are considered to be less than 5 Myr old whilst solar mass, young PMS stars are less than 30 Myr old (Soderblom et al., 2014).

From Figure 4.14 it is not easy to differentiate between the ages of our 'near' and 'far' populations. It is however possible to see that the vast majority of sources lie within the boundaries identified by Soderblom et al. (2014). At magnitudes <11 mag it can be seen that a large scattering of sources lie below and to the left of the main sequence. Whilst this may be a true representation of their position on the CMD, the scattering is more likely due to an accumulation of errors caused by errors on the measurement of the photometric magnitude and the increase in these errors due to the colour subtraction effect of G_{BP}-G_{RP}. For the purposes of further discussion these sources are ignored.

In their consideration of YSO's in the Gould Belt, of which the TMC is a member, Dunham et al. (2015) present limits on the lifetime durations of the various classes of YSO. Taking contamination of Class III YSO's by background AGB stars and IR excess into account they determine YSO lifetimes as presented in Table 4.3.

YSO Class	Stage	Duration (Myr)	$\simeq$ Max Age (Myr)
0 + I	Protostellar	0.5 to 0.7	0.7
Flat spectrum		0.3 to 0.5	1.2
II + III	T Tauri to PMS	3.0	4.2

Table 4.3 Lifetime duration of YSO's, with inferred ages, taken from Dunham et al. (2015).

To investigate our 'near' and 'far' populations more fully, isolated individual groups in our study area have been identified (see Figure 3.12). Two groups from each of the 'near' and 'far' populations have been selected, in different regions, as a representative sample. From the 'near' population region B7 (lying in the Eastern region of B10 in Figure 3.12) and the collection of sources in the Eastern part of B18 have been chosen, denoted here as B18e. From the 'far' population regions L1536 and B213 are used.

The results of our investigation are presented in Figure 4.15. In each case, members of the various complexes have ages between 1 Myr to 5 Myr which is consistent with the findings of Dunham et al. (2015).

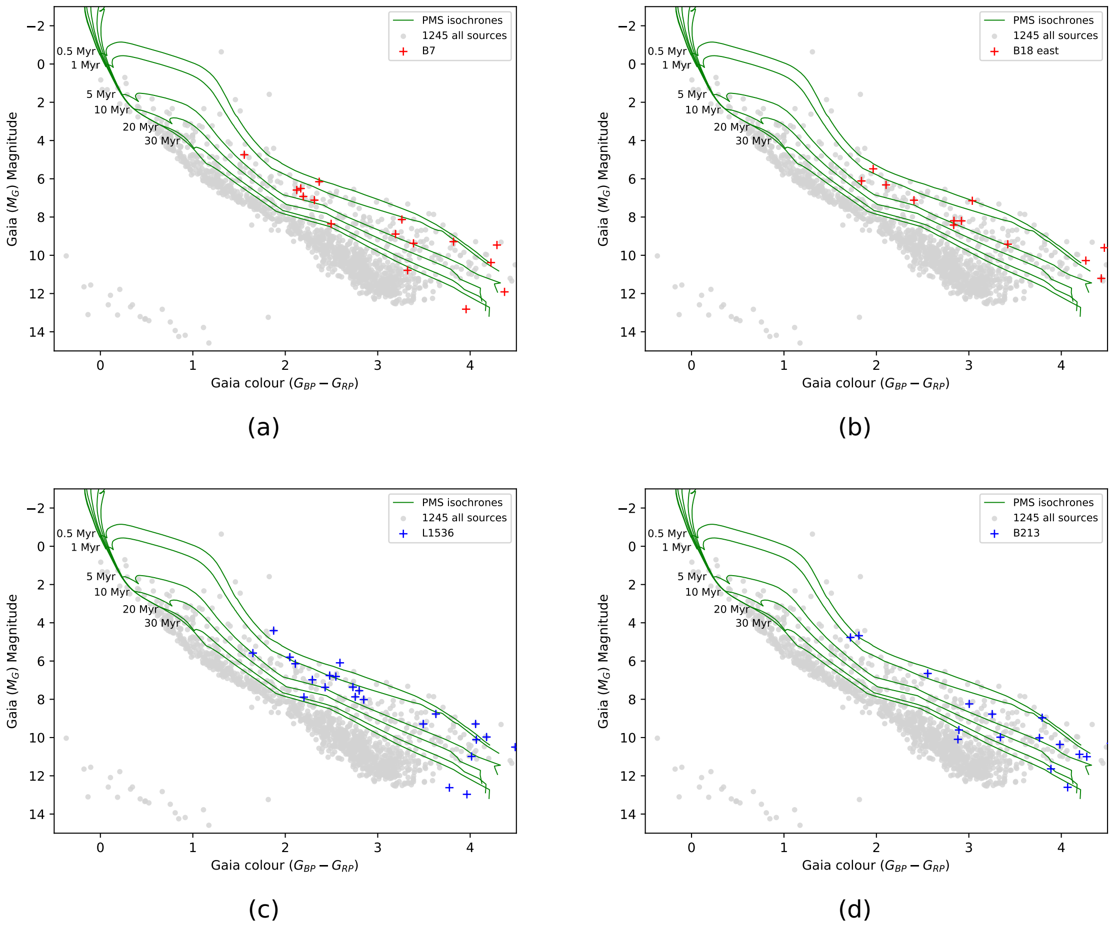

Figure 4.15 Distribution of ages for discrete regions of the TMC. 'Near' groups are coloured red and 'far' groups are shown in blue. The populations shown are an amalgamation of sources identified in both studies presented in this research. (a) Region B7. (b) Region B18e. (c) L1536. (d) Region B213

4.4.4 Determining population peer groups

Literature studies (see Appendix F.1.1) suggest that young Class II (CTTS) sources with optically thick disks are best observed in the infrared whilst more evolved Class III (WTTS) sources become visible at optical wavelengths due to their optically thin disks. It is therefore possible to draw an analogy between these classifications and the studies presented here. It seems reasonable to suggest that our preliminary (*Spitzer* sampled) investigation studied the 'younger' infrared population whilst our follow-on study using *Gaia* optical data looked at a more 'evolved' population of sources, sources appearing in both studies representing an adolescent group between them.

Following this possible link between evolved stages and the studies presented here, Figure 4.16 presents a three-dimensional grid showing the results from both studies.

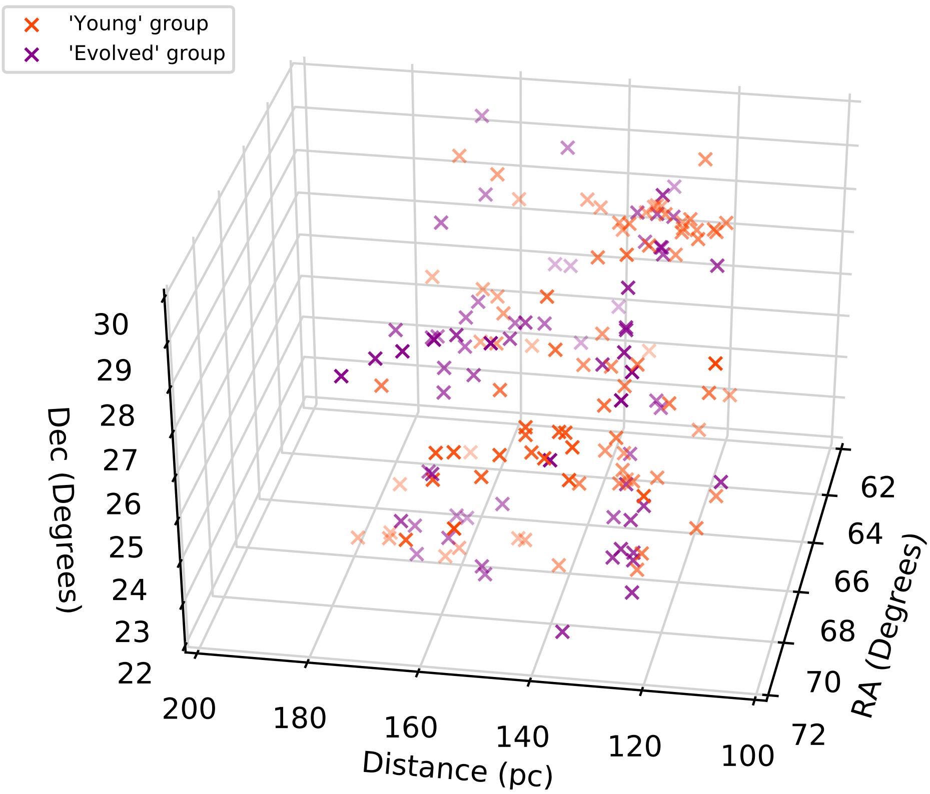

Figure 4.16 Spatial distribution of sources identified in our preliminary and follow-on studies. Sources are identified here according to our inferred 'developmental' groups (see text).

Figure 4.16 provides a graphical representation of the results presented in the studies discussed in Chapter 3 and Chapter 4. The preliminary study sources are identified as 'young' and the follow-on study sources identified as 'evolved'. Those sources which appear in both studies and are considered to be at an intermediate age are omitted for the purposes of clarity. Whilst the distinction between the 'near' and 'far' groups from both studies is still clearly apparent there appears to be no clear demarcation between age ranges presented, suggesting that the link discussed above may simply be fortuitous.

5 DISCUSSION

The intention in planning this study was to use the *Gaia* telescope's newly available second data release to investigate the Taurus Molecular Cloud and to compare its findings with those of previous studies.

In defining this study for approval, the following statement was made:

> *Transverse velocities and proper motions will be identified as the kinematic properties of objects within the various clouds and structures of the TMC, to show the relative motions of these regions within the larger cloud structure. The relative depths of objects within the TMC will be identified and, through the use of 3-D graphical representations, making use of the unprecedented accuracy of the Gaia parallax measurements, it is hoped to better constrain the boundaries of the Taurus molecular cloud.* (Fleming 2019, Research Project Approval).

Here some of the findings from our investigative studies are draw together.

5.1 Combined Study Results

An area of the Taurus Molecular Cloud of approximately 375 pc^2 with a depth of 100 pc has been studied using G-band *Gaia* DR2 astrometry available on the open access *Gaia* Archive portal.

By cross-matching *Gaia* DR2 with *Spitzer* infrared data a group of 161 young YSO's have been investigated. The existence of two, previously unrecognised, distributions have been identified within the TMC, centred on 147.9 pc. Statistical analysis has confirmed the existence of these two populations with a 'near' group centred at 131$\pm$7 pc and a 'far' group at 160$\pm$5 pc to 1σ. Additionally, these groups are found to have different proper motions and markedly different solar corrected velocity vectors. The findings from this preliminary study were placed in the on-line open-access archive (arXiv) and submitted for peer-review in the scientific press.

By applying quality filters to the initial query a potentially more evolved group of 142 pre-main sequence stars have been identified using *Gaia* optical data only. An investigation of these sources reaffirms the existence of two populations, this time centred on 139.7 pc which is entirely consistent with the literature. This second study found the two groups at slightly different distances from the preliminary study, this time centred at 130.0$\pm$3 and 160$\pm$12 pc, again at 1σ for the 'near' and 'far' groups respectively. The greater variability in the 'far' groups value reflecting the larger physical scattering of its members. As with the previous study, proper motion and velocity vector studies highlighted the individuality of the two groups.

5.2 Conclusions & Future Proposals

In conclusion, this investigation has:

- In conjunction with the use of *Spitzer* data, *Gaia* DR2 has been able to isolate two previously unidentified populations of YSO at different distances.
- The existence of these distinct populations has been confirmed though the sole use of *Gaia* data for a more evolved group of YSO's and Young stars.
- In both studies the 'near' and 'far' populations have been found to have different proper motions, suggesting the possibility that they have different origins (convergent points).
- The dating of discrete regions from both 'near' and 'far' populations has shown them to have contemporary ages and confirms the populations as being YSO's and Young stars.

The identification of two discrete populations of YSO's, the presentation of Figure 4.16 as a 3-dimensional graphical representation of the Taurus molecular cloud and the wider results discussed have met the objectives set for this study. This investigation has shown the *Gaia* data to be versatile in analysing the kinematics of stellar and pre-stellar populations.

During these studies I have contributed to a new understanding of the kinematics of the Taurus star-forming region using the second data release of the *Gaia* space telescope. These findings have led me to submit a paper to a peer reviewed journal, and I have presented at International conferences.

The area known as the Gould Belt is an area consisting of an 'elliptical ring' of young stars and clouds of neutral hydrogen located within the Milky Way Galaxy with semi-major and semi-minor axes of 375 pc and 235 pc respectively. The centre of the structure is located about 105 pc from the Sun in the direction of the Galactic anti-centre and is tilted with regards to the plane of the Milky Way. The Gould Belt is a dynamic region, containing several million solar masses of interstellar material which includes all the nearby sites of active star formation (Taurus, Orion, Ophiuchus, Perseus etc.) and has been the subject of recent radio surveys (e.g. Gonthier, 2005; Loinard, 2012; Ortiz-León et al., 2017). The precise formation history of the structure is still the subject of study with a number of competing theories being proposed.

With the release of *Gaia*'s third data release (DR3) in its early-release form in the Autumn/Winter of 2020 and the full release in the middle of 2021 it will be possible to explore the Gould Belt in detail.

Using the techniques used in this study, and the newly available *Gaia* DR3 data, it will be possible to create dynamic simulations of the Gould Belt with a view to understandings its structure, kinematics and relationship to its local environment. It is expected that such studies would provide new insights into the origins, coherence and current nature of this region.

A *gaiadr2.gaia_source* Column Descriptors

This table has been compiled using information sourced from the *Gaia* Archive documentation[1], where a complete description of each field can be found.

Table A.1 *Gaia* Data Descriptors

Data ID	Description
solution_id	An unequivocal DPAC solution identifier
designation	Unique designation across all *Gaia* Data Releases
source_id	A unique numerical identifier of the source
random_index	Random index to select smaller subsets of data
ref_epoch	Epoch of the source parameters [Julian Years]
ra	Barycentric ra of the source in ICRS at ref_epoch [deg]
ra_error	Standard error of ra [mas]
dec	Barycentric dec of the source in ICRS at ref_epoch [deg]
dec_error	Standard error of dec [deg]
parallax	Absolute stellar parallax of the source at ref_epoch [mas]
parallax_error	Standard error of parallax [mas]
parallax_over_error	Parallax divided by its standard error
pmra	Proper motion in ra [mas/year]
pmra_error	Standard error of pm in ra direction [mas/year]
pmdec	Proper motion in declination direction [mas/year]
pmdec_error	Standard error of pm in dec direction [mas/year]
ra_dec_corr	Correlation between ra and dec
ra_parallax_corr	Correlation between ra and parallax
ra_pmra_corr	Correlation between ra and pm in ra
ra_pmdec_corr	Correlation between ra and pm in dec
dec_parallax_corr	Correlation between dec and parallax
dec_pmra_corr	Correlation between dec and pm in ra
dec_pmdec_corr	Correlation between dec and pm in dec
parallax_pmra_corr	Correlation between parallax and pm in ra
parallax_pmdec_corr	Correlation between parallax and pm in dec
pmra_pmdec_corr	Correlation between pm in ra and pm in dec
astrometric_n_obs_al	Total number of AL observations
astrometric_n_obs_ac	Total number of AC observations
astrometric_n_good_obs_al	Number of good AL observations
astrometric_n_bad_obs_al	Number of bad AL observations
astrometric_gof_al	Goodness-of-fit statistic of the astrometric solution
astrometric_chi2_al	AL chi-square value
astrometric_excess_noise	Excess noise of the source [mas]
astrometric_excess_noise_sig	Significance of excess noise
astrometric_params_solved	Binary code indicating which parameters were estimated
astrometric_primary_flag	Was this source a primary or secondary source
astrometric_weight_al	Mean astrometric weight of the source [mas^{-2}]
astrometric_pseudo_colour	Astrometrically determined pseudocolour [μm^{-1}]
astrometric_pseudo_colour_error	Standard error of the pseudocolour [μm^{-1}]
mean_varpi_factor_al	Mean parallax factor in the AL direction
astrometric_matched_observations	The number of FOV transits matched to this source

Continued on next page

[1] https://gea.esac.esa.int/archive/documentation/GDR2/Gaia_archive/chap_datamodel/sec_dm_main_tables/ssec_dm_gaia_source.html

Table A.1 – continued from previous page

Data ID	Description
visibility_periods_used	Number of visibility periods used in the astrometric solution
astrometric_sigma5d_max	The longest semi-major axis of the 5-d error ellipsoid [mas]
frame_rotator_object_type	The type of the source mainly used for frame rotation
matched_observations	Amount of observations matched to this source
duplicated_source	Source with duplicate sources
phot_g_n_obs	Number of observations contributing to G photometry
phot_g_mean_flux	G-band mean flux
phot_g_mean_flux_error	Error on G-band mean flux
phot_g_mean_flux_over_error	G-band mean flux divided by its error
phot_g_mean_mag	G-band mean magnitude
phot_bp_n_obs	Number of observations contributing to BP photometry
phot_bp_mean_flux	Integrated BP mean flux
phot_bp_mean_flux_error	Error on the integrated BP mean flux
phot_bp_mean_flux_over_error	Integrated BP mean flux divided by its error
phot_bp_mean_mag	Integrated BP mean magnitude
phot_rp_n_obs	Number of observations contributing to RP photometry
phot_rp_mean_flux	Integrated RP mean flux
phot_rp_mean_flux_error	Error on the integrated RP mean flux
phot_rp_mean_flux_over_error	Integrated RP mean flux divided by its error
phot_rp_mean_mag	Mean magnitude in the integrated RP band
phot_bp_rp_excess_factor	BP/RP excess factor with respect to the G-Band flux
phot_proc_mode	Indicates different calibration procedures in place
bp_rp	BP $-$ RP colour
bp_g	BP $-$ G colour
g_rp	G $-$ RP colour
radial_velocity	Spectroscopic rv in the solar barycentric reference frame
radial_velocity_error	Error accounting for the calibration contribution
rv_nb_transits	Number of transits (epochs) used to compute rv
rv_template_teff	T_{eff} of the synthetic spectrum template used to determine rv
rv_template_logg	log*g* of the synthetic spectrum template used to determine rv
rv_template_fe_h	Fe/H of synthetic spectrum template used to determine rv
phot_variable_flag	Indicates if variability identified in the photometric data
l	Galactic Longitude of the object at reference epoch [deg]
b	Galactic Latitude of the object at reference epoch [deg]
ecl_lon	Ecliptic Longitude of the object at reference epoch [deg]
ecl_lat	Ecliptic Latitude of the object at reference epoch [deg]
priam_flags	Flags for the Apsis-Priam results
teff_val	Estimate of Teff from Apsis-Priam [K]
teff_percentile_lower	Lower 16th percentile uncertainty on T_{eff} estimate
teff_percentile_upper	Upper 84th percentile uncertainty on T_{eff} estimate
a_g_val	Estimate of extinction in the G band (Magnitude[mag])
a_g_percentile_lower	Lower 16th percentile uncertainty on AGG estimate
a_g_percentile_upper	Upper 84th percentile uncertainty on AGG estimate
e_bp_min_rp_val	Estimate of reddening E(BP-RP) [mag]
e_bp_min_rp_percentile_lower	Lower 16th percentile uncertainty on E(BP-RP) estimate
e_bp_min_rp_percentile_upper	Upper 84th percentile uncertainty on E(BP-RP) estimate
flame_flags	Status of the astrophysical parameters radius and luminosity
radius_val	Estimate of radius from Apsis-FLAME [Solar Radius]
radius_percentile_lower	Lower 16th percentile uncertainty on radius estimate
radius_percentile_upper	Upper 84th percentile uncertainty on radius estimate
lum_val	Estimate of luminosity [Solar Luminosity]
lum_percentile_lower	Lower 16th percentile uncertainty on luminosity estimate
lum_percentile_upper	Upper 84th percentile uncertainty on luminosity estimate

B *Gaia* Archive queries

This appendix contains the ADQL queries used to interrogate the *Gaia* DR2 Archive. An explanation of the line descriptors are given in Table B.1 following the query listings.

```
SELECT *
FROM gaiadr2.gaia_source
WHERE parallax BETWEEN 5.0 AND 10.0
    AND CONTAINS (POINT(’ICRS’, ra, dec), BOX(’ICRS’, 68.5, 27.0, 15.0,
     10.0)) = 1
    AND parallax_over_error > 5.0
    AND phot_bp_mean_flux_over_error > 10
    AND phot_rp_mean_flux_over_error > 1
    AND astrometric_n_good_obs_al > 5
    AND (SQRT(astrometric_chi2_al/
    (astrometric_n_good_obs_al - 5.0)) < 1.2
    OR SQRT(astrometric_chi2_al/(astrometric_n_good_obs
    _al - 5.0)) < 1.2*exp(-0.2*(phot_g_mean_mag - 19.5)))
    AND phot_bp_rp_excess_factor BETWEEN 1.0 + (0.03*POWER
    (phot_bp_mean_mag - phot_rp_mean_mag, 2.0))
    AND 1.3 + (0.06*POWER(phot_bp_mean_
    mag - phot_rp_mean_mag, 2.0))
    ORDER BY parallax DESC
```

Listing B.1 Original ADQL query (4770 sources returned)

```
SELECT *
FROM gaiadr2.gaia_source
WHERE parallax BETWEEN 5.0 AND 10.0
    AND CONTAINS (POINT(’ICRS’, ra, dec),
    BOX(’ICRS’, 68.5, 27.0, 15.0, 10.0)) = 1
    AND parallax_over_error > 5.0
    AND astrometric_n_good_obs_al > 5
    ORDER BY parallax DESC
```

Listing B.2 Final query (returned 7587 sources)

Table B.1 lists the line numbers and descriptors used in the original *Gaia* Archive query presented in Listing B.1. Listing B.2 removes the quality constraints whilst retaining the essential elements of the orignal query. Descriptors for the code in Listing B.2 will also be found in this table (but with different line numbers).

Table B.1 *Gaia* Query Descriptors

Line No.	Descriptor
2	Identifies the data source file.
3	Get data between 100pc (parallax 10.0) and 200pc (parallax 5.0).
4	Identifies the search 'box' by centre coordinates and widths of sides.
5	Setting relative precision on parallax at 5% (actually better than 20%).
6	Setting Gbp flux error signal-to-noise greater than 10.
7	Setting Grp flux error signal-to-noise greater than 10 .
8	There must be at least 5 independent astrometric measurements for a reliable selection.
9-12	Filtering on how well the 5 parameter model fits the astrometry. and will tend to exclude binaries.
13-16	This excludes any measurements where crowding has seriously affected the photometry.
17	order the output data table by descending parallax values (i.e. increasing distance).

C Catalogue of Preliminary Sources

Here we list the parameters of the 168 sources, from the *Spitzer* catalogue, used in our preliminary study (Chapter 3).

Sources which have been removed at various stages in the study have been color coded so that the reader may judge the validity of the decisions made. Within the table, the following colour code has been used to highlight groups discussed in the text.

- 3 sources identified in Figure 3.4b as being outside the main populations.
- 4 sources rejected as lying outside 12-40 mas yr^{-1} proper motion limits.
- 5 sources within 12-40 mas yr^{-1} proper motion limits but lying outside the boundary of Figure 3.9b.

Table C.1 Catalogue of 168 *Gaia*/*Spitzer* Sources

Gaia DR2 ID	SSTtau ID	RA [deg]	Dec [deg]	Parallax [mas]	Distance [pc]	PMRA [mas yr^{-1}]	PMDec [mas yr^{-1}]	μ [mas yr^{-1}]
147869573608324992	043051.7+24414	67.7156	24.6965	9.51	105.12	11.52	-24.50	27.10
151870352825256576	043545.2+273713	68.9387	27.6202	8.83	113.19	14.20	-25.79	29.44
147778490237623808	043306.6+240954	68.2777	24.1652	8.83	113.20	9.56	-20.23	22.37
149685627517927296	042359.7+251452	65.9988	25.2479	8.75	114.33	0.99	-19.70	19.72
147546080967742720	043621.5+235116	69.0896	23.8545	8.66	115.46	-1.54	-19.48	19.54
151296579553731456	043007.2+260820	67.5302	26.1390	8.62	116.06	2.67	-21.927	22.09
164513602672978304	041840.6+281915	64.6692	28.3209	8.52	117.44	6.62	-29.87	30.60
164513022853468160	041807.9+282603	64.5333	28.4342	8.48	117.95	8.43	-24.73	26.13
149409920679460096	042630.5+244355	66.6273	24.7321	8.41	118.91	2.74	-22.02	22.19
164502062096975744	041901.1+281942	64.7546	28.3282	8.38	119.37	8.71	-25.34	26.79
164598303725243776	041935.4+282721	64.8978	28.4560	8.36	119.64	11.93	-25.97	28.58
164550882989640192	042203.1+282538	65.5132	28.4274	8.31	120.27	10.27	-25.86	27.83
146874275068113664	044000.6+235821	70.0028	23.9724	8.30	120.49	8.62	-20.74	22.46
151262700852297728	042704.6+260616	66.7696	26.1044	8.25	121.18	6.16	-19.30	20.26
164546038266077824	042025.8+281923	65.1077	28.3232	8.19	122.13	10.66	-24.22	26.46
151102790629500288	043057.1+255639	67.7384	25.9442	8.14	122.82	5.42	-23.02	23.65
148116246465275520	044205.4+252256	70.5229	25.3822	8.14	122.88	5.49	-18.99	19.77
164507353496637952	041831.1+281629	64.6297	28.2747	8.12	123.08	8.82	-25.64	27.12
165563674934601856	041357.3+291819	63.4891	29.3053	8.10	123.47	9.95	-22.89	24.96
146764465639042176	043906.3+233417	69.7766	23.5716	8.06	124.14	8.18	-21.82	23.30
147799209159857280	043217.8+242214	68.0745	24.3707	8.05	124.17	6.26	-22.20	23.06
164519276325850752	041817.1+282841	64.5713	28.4782	8.04	124.37	5.79	-25.03	25.69
146675954953119104	043815.6+230227	69.5651	23.0409	7.98	125.24	-1.07	-17.19	17.22
164513400810646912	041842.5+281849	64.6771	28.3138	7.97	125.50	12.13	-24.15	27.02

Continued on next page

Table C.1 – continued from previous page

Gaia DR2 ID	SSTtau ID	RA [deg]	Dec [deg]	Parallax [mas]	Distance [pc]	PMRA [mas yr^{-1}]	PMDec [mas yr^{-1}]	μ [mas yr^{-1}]
164495323291866624	041851.1+281433	64.7132	28.2425	7.96	125.66	8.61	-24.65	26.11
164513538249595136	041847.0+282007	64.6960	28.3353	7.95	125.77	8.30	-25.31	26.63
164422961683000320	041941.2+274948	64.9220	27.8299	7.91	126.37	9.94	-24.96	26.87
152118881108855680	042445.0+270144	66.1878	27.0290	7.89	126.73	8.39	-26.84	28.13
146767764173923328	043858.5+233635	69.7442	23.6097	7.89	126.82	8.64	-21.20	22.89
163165738856771200	041514.7+280009	63.8114	28.0025	7.88	126.88	8.55	-25.52	26.92
146881048231272192	043933.6+235921	69.8902	23.9891	7.87	127.12	7.28	-20.99	22.22
152511475478780416	042155.6+275506	65.4819	27.9183	7.85	127.37	10.75	-27.22	29.27
151793082068521856	043114.4+271017	67.8102	27.1715	7.84	127.49	9.17	-27.58	29.06
164445437248152832	042026.0+280408	65.1087	28.0691	7.84	127.51	8.33	-26.07	27.37
146764809236423808	043901.6+233602	69.7568	23.6007	7.82	127.81	8.57	-21.85	23.47
162758236656524416	041447.8+264811	63.6995	26.8030	7.82	127.93	9.02	-22.45	24.20
148037764527442944	043619.0+254258	69.0796	25.7163	7.81	128.02	8.91	-27.47	28.88
163184366130809984	041412.9+281212	63.5539	28.2033	7.80	128.13	8.93	-29.05	30.40
147606657186323712	043527.3+241458	68.8641	24.2496	7.80	128.22	6.05	-20.77	21.64
151327159721125888	042945.6+263046	67.4403	26.5128	7.80	128.23	6.87	-20.97	22.06
147801339463632000	043301.9+242100	68.2582	24.3499	7.80	128.24	6.37	-20.47	21.44
162757545164429696	041447.3+264626	63.6971	26.7739	7.78	128.47	9.48	-22.69	24.59
163246832135164544	041314.1+281910	63.3090	28.3195	7.76	128.85	8.37	-24.40	25.80
164698634160139264	041733.7+282046	64.3906	28.3462	7.76	128.88	9.18	-25.55	27.15
164702070133970944	041749.6+282936	64.4569	28.4933	7.75	129.03	6.90	-24.62	25.57
151373820245230080	042920.7+263340	67.3363	26.5611	7.74	129.24	7.91	-20.41	21.89
149369139966814976	042936.0+243555	67.4003	24.5987	7.73	129.42	8.57	-20.20	21.94

Continued on next page

Table C.1 – continued from previous page

Gaia DR2 ID	SSTtau ID	RA [deg]	Dec [deg]	Parallax [mas]	Distance [pc]	PMRA [mas yr^{-1}]	PMDec [mas yr^{-1}]	μ [mas yr^{-1}]
164666022471759232	041628.1+280735	64.1171	28.1265	7.70	129.84	6.85	-25.90	26.80
164409359522965120	041830.3+274320	64.6263	27.7223	7.70	129.89	8.73	-26.27	27.68
145238687096970496	043508.5+231139	68.7855	23.1943	7.69	129.96	7.24	-20.98	22.19
147796013704188928	043231.7+242002	68.1324	24.3341	7.69	130.03	7.12	-21.50	22.65
147796013704189440	043230.5+241957	68.1274	24.3325	7.68	130.21	6.65	-21.86	22.85
146277553787186048	043223.2+240301	68.0972	24.0503	7.68	130.24	7.36	-22.43	23.60
164705368668853120	041738.9+283300	64.4123	28.5500	7.68	130.27	6.87	-25.25	26.17
164536250037820160	042158.8+281806	65.4952	28.3017	7.67	130.33	9.01	-26.39	27.88
151028990206478080	043203.2+252807	68.0138	25.4687	7.67	130.39	8.09	-22.81	24.20
146285112929523456	043023.6+235912	67.5986	23.9868	7.67	130.40	4.73	-21.97	22.48
164518589131083136	041831.1+282716	64.6297	28.4544	7.67	130.44	8.68	-25.10	26.56
147806733942555008	043215.4+242859	68.0643	24.4831	7.67	130.46	5.02	-21.38	21.96
147790202612482560	043334.0+242117	68.3919	24.3547	7.66	130.50	5.88	-20.55	21.38
152226491513195648	042457.0+271156	66.2379	27.1989	7.66	130.57	8.36	-26.75	28.02
147831571737487488	043310.0+243343	68.2918	24.5619	7.66	130.60	7.25	-21.23	22.43
163182888662060928	041411.8+281153	63.5496	28.1981	7.63	131.09	9.08	-23.89	25.56
146366442430208640	042959.5+243307	67.4980	24.5520	7.63	131.12	8.18	-21.44	22.95
148017561002336384	043342.9+252647	68.4289	25.4462	7.63	131.14	5.13	-22.77	23.35
164738521519622656	041414.5+282758	63.5609	28.4660	7.62	131.24	9.50	-23.57	25.41
151297958238753664	042951.5+260644	67.4648	26.1124	7.62	131.28	5.95	-21.01	21.84
150393571269837184	041810.7+251957	64.5450	25.3325	7.61	131.36	8.83	-23.34	24.95
164684340508950144	041539.1+281858	63.9132	28.3162	7.61	131.49	9.25	-24.38	26.08
164504467278644096	041926.2+282614	64.8595	28.4372	7.59	131.70	8.36	-25.47	26.81

Continued on next page

Table C.1 – continued from previous page

Gaia DR2 ID	SSTtau ID	RA [deg]	Dec [deg]	Parallax [mas]	Distance [pc]	PMRA [mas yr^{-1}]	PMDec [mas yr^{-1}]	μ [mas yr^{-1}]
163184366130809472	041413.5+281249	63.5566	28.2136	7.58	131.94	8.59	-24.42	25.88
163184091252903936	041417.0+281057	63.5709	28.1826	7.55	132.44	8.28	-24.16	25.54
152917298349085824	042515.5+282927	66.3147	28.4909	7.52	133.06	10.79	-25.05	27.27
152362491654557696	042039.1+271731	65.1633	27.2920	7.51	133.07	10.41	-26.09	28.09
147847072275324416	043150.5+242418	67.9607	24.4048	7.50	133.33	4.46	-22.96	23.39
151262876946558976	042657.3+260628	66.7388	26.1078	7.50	133.36	5.19	-20.71	21.35
151125919028356352	043336.7+260949	68.4033	26.1636	7.50	133.40	8.16	-17.37	19.19
163179521407696384	041505.1+280846	63.7715	28.1460	7.49	133.57	8.46	-24.48	25.90
152516079683687680	042306.0+280119	65.7754	28.0220	7.47	133.88	7.93	-26.68	27.84
148450085683504896	043835.2+261038	69.6471	26.1773	7.46	133.96	4.89	-21.78	22.32
147869784062378624	043051.3+244222	67.7141	24.7061	7.45	134.22	7.05	-20.94	22.10
151265002954775936	042727.9+261205	66.8667	26.2013	7.42	134.69	1.81	-23.45	23.52
164514053645658752	041901.9+282233	64.7583	28.3758	7.40	135.07	9.19	-25.76	27.35
151374198202645376	042942.4+263249	67.4270	26.5469	7.40	135.12	6.90	-21.21	22.30
162967384383246336	041557.9+274617	63.9917	27.7714	7.37	135.67	7.82	-24.65	25.86
163181342473839744	041417.6+28060	63.5734	28.1026	7.37	135.69	8.34	-23.32	24.76
148172179824515968	044148.2+253430	70.4511	25.5751	7.34	136.16	4.51	-19.61	20.12
148112913570653568	044221.0+252034	70.5876	25.3428	7.34	136.16	4.89	-19.42	20.03
163233981593016064	041327.2+281624	63.3635	28.2734	7.34	136.30	7.44	-23.84	24.97
148401565437820928	044008.0+260525	70.0334	26.0903	7.34	136.32	5.73	-20.13	20.93
148400229703257856	043944.8+260152	69.9370	26.0312	7.31	136.85	7.46	-22.11	23.33
153001307909276928	042916.2+285627	67.3176	28.9409	7.30	137.05	-6.78	5.99	9.05
147818450613367424	043455.4+242853	68.7309	24.4813	7.29	137.20	3.48	-20.99	21.27

Continued on next page

Table C.1 – continued from previous page

Gaia DR2 ID	SSTtau ID	RA [deg]	Dec [deg]	Parallax [mas]	Distance [pc]	PMRA [mas yr^{-1}]	PMDec [mas yr^{-1}]	μ [mas yr^{-1}]
164470794735041152	041618.8+275215	64.0786	27.8708	7.28	137.29	7.47	-24.93	26.02
164506116546058112	041749.5+281331	64.4565	28.2254	7.28	137.37	8.81	-25.22	26.71
164474986623118592	041612.1+275638	64.0505	27.9439	7.27	137.49	8.89	-25.72	27.21
152029992465874560	042420.9+263051	66.0871	26.5141	7.27	137.59	9.25	-27.37	28.89
148449845165337600	043821.3+260913	69.5889	26.1537	7.23	138.31	5.47	-22.97	23.62
152518828462749440	042307.7+280557	65.7824	28.0992	7.19	139.05	9.65	-27.01	28.69
148449913884294528	043828.5+261049	69.6191	26.1803	7.17	139.38	6.13	-21.34	22.20
151262941369626752	042654.4+260651	66.7267	26.1141	7.15	139.91	3.98	-20.40	20.79
145157937416226176	043559.4+223829	68.9980	22.6413	7.13	140.33	11.85	-16.94	20.67
148384179410294272	044108.2+255607	70.2845	25.9353	7.10	140.83	7.20	-21.95	23.10
147441558642852736	044427.1+251216	71.1131	25.2045	7.09	141.01	6.45	-20.15	21.16
147679014500233728	044018.8+243234	70.0786	24.5427	7.07	141.50	-1.41	-43.35	43.38
163181308112262400	041426.2+280603	63.6095	28.1008	7.04	142.13	5.54	-27.64	28.19
151787064819255936	043126.6+270318	67.8613	27.0551	6.99	143.08	13.99	-19.89	24.32
148354733113981696	043903.9+254426	69.7665	25.7406	6.95	143.99	7.04	-20.61	21.77
148106316500918272	044303.0+252018	70.7628	25.3384	6.92	144.57	4.73	-20.21	20.75
163229544890946944	041353.2+281123	63.4721	28.1897	6.91	144.80	11.32	-22.68	25.35
148450875956969344	043814.8+261139	69.5620	26.1943	6.88	145.41	4.01	-23.17	23.51
148420639387738112	043800.8+255857	69.5036	25.9825	6.87	145.50	4.90	-22.63	23.16
152643240779301632	042900.6+275503	67.2529	27.9175	6.87	145.65	8.65	-25.26	26.70
145196527698016512	043319.0+224634	68.3295	22.7761	6.77	147.67	10.94	-20.15	22.93
145947077527182848	043309.4+224648	68.2895	22.7801	6.71	148.98	10.67	-16.76	19.87
148374391180009600	043955.7+254502	69.9823	25.7505	6.70	149.27	6.19	-20.34	21.26

Continued on next page

Table C.1 – continued from previous page

Gaia DR2 ID	SSTtau ID	RA [deg]	Dec [deg]	Parallax [mas]	Distance [pc]	PMRA [mas yr^{-1}]	PMDec [mas yr^{-1}]	μ [mas yr^{-1}]
150501362066641664	042216.4+254911	65.5686	25.8199	6.61	151.26	14.13	-19.65	24.20
148141775750936960	044039.7+251906	70.1658	25.3183	6.57	152.20	6.35	-20.57	21.53
151130591952773632	043307.8+261606	68.2826	26.2684	6.57	152.25	7.17	-17.31	18.74
151037064744973696	043158.4+254329	67.9936	25.7249	6.55	152.60	7.55	-21.14	22.45
145133786815830784	043541.8+223411	68.9244	22.5698	6.53	153.25	10.96	-17.96	21.04
147373010964871040	044642.6+245903	71.6776	24.9842	6.48	154.25	4.60	-19.52	20.06
152109054223716480	042423.2+265008	66.0968	26.8356	6.46	154.73	11.49	-18.35	21.65
145950895754320384	043224.1+225108	68.1007	22.8522	6.44	155.36	9.99	-17.43	20.09
152108882425024128	042426.4+264950	66.1103	26.8305	6.43	155.51	11.58	-17.86	21.29
151283870746458496	042629.3+262413	66.6225	26.4037	6.42	155.88	10.90	-17.85	20.92
145209442664192896	043552.8+225058	68.9703	22.8495	6.39	156.53	10.95	-16.53	19.83
148196510814073728	044110.7+255511	70.2950	25.9198	6.38	156.81	4.52	-20.11	20.61
163183644576299264	041449.2+281230	63.7054	28.2084	6.37	156.92	10.65	-21.17	23.70
145213192171160064	043553.4+225408	68.9730	22.9024	6.36	157.15	11.37	-18.48	21.70
152288824375681536	042216.7+265457	65.5699	26.9158	6.35	157.57	11.31	-17.60	20.92
152098299625634816	042247.8+264553	65.6996	26.7646	6.34	157.67	10.74	-17.14	20.23
145209618758377856	043547.3+225021	68.9473	22.8393	6.30	158.63	13.52	-15.90	20.87
145203159127518336	043352.0+225030	68.4668	22.8416	6.30	158.71	8.90	-17.07	19.25
144936836795636864	043917.7+222103	69.8242	22.3509	6.29	158.87	10.47	-17.38	20.29
145157941711889536	043558.9+223835	68.9956	22.6431	6.29	158.94	10.81	-15.77	19.12
145196252820109440	043326.2+224529	68.3593	22.7581	6.28	159.17	8.62	-16.75	18.84
145213295250374016	043552.0+225503	68.9671	22.9177	6.28	159.22	8.78	-8.09	11.94
148010281032823552	043339.0+252038	68.4129	25.3438	6.28	159.34	9.33	-18.29	20.53

Continued on next page

Table C.1 – continued from previous page

Gaia DR2 ID	SSTtau ID	RA [deg]	Dec [deg]	Parallax [mas]	Distance [pc]	PMRA [mas yr^{-1}]	PMDec [mas yr^{-1}]	μ [mas yr^{-1}]
152000786688289664	042444.5+261014	66.1858	26.1705	6.27	159.57	11.87	-17.32	21.00
148289831863907840	044138.8+255626	70.4118	25.9407	6.26	159.78	2.50	-15.48	15.68
164800235906366976	041542.7+290959	63.9283	29.1665	6.25	159.95	12.34	-17.75	21.62
164783811951433856	041639.1+285849	64.1631	28.9803	6.25	160.04	4.97	-15.00	15.80
148116276529733120	044207.7+252311	70.5325	25.3866	6.25	160.12	-0.74	-14.15	14.17
146319193494413696	042745.3+235724	66.9392	23.9567	6.24	160.18	11.27	-16.57	20.04
152293149405058816	042146.3+265929	65.4430	26.9914	6.23	160.47	11.92	-18.33	21.86
152104381299305600	042449.0+264310	66.2044	26.7195	6.21	160.97	10.61	-17.05	20.08
145132927822383616	043520.2+223214	68.8343	22.5373	6.20	161.40	9.83	-16.63	19.32
145203811962545152	043410.9+225144	68.5459	22.8623	6.18	161.77	8.90	-17.27	19.43
145213875069914496	043520.8+225424	68.8371	22.9066	6.18	161.83	9.72	-19.25	21.56
145212711134828672	043542.0+225222	68.9252	22.8729	6.17	162.07	10.02	-16.77	19.54
145210099794710272	043551.0+225240	68.9629	22.8777	6.16	162.32	6.32	-28.15	28.85
145225596036660224	043456.9+225835	68.7373	22.9765	6.15	162.68	11.70	-16.41	20.16
147562470562750720	043649.1+241258	69.2049	24.2163	6.14	162.85	43.42	-13.26	45.40
152099055539792000	042224.0+264625	65.6002	26.7738	6.13	163.27	11.41	-17.86	21.19
147248216395196672	044518.2+242436	71.3258	24.4101	6.11	163.54	-15.85	-2.85	16.10
145951789107603200	043249.1+225302	68.2047	22.8841	6.08	164.53	7.43	-15.79	17.45
145213192171159552	043554.1+225413	68.9757	22.9037	6.03	165.95	11.87	-9.99	15.51
152305248330621184	042134.5+270138	65.3942	27.0273	5.99	167.00	11.77	-16.63	20.38
164800815725933312	041524.0+291043	63.8505	29.1787	5.97	167.54	10.74	-19.44	22.20
152349022637314176	042025.5+270035	65.1065	27.0098	5.87	170.35	11.35	-17.73	21.05
145220064117853696	043610.3+225956	69.0433	22.9988	5.84	171.24	10.81	-15.96	19.27

Continued on next page

Table C.1 – continued from previous page

Gaia DR2 ID	SSTtau ID	RA [deg]	Dec [deg]	Parallax [mas]	Distance [pc]	PMRA [mas yr^{-1}]	PMDec [mas yr^{-1}]	μ [mas yr^{-1}]
146050057959093632	043119.0+233504	67.8295	23.5846	5.83	171.56	8.08	-16.60	18.47
145203704587705088	043415.2+225030	68.5637	22.8418	5.82	171.97	10.08	-17.50	20.19
151129011404806912	043344.6+261500	68.4361	26.2500	5.77	173.26	6.51	-17.31	18.50
145213187879627776	043552.7+225423	68.9700	22.9064	5.64	177.15	8.82	-13.95	16.51
145217379763796992	043638.9+225811	69.1622	22.9699	5.44	183.91	9.55	-15.97	18.61
152361426502650496	042115.2+272101	65.3136	27.3502	5.41	184.86	2.96	-4.53	5.41

D Compendium of Sources

This list details the 192 *Gaia* sources identified in our main study (Chapter 4). These sources fall within the distance and proper motion limits defined in our preliminary study and have been ordered by distance. Those sources highlighted have been identified as lying outside of our study area. There are 155 sources remaining in our study area that are discussed further in Chapter 4.

Sources in the 192 cohort, identified as being outside the study area.
13 sources rejected as lying beyond 172 pc (see Section 4.3.1).

Table D.1 Compendium of 192 *Gaia* Sources

Gaia DR2 ID	RA [deg]	Dec [deg]	Parallax [mas]	Distance [pc]	PMRA [mas yr^{-1}]	PMDec [mas yr^{-1}]	μ [mas yr^{-1}]
147838688499178624	68.6911	24.7539	8.94	111.88	-1.27	-20.27	20.31
164513602672978304	64.6692	28.3209	8.52	117.44	6.62	-29.87	30.60
152416436443721728	65.2890	27.8434	8.45	118.31	7.95	-26.85	28.00
164550882989640192	65.5132	28.4274	8.31	120.27	10.27	-25.86	27.83
146874275068113664	70.0028	23.9724	8.30	120.49	8.62	-20.74	22.46
151262700852297728	66.7696	26.1044	8.25	121.18	6.16	-19.30	20.26
146487560507840768	70.4402	23.0327	8.02	124.75	8.30	-21.55	23.10
147605282796916992	68.9207	24.1857	7.99	125.23	5.90	-21.53	22.32
146708734143437568	69.7892	23.4001	7.96	125.63	7.81	-21.29	22.68
164513538249595136	64.6960	28.3353	7.95	125.77	8.30	-25.31	26.63
146758968080949504	69.5679	23.4444	7.94	125.94	7.85	-21.80	23.17
152118881108855680	66.1878	27.0290	7.89	126.73	8.39	-26.84	28.13
146767764173923328	69.7442	23.6097	7.89	126.82	8.64	-21.20	22.89
146881048231272192	69.8902	23.9891	7.87	127.12	7.28	-20.99	22.22
149525098819498752	65.7258	24.6648	7.86	127.23	7.99	-23.41	24.74
152511475478780416	65.4819	27.9183	7.85	127.37	10.75	-27.22	29.27
147523609698860160	68.9873	23.8631	7.85	127.43	8.53	-21.34	22.98
151793082068521856	67.8102	27.1715	7.84	127.49	9.17	-27.58	29.06
164445437248152832	65.1087	28.0691	7.84	127.51	8.33	-26.07	27.37
149623711269425408	65.9133	24.9372	7.82	127.80	6.92	-21.70	22.77
146764809236423808	69.7568	23.6007	7.82	127.81	8.57	-21.85	23.47
151574107455728256	68.8820	27.2521	7.82	127.82	8.85	-27.17	28.58
146767935972608128	69.7739	23.6364	7.82	127.90	8.74	-22.41	24.06
162758236656524416	63.6995	26.8030	7.82	127.93	9.02	-22.45	24.20

Continued on next page

Table D.1 – continued from previous page

Gaia DR2 ID	RA [deg]	Dec [deg]	Parallax [mas]	Distance [pc]	PMRA [mas yr^{-1}]	PMDec [mas yr^{-1}]	μ [mas yr^{-1}]
165259178932295552	65.3605	29.8798	7.81	127.96	9.11	-23.31	25.02
148037764527442944	69.0796	25.7163	7.81	128.02	8.91	-27.47	28.88
163184366130809984	63.5539	28.2033	7.80	128.13	8.93	-29.05	30.40
147606657186323712	68.8641	24.2496	7.80	128.22	6.05	-20.77	21.64
151327159721125888	67.4403	26.5128	7.80	128.23	6.87	-20.97	22.06
164530511961426176	65.4173	28.2395	7.79	128.39	8.36	-25.98	27.29
162757545164429696	63.6971	26.7739	7.78	128.47	9.48	-22.69	24.59
164423034698790656	64.9509	27.8334	7.78	128.59	9.40	-26.11	27.75
163177116226018944	63.6975	28.0514	7.77	128.69	10.16	-26.13	28.03
163246832135164544	63.3090	28.3195	7.76	128.85	8.37	-24.40	25.80
164698634160139264	64.3906	28.3462	7.76	128.88	9.18	-25.55	27.15
151499478104075008	69.3406	26.8503	7.76	128.95	8.63	-27.00	28.34
164436297557793280	64.8551	27.9369	7.75	128.99	8.98	-26.26	27.75
164832740220756608	64.8160	29.1074	7.75	129.07	8.63	-26.18	27.56
147790206908395776	68.3940	24.3515	7.74	129.26	7.75	-20.48	21.90
146709146460303744	69.7447	23.3998	7.73	129.39	7.16	-21.45	22.61
149369139966814976	67.4003	24.5987	7.73	129.42	8.57	-20.20	21.94
164666022471759232	64.1171	28.1265	7.70	129.84	6.85	-25.90	26.80
164409359522965120	64.6263	27.7221	7.70	129.89	8.73	-26.27	27.68
145238687096970496	68.7855	23.1943	7.69	129.96	7.24	-20.98	22.19
147796013704188928	68.1324	24.3341	7.69	130.03	7.12	-21.50	22.65
147796013704189440	68.1274	24.3325	7.68	130.21	6.65	-21.86	22.85
146277553787186048	68.0972	24.0503	7.68	130.24	7.36	-22.42	23.60

Continued on next page

Table D.1 – continued from previous page

Gaia DR2 ID	RA [deg]	Dec [deg]	Parallax [mas]	Distance [pc]	PMRA [mas yr^{-1}]	PMDec [mas yr^{-1}]	μ [mas yr^{-1}]
164705368668853120	64.4123	28.5500	7.68	130.27	6.87	-25.25	26.17
151028990206478080	68.0138	25.4687	7.67	130.39	8.09	-22.81	24.20
164518589131083136	64.6297	28.4544	7.67	130.44	8.68	-25.10	26.56
152226491513195648	66.2379	27.1989	7.66	130.57	8.36	-26.75	28.02
147831571737487488	68.2918	24.5619	7.66	130.60	7.25	-21.23	22.43
151795487250202240	67.9967	27.1885	7.66	130.63	8.44	-27.38	28.65
164676575208109568	64.0720	28.2868	7.63	131.11	8.27	-25.35	26.66
149327461604161408	66.7665	24.1121	7.63	131.14	9.73	-28.36	29.98
164738521519622656	63.5609	28.4660	7.62	131.24	9.50	-23.57	25.41
164684340508950144	63.9132	28.3162	7.61	131.49	9.25	-24.38	26.08
164504467278644096	64.8595	28.4372	7.60	131.70	8.36	-25.47	26.81
152178976290554496	67.0653	27.1863	7.59	131.78	8.19	-26.73	27.96
146028102086382464	68.1027	23.3605	7.58	131.89	8.19	-21.95	23.43
163511608280866816	61.3840	27.5537	7.58	132.00	11.43	-25.32	27.78
152191100981965824	66.9246	27.1653	7.57	132.03	12.16	-10.43	16.02
152466120624336896	66.6854	27.9453	7.57	132.14	8.84	-25.18	26.69
152362491654557696	65.1633	27.2920	7.51	133.07	10.41	-26.09	28.09
147847072275324416	67.9607	24.4048	7.50	133.32	4.46	-22.96	23.39
151262876946558976	66.7388	26.1078	7.50	133.36	5.19	-20.71	21.35
162933226506362240	63.7772	27.4703	7.48	133.66	10.39	-26.67	28.62
152516079683687680	65.7754	28.0220	7.47	133.88	7.93	-26.68	27.84
148450085683504896	69.6471	26.1773	7.46	133.96	4.89	-21.78	22.32
151374198202645376	67.4270	26.5469	7.40	135.12	6.90	-21.21	22.30

Continued on next page

Table D.1 – continued from previous page

Gaia DR2 ID	RA [deg]	Dec [deg]	Parallax [mas]	Distance [pc]	PMRA [mas yr^{-1}]	PMDec [mas yr^{-1}]	μ [mas yr^{-1}]
163179006011625088	63.7179	28.0998	7.39	135.23	7.99	-22.16	23.56
151374202498079872	67.4232	26.5494	7.39	135.35	7.07	-20.70	21.87
162967384383246336	63.9917	27.7714	7.37	135.67	7.82	-24.65	25.86
163181342473839744	63.5734	28.1026	7.37	135.69	8.34	-23.32	24.76
3413006177063524352	71.1633	22.4115	7.35	135.96	7.74	-26.78	27.87
148112913570653568	70.5876	25.3428	7.34	136.16	4.89	-19.42	20.03
163233981593016064	63.3635	28.2734	7.34	136.30	7.44	-23.84	24.97
148400229703257856	69.9370	26.0312	7.31	136.85	7.46	-22.11	23.33
164474986623118592	64.0505	27.9439	7.27	137.49	8.89	-25.72	27.21
148381984682184192	70.2063	25.8552	7.15	139.94	4.38	-19.63	20.11
162174155463688960	62.4579	25.1780	7.12	140.36	24.90	-31.01	39.77
147441558642852736	71.1131	25.2045	7.09	141.01	6.45	-20.15	21.16
148106316500918272	70.7628	25.3384	6.92	144.57	4.73	-20.21	20.75
150073682105601408	63.1696	24.6376	6.84	146.22	14.26	-18.84	23.63
158254087272066304	72.0907	29.4681	6.81	146.84	5.36	-24.73	25.31
152104381299305856	66.2053	26.7174	6.76	147.87	12.67	-17.45	21.56
151851867285622528	68.1198	27.7698	6.76	147.98	13.96	-20.80	25.05
156902512603777408	74.0085	30.3509	6.73	148.60	5.65	-21.74	22.47
164058443515179776	62.3103	28.7561	6.65	150.40	2.33	-17.60	17.75
162259951730099968	61.7236	25.6768	6.64	150.69	14.32	-18.86	23.68
151801500204394624	68.1057	27.3674	6.63	150.76	16.22	-32.63	36.44
146055624236793472	68.1274	23.4823	6.57	152.16	11.26	-17.76	21.03
146469246765971200	69.8226	22.7981	6.57	152.29	8.91	-19.20	21.16

Continued on next page

Table D.1 – continued from previous page

Gaia DR2 ID	RA [deg]	Dec [deg]	Parallax [mas]	Distance [pc]	PMRA [mas yr^{-1}]	PMDec [mas yr^{-1}]	μ [mas yr^{-1}]
146686292938953216	70.0596	23.1317	6.56	152.41	10.23	-16.53	19.44
151037064744973696	67.9936	25.7249	6.55	152.60	7.55	-21.14	22.45
152057239738385792	66.2092	26.6834	6.53	153.22	12.34	-17.22	21.18
145133786815830784	68.9244	22.5698	6.53	153.25	10.96	-17.96	21.04
162259814291151616	61.6852	25.6717	6.51	153.70	14.01	-18.78	23.43
157018884742748032	73.9849	30.8270	6.47	154.44	5.49	-25.55	26.13
152109054223716480	66.0968	26.8356	6.46	154.73	11.49	-18.35	21.65
156901138214266112	73.9390	30.3274	6.46	154.75	3.62	-25.05	25.31
145950895754320384	68.1007	22.8522	6.44	155.36	9.99	-17.43	20.09
156730056780790528	74.6929	29.9124	6.43	155.43	4.09	-25.42	25.75
159965197946584320	72.9475	30.7870	6.43	155.61	4.38	-25.97	26.34
158252399348280704	72.0887	29.4532	6.39	156.49	5.42	-24.74	25.32
156900966415569920	73.9571	30.3277	6.39	156.51	4.83	-23.02	23.53
145209442664192896	68.9703	22.8495	6.39	156.53	10.95	-16.53	19.83
156732977357829888	74.7627	30.0500	6.39	156.55	4.59	-24.73	25.16
156915878541979264	73.9483	30.4687	6.38	156.74	3.48	-24.00	24.25
151526175620701824	68.2689	26.5602	6.37	156.97	8.60	-15.24	17.0
156948382855058176	74.3688	30.4863	6.37	157.00	4.19	-24.56	24.91
157921244486727680	69.7519	28.2797	6.36	157.14	-0.97	-16.18	16.21
145213192171160064	68.9730	22.9024	6.36	157.15	11.37	-18.48	21.70
157015075106952832	73.9186	30.6515	6.36	157.26	4.09	-24.11	24.46
152098299625634816	65.6996	26.7646	6.34	157.67	10.74	-17.14	20.23
153111533949842816	67.3526	29.6871	6.33	157.90	-21.20	-23.34	31.53

Continued on next page

Table D.1 – continued from previous page

Gaia DR2 ID	RA [deg]	Dec [deg]	Parallax [mas]	Distance [pc]	PMRA [mas yr^{-1}]	PMDec [mas yr^{-1}]	μ [mas yr^{-1}]
3419944920068400000	75.6661	24.9926	6.33	158.07	4.66	-26.48	26.89
156616124184955776	74.7163	29.5960	6.31	158.43	4.51	-24.97	25.37
156577881796362496	74.1999	29.2197	6.31	158.56	5.91	-24.47	25.18
145203159127518336	68.4668	22.8416	6.30	158.71	8.90	-17.07	19.25
144936836795636864	69.8242	22.3509	6.29	158.87	10.47	-17.38	20.29
145157941711889536	68.9956	22.6431	6.29	158.94	10.81	-15.77	19.12
148250936640162048	71.1413	25.8831	6.29	159.03	8.25	-26.35	27.61
145196252820109440	68.3593	22.7581	6.28	159.17	8.62	-16.75	18.84
156640004202940672	74.4681	29.9019	6.28	159.29	3.85	-24.98	25.28
148010281032823552	68.4129	25.3438	6.28	159.34	9.33	-18.29	20.53
3412249541265750912	75.6271	22.2805	6.27	159.57	4.28	-23.96	24.34
156907907082740480	73.7958	30.3664	6.26	159.64	3.90	-24.45	24.76
146734503947264640	69.4116	23.3496	6.26	159.67	2.75	-17.99	18.20
164800235906366976	63.9283	29.1665	6.25	159.95	12.34	-17.75	21.62
165891088881410176	62.0925	30.1506	6.24	160.13	21.83	-26.44	34.29
156730056780026240	74.6951	29.9112	6.23	160.55	3.25	-24.37	24.59
3419631520599185664	75.2549	25.0280	6.22	160.72	5.18	-26.27	26.78
155447893079715456	75.6452	27.7637	6.22	160.83	4.27	-24.57	24.94
152104381299305600	66.2044	26.7195	6.21	160.97	10.61	-17.05	20.08
151286550806099712	66.8529	26.4054	6.20	161.17	11.20	-18.05	21.24
145494460991086976	66.7809	22.2510	6.20	161.23	7.24	-17.22	18.68
152280165721635968	65.4788	26.7103	6.20	161.27	10.14	-16.87	19.68
158165714024754688	70.6157	29.6624	6.20	161.32	5.21	-21.34	21.96

Continued on next page

Table D.1 – continued from previous page

Gaia DR2 ID	RA [deg]	Dec [deg]	Parallax [mas]	Distance [pc]	PMRA [mas yr^{-1}]	PMDec [mas yr^{-1}]	μ [mas yr^{-1}]
156916325218569856	73.9509	30.5043	6.20	161.33	3.85	-24.43	24.73
158234192983875328	72.2394	29.2310	6.19	161.59	4.10	-24.29	24.63
145203811962545152	68.5459	22.8623	6.18	161.77	8.90	-17.27	19.43
145213875069914496	68.8371	22.9066	6.18	161.83	9.72	-19.25	21.56
151127907597788672	68.4780	26.2242	6.17	161.99	9.46	-17.47	19.87
145886539965771648	67.3755	22.6542	6.17	162.04	9.02	-17.73	19.89
145212711134828672	68.9252	22.8729	6.17	162.07	10.02	-16.77	19.53
152104381299305728	66.2007	26.7211	6.17	62.18	10.47	-14.54	17.92
145210099794710272	68.9629	22.8777	6.16	162.32	6.32	-28.15	28.85
156842486140929024	73.9705	30.1145	6.15	162.66	13.24	-10.70	17.02
145225596036660224	68.7373	22.9765	6.15	162.68	11.70	-16.41	20.16
151338056053442048	68.0093	26.5288	6.14	162.76	18.17	-26.24	31.92
153402045537055360	73.8062	26.4977	6.13	163.08	14.63	-8.99	17.17
152099055539792000	65.6002	26.7738	6.13	163.26	11.41	-17.86	21.19
163222814678059648	63.3619	28.0827	6.11	163.70	-4.44	-32.55	32.85
147727672184672640	68.9951	24.6445	6.10	163.90	10.20	-15.05	18.18
145951789107603200	68.2047	22.8841	6.08	164.53	7.43	-15.79	17.45
147272848031900160	71.1868	24.7570	6.07	164.61	15.92	-5.63	16.89
156915878541979008	73.9501	30.4679	6.07	164.83	4.60	-23.70	24.14
151791982556895360	67.8599	27.1223	6.06	165.15	25.26	-22.34	33.72
156915290131026816	73.8472	30.4600	6.05	165.30	4.99	-25.00	25.49
156574617621217792	74.2505	29.1830	6.05	165.32	4.75	-24.73	25.18
159563983577848192	71.1477	31.5548	6.03	165.80	22.08	-8.93	23.82

Continued on next page

Table D.1 – continued from previous page

Gaia DR2 ID	RA [deg]	Dec [deg]	Parallax [mas]	Distance [pc]	PMRA [mas yr^{-1}]	PMDec [mas yr^{-1}]	μ [mas yr^{-1}]
145213192171159552	68.9757	22.9037	6.03	165.95	11.87	-9.98	15.51
158197973524029696	71.9173	28.8446	5.99	166.93	7.73	-25.80	26.93
152305248330621184	65.3942	27.0273	5.99	167.00	11.77	-16.63	20.38
145125987155266048	68.6505	22.4206	5.99	167.03	12.01	-17.87	21.53
152009028728671744	66.3238	26.2973	5.98	167.15	28.99	-11.37	31.14
145982742935380096	68.6894	23.1340	5.98	167.20	10.96	-17.55	20.69
164265220422661760	61.6777	29.0337	5.97	167.40	11.03	-17.80	20.94
164545351071767168	65.1079	28.2782	5.93	168.60	-0.32	-17.19	17.19
166173869528755968	64.3201	30.8977	5.90	169.36	19.53	-24.62	31.42
3420008412568724736	75.7775	25.3887	5.90	169.58	3.00	-17.18	17.44
155754583809675392	74.8787	8.7896	5.88	170.19	4.47	-24.84	25.24
155162123136347648	72.7445	28.8726	5.85	171.08	6.83	-25.62	26.51
158494605440901760	70.8343	29.6683	5.84	171.17	2.61	-22.06	22.22
151793868047070848	67.8802	27.2454	5.83	171.62	17.82	-25.04	30.74
163984707516695296	62.3842	28.3836	5.79	172.78	-12.39	-10.39	16.17
3412561424610676480	74.3177	22.8115	5.78	173.12	13.13	-19.63	23.61
153215880179436928	72.4755	25.2581	5.77	173.34	28.76	-3.91	29.04
151825891323215104	68.1356	27.4525	5.77	173.42	7.25	31.08	31.91
150313483015851264	64.5233	24.7978	5.74	174.09	34.49	-18.84	39.30
165680429326185472	63.8521	29.8504	5.74	174.10	-0.23	-35.69	35.69
147862736020188032	67.6732	24.5114	5.74	174.25	17.97	-33.46	37.98
164073866741018880	62.7258	28.8380	5.72	174.82	-7.83	-25.43	26.61
147982484004552704	69.1158	25.4501	5.71	175.19	-26.63	-13.37	29.79

Continued on next page

Table D.1 – continued from previous page

Gaia DR2 ID	RA [deg]	Dec [deg]	Parallax [mas]	Distance [pc]	PMRA [mas yr^{-1}]	PMDec [mas yr^{-1}]	μ [mas yr^{-1}]
158547519437976064	70.6895	29.8618	5.68	176.03	19.73	-23.87	30.97
152134888450886912	66.0065	27.1636	5.66	176.57	-23.76	-16.69	29.04
145873345826129024	67.8252	22.8916	5.65	176.99	34.21	-10.63	35.82
145213187879627776	68.9700	22.9064	5.64	177.15	8.82	-13.95	16.51
163941105010724480	62.0356	28.3912	5.64	177.23	-28.49	-19.37	34.45
164036517705037312	62.2062	28.5142	5.63	177.65	5.59	-31.50	32.00
146783397854852352	69.7671	23.8157	5.62	177.96	13.30	-14.34	19.56

E Redshift values for *Gaia* associations

This appendix contains the details of those sources in our *Gaia* ‘near’ and ‘far’ groups that have redshift values in the LAMOST DR5 catalogue. We provide values for source α, δ, π and z, along with their errors.

Table E.1 *Gaia* Redshift Values (Far Group)

Gaia DR2 ID	RA [deg]	RA error [deg]	Dec [deg]	Dec error [deg]	Parallax [mas yr^{-1}]]	Parallax error [mas yr^{-1}]	Redshift	Redshift error
163511608280866816	61.3840	0.0944	27.5537	0.0411	7.58	0.12	0.00015254	0.00002461
150073682105601408	63.1696	0.0729	24.6376	0.0356	6.84	0.08	0.00012694	0.00002788
163246832135164544	63.3090	0.0535	28.3195	0.0266	7.76	0.06	0.00003266	0.00000866
163233981593016064	63.3635	0.0619	28.2734	0.0323	7.34	0.07	0.00008389	0.00000614
163184366130809984	63.5539	0.1345	28.2033	0.0701	7.80	0.14	-0.0000046	0.000017412
164738521519622656	63.5609	0.0602	28.4660	0.0340	7.62	0.06	0.00007532	0.00000947
163181342473839744	63.5734	0.0786	28.1026	0.0402	7.37	0.09	0.0001874	0.0000402
162757545164429696	63.6971	0.0483	26.7739	0.0254	7.78	0.05	0.00008263	0.00000921
163177116226018944	63.6975	0.0658	28.0514	0.0340	7.77	0.08	0.0001351	0.00001893
162758236656524416	63.6995	0.0383	26.8030	0.0202	7.82	0.04	0.0000786	0.00001075
163179006011625088	63.7179	0.0825	28.0998	0.0419	7.39	0.09	0.00009948	0.00001006
164684340508950144	63.9132	0.0715	28.3162	0.0364	7.61	0.08	0.00009409	0.00001043
162967384383246336	63.9917	0.0967	27.7714	0.0510	7.37	0.11	-0.00012142	0.0000316
164474986623118592	64.0505	0.1151	27.9439	0.0610	7.27	0.12	-0.00014138	0.00009018
164676575208109568	64.0720	0.1009	28.2868	0.0516	7.63	0.12	0.00014384	0.0000223
164666022471759232	64.1171	0.0361	28.1265	0.0199	7.70	0.04	0.00009496	0.00000731
164705368668853120	64.4123	0.0500	28.5500	0.0244	7.68	0.06	0.00009221	0.00000703
164409359522965120	64.6263	0.0882	27.7223	0.0458	7.70	0.09	-0.00005364	0.00002271
164832740220756608	64.8160	0.0542	29.1074	0.0267	7.75	0.06	-0.0000506	0.00003961
164436297557793280	64.8550	0.0762	27.9369	0.0347	7.75	0.08	0.0001348	0.00000915
164504467278644096	64.8595	0.0607	28.4372	0.0224	7.59	0.06	0.0000308	0.000014977
164423034698790656	64.9509	0.0438	27.8334	0.0218	7.78	0.05	0.00008334	0.00001364
164445437248152832	65.1087	0.0470	28.0691	0.0204	7.84	0.05	0.00010656	0.00001257
152362491654557696	65.1633	0.0582	27.2920	0.0282	7.51	0.06	0.00007917	0.00001011

Continued on next page

Table E.1 – continued from previous page

Gaia DR2 ID	RA [deg]	RA error [deg]	Dec [deg]	Dec error [deg]	Parallax [mas yr^{-1}]]	Parallax error [mas yr^{-1}]	Redshift	Redshift error
152416436443721728	65.2890	0.0935	27.8434	0.0401	8.45	0.10	0.00014871	0.00002146
164530511961426176	65.4173	0.0854	28.2395	0.0389	7.79	0.09	0.00017319	0.00003068
152511475478780416	65.4819	0.0635	27.9183	0.0255	7.85	0.07	0.00008049	0.00001346
164550882989640192	65.5132	0.1230	28.4274	0.0623	8.31	0.14	0.00008197	0.00000755
152118881108855680	66.1878	0.0750	27.0290	0.0389	7.89	0.08	-0.00004815	0.00002092
152466120624336896	66.6854	0.1509	27.9453	0.0948	7.57	0.18	0.0003016	0.00009918
152178976290554496	67.0653	0.1258	27.1863	0.0738	7.59	0.12	-0.00038064	0.00006867
149369139966814976	67.4003	0.0826	24.5987	0.0545	7.73	0.09	0.00009182	0.00001073
147847072275324416	67.9607	0.0839	24.4048	0.0518	7.50	0.09	0.00009871	0.00000763
146028102086382464	68.1027	0.0698	23.3605	0.0448	7.58	0.07	0.00013891	0.0000131
147831571737487488	68.2918	0.0440	24.5619	0.0292	7.66	0.04	0.0000505	0.0000133
147838688499178624	68.6911	0.1025	24.7539	0.0662	8.94	0.11	0.00006155	0.00001153
147606657186323712	68.8641	0.0544	24.2496	0.0361	7.80	0.05	0.000040895	0.0000163
151574107455728256	68.8820	0.0598	27.2522	0.0389	7.82	0.07	0.00003198	0.00001321
147605282796916992	68.9207	0.1234	24.1857	0.0816	7.99	0.15	0.00010215	0.00001168
147523609698860160	68.9873	0.0840	23.8631	0.0524	7.85	0.09	0.00014501	0.00002114
148037764527442944	69.0796	0.0746	25.7163	0.0461	7.81	0.08	0.0000489	0.0000127
151499478104075008	69.3406	0.0620	26.8503	0.0419	7.76	0.07	0.00010319	0.00001317
146758968080949504	69.5679	0.0928	23.4444	0.0560	7.94	0.11	0.00012947	0.00001974
148450085683504896	69.6471	0.1060	26.1773	0.0776	7.46	0.12	0.00009617	0.00000807
146767764173923328	69.7442	0.1094	23.6097	0.0649	7.89	0.12	0.00021063	0.00004334
146764809236423808	69.7568	0.0771	23.6007	0.0462	7.82	0.08	0.00007466	0.00001409
146767935972608128	69.7739	0.1077	23.6364	0.0575	7.82	0.10	0.00013689	0.00002066

Continued on next page

Table E.1 – continued from previous page

Gaia DR2 ID	RA [deg]	RA error [deg]	Dec [deg]	Dec error [deg]	Parallax [mas yr^{-1}]]	Parallax error [mas yr^{-1}]	Redshift	Redshift error
146708734143437568	69.7892	0.0556	23.4001	0.0319	7.96	0.06	0.0000746	0.00001015
146881048231272192	69.8902	0.0930	23.9891	0.0577	7.87	0.10	0.00017134	0.00002594
146874275068113664	70.0028	0.1230	23.9724	0.0783	8.30	0.16	-0.00001664	0.00006095
148381984682184192	70.2063	0.0508	25.8552	0.0315	7.15	0.06	0.00005351	0.00001309
146487560507840768	70.4402	0.0844	23.0327	0.0534	8.02	0.08	0.00009908	0.00001129
148106316500918272	70.7628	0.0444	25.3384	0.0268	6.92	0.05	0.00008943	0.00001053
3413006177063524352	71.1633	0.0642	22.4115	0.0383	7.35	0.07	0.00007079	0.00001278
158254087272066304	72.0907	0.1250	29.4681	0.0819	6.81	0.14	-0.00016385	0.00018202
164265220422661760	61.6777	0.1225	29.0337	0.0492	5.97	0.14	0.0001551	0.00002342
162259951730099968	61.7236	0.1162	25.6768	0.0485	6.64	0.12	0.00013682	0.00003023
163941105010724480	62.0356	0.0375	28.3912	0.0158	5.64	0.04	-0.00000837	0.0000162
164036517705037312	62.2062	0.0431	28.5142	0.0158	5.63	0.04	0.000112411	0.0000204
164058443515179776	62.3103	0.0480	28.7561	0.0176	6.65	0.05	0.0000344	0.0000155
163984707516695296	62.3842	0.0437	28.3836	0.0203	5.79	0.04	0.0000174	0.0000144
164073866741018880	62.7258	0.0442	28.8380	0.0246	5.72	0.05	0.0000842	0.0000194
163222814678059648	63.3619	0.0883	28.0827	0.0371	6.11	0.09	-0.000115947	0.0000187
164800235906366976	63.9283	0.0597	29.1665	0.0284	6.25	0.07	0.00008785	0.00000717
150313483015851264	64.5233	0.1084	24.7978	0.0509	5.74	0.13	0.00013506	0.00002228
164545351071767168	65.1079	0.0457	28.2782	0.01769	5.93	0.05	0.0000147	0.000014
152305248330621184	65.3942	0.1293	27.0273	0.0589	5.99	0.14	0.00027937	0.00004322
152280165721635968	65.4785	0.1084	26.7103	0.0455	6.20	0.13	0.00017436	0.00003326
152134888450886912	66.0065	0.0526	27.1636	0.0279	5.66	0.06	-0.00000163	0.0000127
152109054223716480	66.0968	0.0825	26.8356	0.0424	6.46	0.09	-0.00235295	0.00005558

Continued on next page

Table E.1 – continued from previous page

Gaia DR2 ID	RA [deg]	RA error [deg]	Dec [deg]	Dec error [deg]	Parallax [mas yr^{-1}]]	Parallax error [mas yr^{-1}]	Redshift	Redshift error
152009028728671744	66.3238	0.1832	26.2973	0.1057	5.98	0.19	0.00008875	0.00000713
145886539965771648	67.3755	0.0488	22.6542	0.0242	6.17	0.05	0.00005407	0.00000729
147862736020188032	67.6732	0.0375	24.5114	0.0265	5.74	0.04	0.00010634	0.0000138
145873345826129024	67.8252	0.0401	22.8916	0.0254	5.65	0.04	0.0000586	0.0000162
151791982556895360	67.8599	0.0825	27.1223	0.0550	6.06	0.10	0.000160878	0.0000222
151793868047070848	67.8802	0.0923	27.2454	0.0590	5.83	0.10	-0.00006044	0.00000412
151338056053442048	68.0093	0.1375	26.5288	0.08611	6.14	0.15	0.00013118	0.00002104
151526175620701824	68.2689	0.0928	26.5602	0.0614	6.37	0.11	0.00012095	0.00001633
145203159127518336	68.4668	0.0436	22.8416	0.0305	6.30	0.05	0.00010252	0.00000946
151127907597788672	68.4780	0.0742	26.2242	0.0430	6.17	0.08	0.000103	0.000004
145203811962545152	68.5459	0.0577	22.8622	0.0370	6.18	0.06	0.00009823	0.00000801
145225596036660224	68.7373	0.0532	22.9765	0.0287	6.15	0.06	0.00007564	0.00000581
145213875069914496	68.8371	0.0618	22.9066	0.0351	6.18	0.06	0.000064	0.000002
145212711134828672	68.9252	0.1211	22.8729	0.0704	6.17	0.13	0.00015097	0.00003265
145213187879627776	68.9700	0.1094	22.9064	0.0580	5.64	0.11	0.00004146	0.00002009
145209442664192896	68.9703	0.0875	22.8495	0.0515	6.39	0.09	0.00011212	0.00001044
147727672184672640	68.9951	0.0591	24.6445	0.0413	6.10	0.07	0.00010248	0.00000785
147982484004552704	69.1158	0.0645	25.4501	0.0381	5.71	0.06	0.000132625	0.0000255
146734503947264640	69.4116	0.0648	23.3496	0.0433	6.26	0.06	0.0000865	0.0000133
157921244486727680	69.7519	0.0920	28.2797	0.0640	6.36	0.10	0.0000186	0.00000778
146469246765971200	69.8226	0.0988	22.7981	0.0638	6.57	0.12	0.0001539	0.00004354
146686292938953216	70.0596	0.1069	23.1317	0.0629	6.56	0.11	0.0000844	0.00012816
148250936640162048	71.1413	0.0644	25.8831	0.0381	6.29	0.08	0.00012021	0.00001392

Continued on next page

Table E.1 – continued from previous page

Gaia DR2 ID	RA [deg]	RA error [deg]	Dec [deg]	Dec error [deg]	Parallax [mas yr^{-1}]]	Parallax error [mas yr^{-1}]	Redshift	Redshift error
147272848031900160	71.1868	0.0503	24.7570	0.0309	6.07	0.06	-0.0000428	0.0000156
158197973524029696	71.9173	0.0546	28.8446	0.0312	5.99	0.05	0.0000639	0.00000841
158234192983875328	72.2394	0.0907	29.2310	0.0604	6.19	0.10	0.00018859	0.00003899
153215880179436928	72.47555	0.0357	25.2581	0.0228	5.77	0.04	0.000113	0.00004455
155162123136347648	72.7445	0.0732	28.8726	0.0434	5.85	0.0	0.00007273	0.00001185

F Underpinning Knowledge

F.1 Molecular Clouds

Molecular clouds, ubiquitous along our Galactic plane are dense, compact regions where gas and dust have clumped together. In contrast to the general interstellar medium where temperatures can range between 50 to 10^4 K and where densities are as low as 0.2 to 50 particles cm^{-3}, molecular clouds have an average density of 10^2 to 10^3 molecules cm^{-3} with internal temperatures of only 10 to 20 K (Ferriere, 2001).

Table F.1 Constituents of Molecular Clouds

Factor	Composition
GAS	99% by mass, of which
H_2	99%
He	25% of mass
CO	10^{-4} by number
CS	10^{-9} by number
NH_3	10^{-9} by number
N_2H+	10^{-10} by number
DUST	1% by mass
silicates + carbonaceous	

We can begin to understand the structure of molecular clouds through radial velocity measurements of the gas contained within them. These clouds consist mainly of molecular hydrogen (H_2) but because of its structure and its lack of a permanent electric dipole (H_2) is virtually invisible (i.e. optically thick) at temperatures below $\sim$200K (Bolatto, Wolfire, and Leroy, 2013). This makes it difficult to detect and proxy tracers are used to infer its presence. Tracers such as carbon monoxide (CO), which is the most abundant molecule after H_2 only constitutes a small percentage of the gas contained in the cloud (Table F.1) but it has a lower frequency transition that can more easily be detected. By mapping the presence of CO emission and those of its isotopes ^{12}CO and ^{13}CO it is possible to effectively map out the locations and some of the internal structures within molecular clouds (Figure F.1).

The ratio between H_2 mass (M) and CO luminosity (L') is described by the relationship

$$\alpha = \frac{MH_2}{L'CO(1 \rightarrow 0)} \tag{F.1}$$

for the $(1 \rightarrow 0)$ transition at 115 GHz (Bolatto, Wolfire, and Leroy, 2013). This value is taken to be a constant with a standard Galactic value of α=4.6 $M_{\odot}/(K\ km^{-1}\ pc^2)$ which has been empirically verified using different techniques (Dickman, 1978; Bloemen, 1987; Solomon et al., 1987). Subsequent studies of Luminous and Ultraluminous infrared galaxies (Downes and Solomon, 1998; Papadopoulos et al., 2012) have found a significantly smaller value of α=0.8 $M_{\odot}/(K\ km^{-1}\ pc^2)$ indicating that this may not be a universal constant.

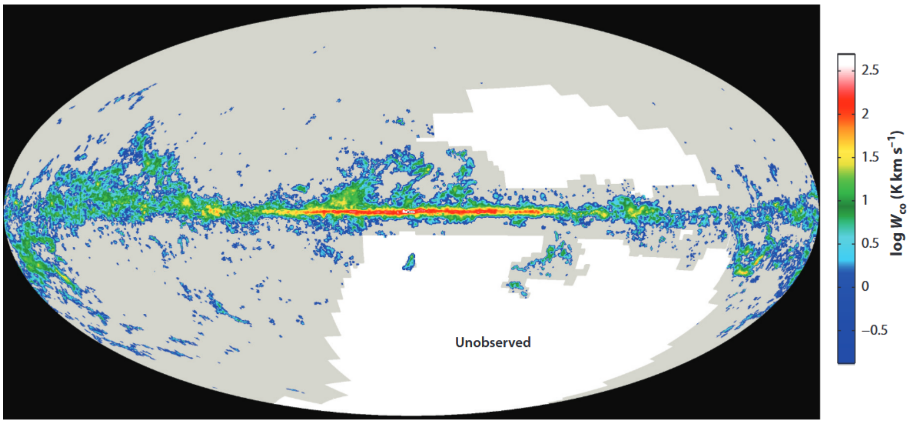

Figure F.1 Composite image of galactic ^{12}CO emission constructed from the surveys of Dame, Hartmann, and Thaddeus (2001) and Mizuno and Fukui (2004) From: (Heyer and Dame, 2015: Figure 3).

There have been many investigations aimed at determining the physical properties of molecular clouds and to understand how their gravity, magnetic fields and turbulence shape their complex structure. We still do not fully understand whether molecular clouds are gravitationally bound or whether they are merely transient features.

The Solomon et al. (1987) study of 237 molecular clouds in the Galactic disk was able to determine that the clouds were characterised by a constant mean surface density of 170 $M_{\odot}pc^{-2}$ and that molecular clouds are either in or near virial equilibrium and are thus gravitationally bound. Such a conclusion however presents a problem which was highlighted by the study of Zuckerman and Evans (1974). The idea that molecular clouds are gravitationally bound is not observationally supportable. Namely, if molecular clouds are gravitationally bound, and if they collapse in the order of their free-fall time (i.e. the time it would take the cloud to collapse under its own gravitational forces if no other forces oppose the collapse) then the rate of star formation should be in the order of two magnitudes greater than that observed (Zuckerman and Evans, 1974).

The standard picture of star formation involves the collapse of a cloud (or part of a cloud) under gravity and the associated fragmentation of the cloud into smaller and smaller self-gravitating clumps (Hoyle, 1953). It has also been suggested, from observations of pre-protostellar clumps, that fragmentation may be linked to the creation of the initial mass function (IMF) of stars (Ward-Thompson et al., 2006; Carpenter et al., 2009). Both of these suppositions can only be supported if molecular clouds are not gravitationally bound.

Contemporary observational evidence suggesting that clouds are short-lived (Ballesteros-Paredes et al., 2006; Elmegreen, 2007; Kruijssen et al., 2019) and that star formation is prevented by stellar feedback (Rey-Raposo et al., 2016) and the effects of turbulence and magnetic fields (Price and Bate, 2008; Federrath, 2016) indicate that most molecular clouds are unbound. This is further supported by simulations of molecular cloud formation in spiral galaxies (Dobbs, Bonnell, and Pringle, 2006; Dobbs, Burkert, and Pringle, 2011) which suggest that only the internal star forming clumps are gravitationally bound whilst the molecular cloud itself is unbound.

F.1.1 Young Stellar Object classifications

During the initial stages of stellar development, a molecular cloud collapses, forming a protostar due to the in-fall of material from a circumstellar disk, or envelope. This protostar remains shrouded in an envelope of gas and dust and is only visible due to the excess infrared radiation given off by its surrounding envelope. As the gas and dust in the disk is used up the central YSO becomes visible and displays the black body spectrum typical of young stars whilst also exhibiting a decreasing infrared excess due to the envelope.

These different stages in development are characterised by changes in the spectrum of radiation given off. Submillimeter radiation from the gas cloud dominates the early stages of development. Intermediate stages emit strongly in the infrared through radiation from the disk whilst the later stages are observable in the optical and infrared. Lada (1987) developed a classification scheme for YSO's based on the spectral index (α) of a source, where α is the ratio of the bodies flux density to its wavelength in the near to mid-infrared spectrum, i.e.

$$\alpha = \frac{d\log_{10}(\lambda F_{\lambda})}{d\log_{10}(\lambda)} \quad \textbf{(F.2)}$$

where λ is the wavelength and F_{λ} is the flux density. Lada (1987) proposed three classes (I, II and III), whilst a fourth class (0) was subsequently added by (Andre, Ward-Thompson, and Barsony, 1993) following their observation of faint objects with strong submillimetre radiation at wavelengths below 10μm.

Figure F.2 shows this revised classification scheme as an evolutionary sequence for YSO's where deeply embedded Class 0 sources dissipate their circumstellar envelopes becoming Class I objects which eventually become optically visible as young pre-main-sequence stars.

Objects within Class II have circumstellar disks and correspond roughly to classical T Tauri stars (CTTS) with active disks, stellar jets and associated Herbig-Haro objects (Reipurth and Heathcote, 1997). Class III YSO's

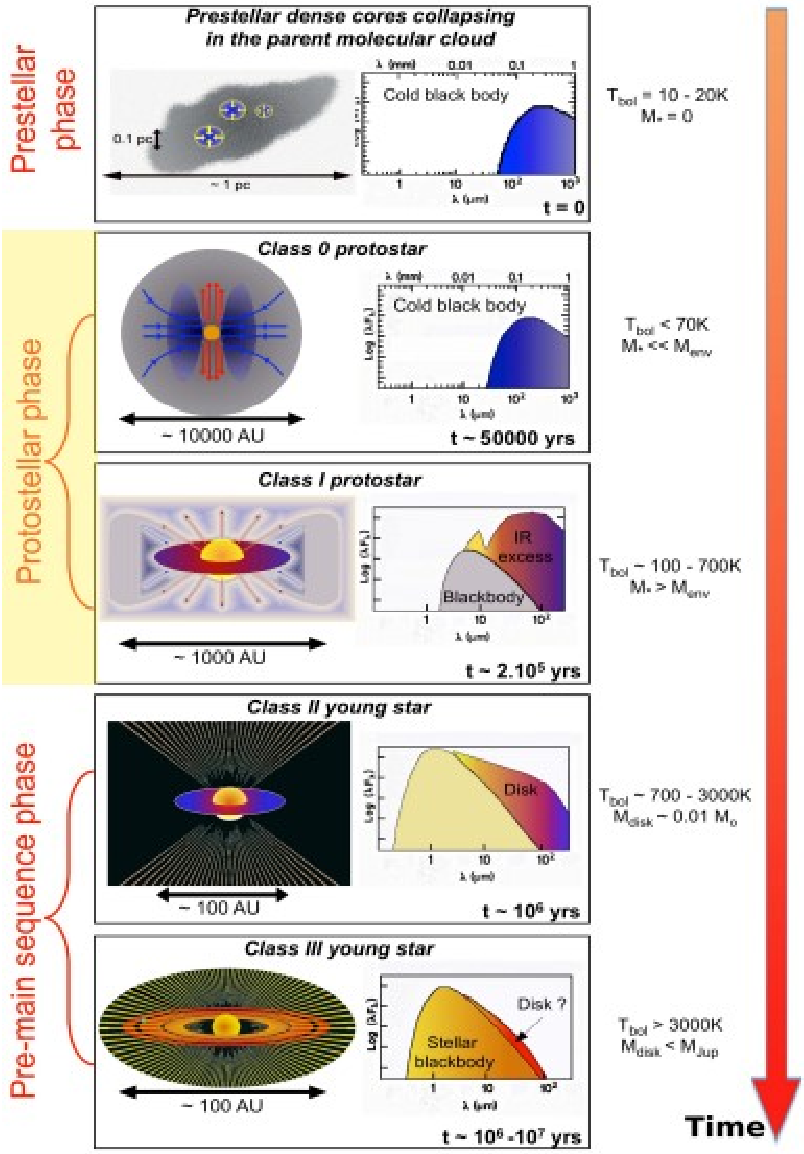

Figure F.2 The evolutionary development of YSO's from collapsing molecular cloud to pre-main sequence. Credit: From a presentation 'Roles and properties of magnetic fields from molecular clouds to protoplanetary disks' by Anaëlle Maury. Available at: http://sf2a.eu/semaine-sf2a/2018/presentations/S00/SF2A-MagneticFields-Anaelle-public.pdf.

corresponding approximately to weak-line T Tauri stars (WTTS) have begun nuclear fusion and are fragmenting their protoplanetary disks prior to the formation of planetary objects. Between the Class II and Class III objects lie transition disk objects (TDO's) which are gas-rich and optically thick but which have dust distributions with large central voids lacking in small dust grains. TDO's are thought to represent an evolutionary stage between Class II and Class III young stellar objects (Strom et al., 1989).

The TMC provides one of the best environments for the study of Class II and Class III objects in the infrared (e.g. Kenyon and Hartmann, 1995: and references therein).

F.2 Principles of Astrometric Measurements

The science of precisely measuring the position and movements of stars and other celestial objects is known as **astrometry**. The data provided through astrometric measurements can provide insights into the physical parameters and kinematics of astronomical objects.

Of particular interest to this study are the concepts of measuring distances through the use of parallax angles, the measurement of an objects proper motions through space and the precise location of an object in 3D space. For those unfamiliar with these astrometric concepts, and others, they are briefly discussed here.

F.2.1 Conventions for dating astrometric observations

When astrometric data are dependent upon a particular coordinate system for specifying their positional information, the reference date (or epoch) of that coordinate system needs to be specified. Celestial coordinate systems commonly used are the equatorial system and the ecliptic coordinate system.

Since an epoch is essentially a moment in time they can be specified in a number of different formats in relation to a given reference start date. Common formats are:

- **Julian date** (JD) is the continuous count of days since the beginning of the Julian Period (1st January 4713 BC). Julian dates are expressed as a Julian day number with a decimal fraction added[1]. For example, JD2433282.4235 for January 0.9235, 1950 Terrestrial Dynamic Time (TT).

- The **Besselian year** which is defined as starting when the mean Sun's longitude is precisely 280° which corresponds closely to 1st January, the start of the Gregorian calendar year (Meeus, 1991). For example, B1950.0 represents the instant January 0.9235, 1950 TT. This was the basic unit of the Besselian epoch which has now been superseded by,

- The **Julian epoch** which is a system of defining the date as a year with a decimal component. The base unit is the Julian year of 365.25 days. The prefix 'J' is used to distinguish this epoch from the earlier Besselian epoch. The standard Julian epoch is defined as

  $$\text{J2000.0} = \text{2000 January 1.5} = \text{2000 January 1 at 12 noon TDB}$$

  where TDB is the Barycentric Dynamic Time which is essentially the same as Terrestrial Dynamic Time except for relativistic corrections to move the origin to the solar system barycentre.

In 1976, the IAU decided that the standard epoch of J2000.0 should be adopted, starting in 1984 (Aoki et al., 1983). Before 1984, coordinate systems

[1] "XXIIIrd General Assembly Kyoto, Japan 1997 XXIIIe Assemblee Generale Kyoto, Japon"

dated to 1950 or 1900 were generally used. This international standardisation on a particular epoch enables all astronomers to collaborate effectively.

F.2.2 Parallax Measurements

Gaia is not designed to measure distances directly, but they can be inferred through the determination of stellar parallax.

In astrometric terms it is not possible to measure the distances to other stars using telescopes based on the Earth's surface. However, if we make two observations of the same star on opposites sides of the Earth's orbit we can get a noticeable angle between the star's apparent positions (Figure F.3).

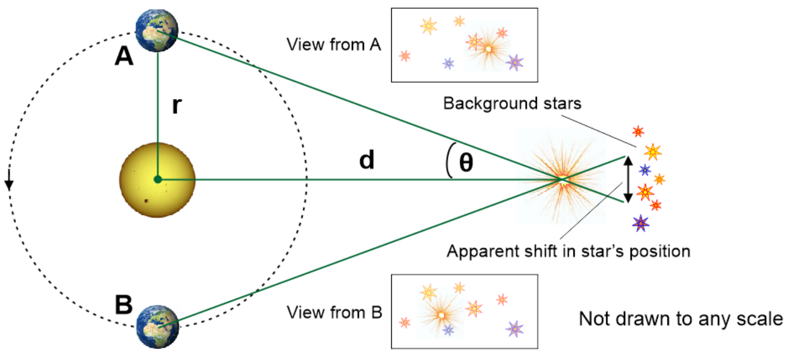

Figure F.3 Measurement of stellar parallax. Measuring a star's position once, and then again 6 months later and calculating the apparent change in position. The star's apparent motion is called stellar parallax (see text). Credit: Author, 2019.

Parallax is a measured difference in the apparent position of an object. Stellar parallax is most often measured using annual parallax i.e. through measuring a star's position once, and then again 6 months later and calculating the apparent change in position.

Using trigonometry we can now calculate the distance to the star such that, from Figure F.3

$$\tan\theta = \frac{r}{d} \quad \textbf{(F.3)}$$

where θ is the parallax angle p, *r* is 1 Astronomical Unit (AU), and *d* is the distance. On the assumption that any star is very far away we can say that $\tan$(p)=p, and the formula becomes

$$p = \frac{1AU}{d} \quad \text{or, rearranging} \quad d = \frac{1AU}{p} \quad \textbf{(F.4)}$$

It is more usual to use the parsec as a measure of distance and not the AU. The parsec is defined as the distance to a star that shows 1 arc-second of parallax angle. Our formula can therefore be re-written as

$$d = \frac{1}{p} \text{ parsecs} \quad \textbf{(F.5)}$$

where *p* is measured in arc-seconds and *d* is measured in parsecs (1 parsec ≏ 206265 AU).

In the context of *Gaia* parallax measurements, Luri et al. (2018) provides a full description of the issues involved in the estimation of distances from parallaxes and recommends that a full Bayesian approach be adopted when considering *Gaia* parallaxes. In general, observational errors in measured parallaxes, especially when the associated measurement uncertainties are large can lead to potentially strong biases requiring a full statistical treatment of the data and its uncertainties.

DR2 parallax uncertainties are in the range of up to 0.04 milli-arcseconds (mas) for sources with a broad-band, white-light magnitude (G) $<$15 and on the order of 0.7 mas at G$=$20. Coupled with proper motion measurements from DR2, a detailed investigation of the internal kinematics of the Taurus star-forming region can be made. Due to the relative proximity of the Taurus star-forming region, where the parallaxes are positive and relative uncertainties are small, a Bayesian prior is not employed in this study (Bailer-Jones, 2015; Bailer-Jones et al., 2018; Luri et al., 2018), and a straightforward inversion of parallax is used to infer distance (Equation F.5). This does not affect any of the conclusions in this paper.

Since it is known that there are unquantifiable (but probably small) parallax errors due to a poorly determined zero-point offset in extinction (Lindegren et al., 2018), it is not possible to correct individual *Gaia* parallax values completely. It should also be remembered that *Gaia* is, in essence, an optical telescope and, as such, will have difficulty in accurately measuring parallaxes in areas of high optical extinction due to dust. Hence, for the purposes of this study, mean parameter values are used. Independent comparisons of *Gaia* and VLBA studies of YSOs in the Ophiuchus, Serpens and Aquila regions (Ortiz-León et al., 2018) obtained consistent parallax values across all systems, supporting our use of uncorrected *Gaia* parallax values at this distance.

F.2.3 Measuring Proper Motion

The proper motion of an object has a magnitude and a direction and is a measure of the observable changes in the apparent positions of astronomical objects as seen against the background of more distant objects. In the equatorial coordinate system (see Appendix F.2.4), in any particular epoch (Appendix F.2.1), an objects proper motion is given in terms of its motion in right ascension (μRA or μ_α) and declination (μDec or μ_δ). The combination of these values gives the objects true proper motion (μ) typically measured in milli-arcseconds per year (mas yr^{-1}), using the relationship

$$\mu^2 = {\mu_\alpha}^2 + {\mu_\delta}^2 \qquad \textbf{(F.6)}$$

However, to find the true space velocity of an object we need to consider the individual vectors of that velocity.

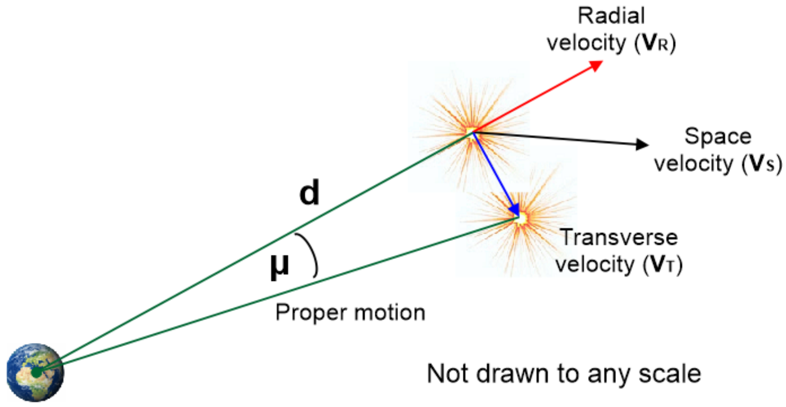

Figure F.4 Components of proper motion (see text) Credit: Author, 2019.

Figure F.4 identifies these component vectors. The space velocity of a star is defined by the components:

V_S = space velocity (the true total velocity of the star)
V_T = transverse velocity (velocity perpendicular to line of sight)
V_R = radial velocity (the line of sight velocity, i.e. the Doppler velocity)

through the Pythagorean relationship

$$V_S{}^2 = V_R{}^2 + V_T{}^2 \quad \textbf{(F.7)}$$

where V_T can be calculated by knowing the proper motion (μ) and the distance (d) derived from the objects parallax (Appendix F.2.2), using

$$V_T = 4.74\mu d \quad \textbf{(F.8)}$$

where V_T is in km s^{-1}, μ is in arcsec yr^{-1}, and d is the distance in parsecs.

Since an observer moves due to the Earth's rotation and revolution around the Sun, these motions have to be removed from the stellar radial velocity. This reduction step is called the heliocentric correction. Applying this correction removes the Earth's orbital velocity of 30 km s^{-1} and its rotational velocity of 0.5 km s^{-1} and provides the radial velocity of the observer relative to the observed object.

For a full determination of an objects proper motion it is necessary to take account of the Local Standard of Rest (LSR) radial velocity which corrects the heliocentric radial velocity to a value which would be seen in the Local rest frame once the Sun's peculiar motion has been removed.

Also, the Galactic Standard of Rest (GSR) radial velocity further corrects the stellar velocity for the LSR velocity projected on the line of sight and is interpreted as the velocity that a stationary observer in the Galactic rest frame would see at the position of the Sun.

F.2.4 Equatorial Coordinate System (RA & Dec)

In essence, the equatorial coordinate system is a projection of the land-based longitude and latitude system (Figure F.5) onto the Celestial Sphere.

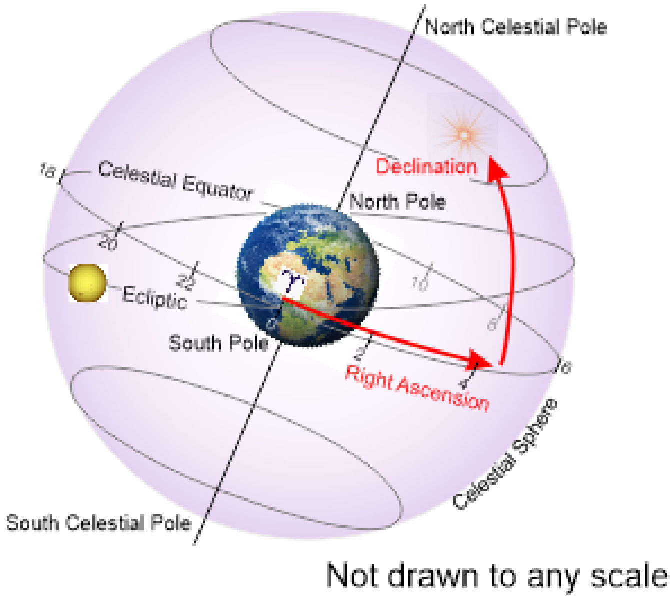

Figure F.5 Location around the celestial equator is measured as right ascension (RA or α) in hh:mm:ss starting from 0° at the vernal equinox and increasing from west to east. The distance from the celestial equator to a celestial pole is measured in degrees of declination (Dec or δ). Credit: Author, 2019.

By direct analogy, terrestrial lines of longitude have their equivalent in lines of right ascension (RA), measured in hours, minutes and seconds eastwards of a point where the celestial equator intersects the ecliptic (the vernal equinox or First Point of Aries, ♈), with one hour of RA = 15°. Terrestrial lines of latitude translate into celestial lines of declination (Dec), measured in degrees, arcminutes and arcseconds, indicating how far north or south of the celestial equator (a projection of the Earth's equator onto the celestial sphere) the object lies, with a minus sign indicating a measurement toward the celestial south pole.

F.2.5 Galactic Coordinate System (*l* & *b*)

The position of an object is measured in terms of its Galactic longitude (*l*) and its Galactic latitude (*b*) with the Galactic plane lying at *b* = 0°. Figure F.6 illustrates the system.

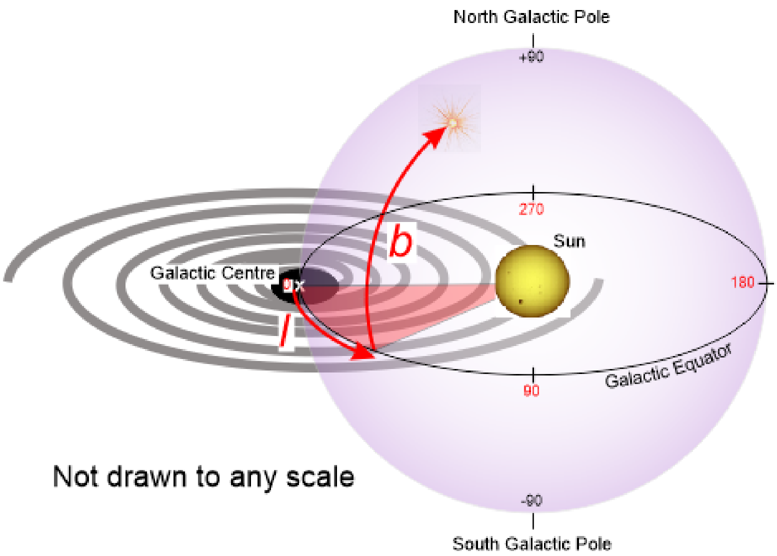

Figure F.6 Galactic coordinate system. Positions of objects are measured in terms of their galactic longitude (*l*) and galactic latitude (*b*). Credit: Author, 2019.

This coordinate system is heliocentric with its outer perimeter located at the Galactic centre, onto which Galactic longitude (*l*) and latitude (*b*) are projected. Galactic longitude ranges from 0° to 360° with the Galactic centre lying at l = 0° and increases anti-clockwise as viewed looking down from the North Galactic Pole (NGP). The galactic longitude *l* of an object is the angular distance around the Galactic equator from the Galactic centre. Galactic latitude ranges from +90° to -90°, above and below the galactic plane respectively.

F.2.6 Galactic Rectilinear Systems (xyz & UVW)

The Galactic rectilinear coordinate systems are heliocentric but are not projected onto the celestial sphere.

The xyz system is used to represent an objects 3-dimensional position in space as linear (Euclidean) distances, measured in parsecs, from the Sun and provides a true spatial frame of reference. As seen in Figure F.7, the x direction extends from the Sun through the galactic barycenter (galactic coordinates l = 0°, b = 0°) (e.g. Bobylev, 2010); the z-axis extends from the Sun through the NGP at b = 90°, and the y direction lies perpendicular to both the x and z axes in the direction of Galactic rotation (l = 90°, b = 0°).

The UVW system is a vector coordinate system which provides stellar velocities, in km s^{-1} relative to the Local Standard of Rest (LSR) - which is an imaginary position in a circular orbit in the Galaxies fundamental plane and co-moving with the average rotational speed of stars at the same distance as the Sun from the galactic centre. Figure F.7 shows how the xyz and UVW systems are co-incident. Since the UVW system

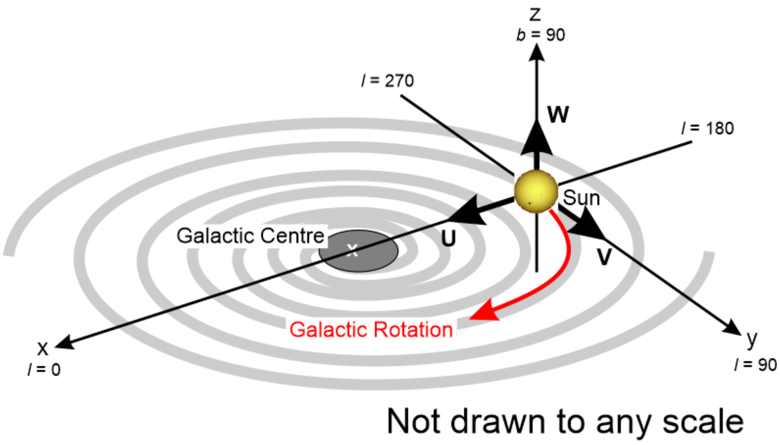

Figure F.7 The galactic xyz coordinate system representing linear distances and the corresponding UVW vector system of stellar velocities relative to the LSR. Only the positive directions of the UVW dimensions are shown in the figure. Credit: Author, 2019.

is a vector representation of an objects movement it does not have a central reference point. An object with zero velocity in U, V and W is moving in exactly the same direction and at the same speed as the LSR, but it can be located in any direction and at any distance from the Sun.

When using the UVW system it is important to specify which of two conventions are being used in determining the velocities. In one system, the U-axis is sighted **towards the galactic centre** (l = 0°) with positive towards the east and towards the north galactic pole (a right-handed system); in the other convention the U-axis is directed **toward the galactic anticenter** (l = 180°), with positive values towards the east and towards the north galactic pole, i.e. a left-handed system (e.g. Johnson and Soderblom, 1987).

Bibliography

Ainsworth, Rachael E et al. (2016). "A GMRT survey of regions towards the Taurus molecular cloud at 323 and 608 MHz". In: *Monthly Notices of the Royal Astronomical Society* 462(3), pp. 2904–2917.

Anders, Edward and Nicolas Grevesse (1989). "Abundances of the elements: Meteoritic and solar". In: *Geochimica et Cosmochimica acta* 53(1), pp. 197–214.

Andre, Philippe, Derek Ward-Thompson, and Mary Barsony (1993). "Submillimeter continuum observations of Rho Ophiuchi A-The candidate protostar VLA 1623 and prestellar clumps". In: *The Astrophysical Journal* 406, pp. 122–141.

Aoki, S et al. (1983). "Conversion matrix of epoch B 1950.0 FK 4-based positions of stars to epoch J 2000.0 positions in accordance with the new IAU resolutions". In: *Astronomy and Astrophysics* 128, pp. 263–267.

Arenou, F et al. (2018). "Gaia Data Release 2-Catalogue validation". In: *Astronomy and Astrophysics* 616, A17.

Babusiaux, Carine et al. (2018). "Gaia Data Release 2-Observational Hertzsprung-Russell diagrams". In: *Astronomy and Astrophysics* 616, A10.

Bailer-Jones, CAL et al. (2018). "Estimating distances from parallaxes IV: Distances to 1.33 billion stars in Gaia Data Release 2". In: *The Astronomical Journal* 156(58), p. 58.

Bailer-Jones, Coryn AL (2015). "Estimating distances from parallaxes". In: *Publications of the Astronomical Society of the Pacific* 127(956), p. 994.

Ballesteros-Paredes, Javier et al. (2006). "Molecular cloud turbulence and star formation". In: *arXiv preprint astro-ph/0603357*.

Bertout, Claude and Françoise Genova (2006). "A kinematic study of the Taurus-Auriga T association". In: *Astronomy and Astrophysics* 460(2), pp. 499–518.

Bertout, Claude, Noël Robichon, and Frédéric Arenou (1999). "Revisiting Hipparcos data for pre-main sequence stars". In: *Astronomy and Astrophysics* 352, pp. 574–586.

Bloemen, Hans (1987). "The High-Energy Component of the ISM—Cosmic-Ray Phenomena". In: *Interstellar Processes*. Springer, pp. 143–168.

Bobylev, Vadim V (2010). "Searching for stars closely encountering with the solar system". In: *Astronomy Letters* 36(3), pp. 220–226.

Bolatto, Alberto D, Mark Wolfire, and Adam K Leroy (2013). "The CO-to-H2 conversion factor". In: *Annual Review of Astronomy and Astrophysics* 51, pp. 207–268.

Bressan, A et al. (1993). "Evolutionary sequences of stellar models with new radiative opacities. II-Z= 0.02". In: *Astronomy and Astrophysics Supplement Series* 100, pp. 647–664.

Bressan, Alessandro et al. (2012). “PARSEC: stellar tracks and isochrones with the PAdova and TRieste Stellar Evolution Code”. In: *Monthly Notices of the Royal Astronomical Society* 427(1), pp. 127–145.

Briceno, Cesar et al. (1997). “X-rays surveys and the post-t tauri problem”. In: *The Astronomical Journal* 113, pp. 740–752.

Brown, AGA et al. (2018). “Gaia Data Release 2-Summary of the contents and survey properties”. In: *Astronomy and Astrophysics* 616, A1.

Brown, Anthony GA et al. (2016). “Gaia Data Release 1-Summary of the astrometric, photometric, and survey properties”. In: *Astronomy and Astrophysics* 595, A2.

Brown, Archibald (1950). “On the Determination of the Convergent Point of a Moving Cluster from Proper Motions.” In: *The Astrophysical Journal* 112, p. 225.

Bruijne, Jos HJ de (1999). “A refurbished convergent-point method for finding moving groups in the Hipparcos Catalogue”. In: *Monthly Notices of the Royal Astronomical Society* 306(2), pp. 381–393.

Butkevich, Alexey G and Lennart Lindegren (2014). “Rigorous treatment of barycentric stellar motion-Perspective and light-time effects in astrometric and radial velocity data”. In: *Astronomy and Astrophysics* 570, A62.

Canty, JI et al. (2013). “Towards precise ages and masses of free floating planetary mass brown dwarfs”. In: *Monthly Notices of the Royal Astronomical Society* 435(3), pp. 2650–2664.

Cardelli, Jason A, Geoffrey C Clayton, and John S Mathis (1989). “The relationship between infrared, optical, and ultraviolet extinction”. In: *The Astrophysical Journal* 345, pp. 245–256.

Carpenter, John et al. (2009). “Fragmentation in Molecular Clouds and the Origin of the Stellar Initial Mass Function”. In: *astro2010: The Astronomy and Astrophysics Decadal Survey*. Vol. 2010.

Caselli, Paola et al. (2012). “First detection of water vapor in a pre-stellar core”. In: *The Astrophysical Journal Letters* 759(2), p. L37.

Chamberlin, Donald D (2012). “Early history of SQL”. In: *IEEE Annals of the History of Computing* 34(4), pp. 78–82.

Clark, F. O., P. T. Giguere, and R. M. Crutcher (July 1977). “Radio observations of fragmentation and localized multiple velocity components in a group of dust clouds in Taurus”. In: *The Astrophysical Journal* 215, pp. 511–516. doi: 10.1086/155382.

Cropper, M et al. (2018). “Gaia Data Release 2-Gaia Radial Velocity Spectrometer”. In: *Astronomy and Astrophysics* 616, A5.

Cunha, D et al. (2013). “Impact of stellar companions on precise radial velocities”. In: *Astronomy & Astrophysics* 550, A75.

Dame, Thomas M, Dap Hartmann, and P Thaddeus (2001). “The Milky Way in molecular clouds: a new complete CO survey”. In: *The Astrophysical Journal* 547(2), p. 792.

Di Criscienzo, M, P Ventura, and F D'Antona (2009). "Updated pre-main sequence tracks at low metallicities for 0.1". In: *Astronomy & Astrophysics* 496(1), pp. 223–227.

di Francesco, J. et al. (2007). "An Observational Perspective of Low-Mass Dense Cores I: Internal Physical and Chemical Properties". In: *Protostars and Planets V*, pp. 17–32. eprint: astro-ph/0602379.

Dickman, Robert L (1978). "The ratio of carbon monoxide to molecular hydrogen in interstellar dark clouds". In: *The Astrophysical Journal Supplement Series* 37, pp. 407–427.

Dobbs, CL, A Burkert, and JE Pringle (2011). "Why are most molecular clouds not gravitationally bound?" In: *Monthly Notices of the Royal Astronomical Society* 413(4), pp. 2935–2942.

Dobbs, Clare L, IA Bonnell, and JE Pringle (2006). "The formation of molecular clouds in spiral galaxies". In: *Monthly Notices of the Royal Astronomical Society* 371(4), pp. 1663–1674.

Dobbs, Clare L et al. (2014). "Formation of molecular clouds and global conditions for star formation". In: *Protostars and Planets VI* 1312, pp. 3–26.

Downes, D and PM Solomon (1998). "Rotating nuclear rings and extreme starbursts in ultraluminous galaxies". In: *The Astrophysical Journal* 507(2), p. 615.

Ducourant, C et al. (2005). "Pre-main sequence star proper motion catalogue". In: *Astronomy and Astrophysics* 438(2), pp. 769–778.

Dunham, Michael M et al. (2015). "Young stellar objects in the Gould Belt". In: *The Astrophysical Journal Supplement Series* 220(1), p. 11.

Dzib, Sergio A et al. (2015). "The Gould's Belt Very Large Array Survey. IV. The Taurus-Auriga Complex". In: *The Astrophysical Journal* 801(2), p. 91.

Elias, JH (1978). "A study of the Taurus dark cloud complex". In: *The Astrophysical Journal* 224, pp. 857–872.

Elmegreen, Bruce G (2007). "On the rapid collapse and evolution of molecular clouds". In: *The Astrophysical Journal* 668(2), p. 1064.

Esplin, TL and KL Luhman (2017). "A Survey For Planetary-mass Brown Dwarfs in the Taurus and Perseus Star-forming Regions". In: *The Astronomical Journal* 154(4), p. 134.

Esplin, TL and KL Luhman (2019). "A Survey for New Members of Taurus from Stellar to Planetary Masses". In: *The Astronomical Journal* 158(2), p. 54.

Eyer, L et al. (2011). "From Hipparcos to Gaia". In: *Proceedings of the International Astronomical Union* 7(S285), pp. 153–157.

Federrath, Christoph (2016). "The role of turbulence, magnetic fields and feedback for star formation". In: *Journal of Physics: Conference Series*. Vol. 719. 1. IOP Publishing, p. 012002.

Feigelson, Eric and G Jogesh Babu (2013). *Beware the Kolmogorov-Smirnov test*.

Ferriere, Katia M (2001). "The interstellar environment of our galaxy". In: *Reviews of Modern Physics* 73(4), p. 1031.

Fleming, Graham D, Jason Matthew Kirk, and Derek Ward-Thompson (2019). "Revealing the TwoHorns' of Taurus with GAIA DR2". In: *arXiv preprint arXiv:1904.06980*.

Forestini, M (1994). "Low-mass stars: pre-main sequence evolution and nucleosynthesis". In: *Astronomy and Astrophysics* 285, pp. 473–488.

Freeman, A and TJ Millar (1983). "Formation of complex molecules in TMC-1". In: *Nature* 301(5899), p. 402.

Frink, S et al. (1997). "New proper motions of pre-main sequence stars in Taurus-Auriga". In: *Astronomy and Astrophysics* 325, pp. 613–622.

Gaia, Collaboration et al. (2018). "Gaia Data Release 2 Summary of the contents and survey properties". In: *Astronomy & Astrophysics* 616(1).

Galli, PAB et al. (2012). "A new method for calculating the convergent point of a moving group". In: *Astronomy & Astrophysics* 538, A23.

Galli, PAB et al. (2019). "Structure and kinematics of the Taurus star-forming region from Gaia-DR2 and VLBI astrometry". In: *Astronomy and Astrophysics* 630, A137.

Galli, Phillip AB et al. (2018). "The Gould's Belt Distances Survey (GOBELINS). IV. Distance, Depth, and Kinematics of the Taurus Star-forming Region". In: *The Astrophysical Journal* 859(1), p. 33.

Generale, XXIIIe Assemblee. "XXIIIrd General Assembly Kyoto, Japan 1997 XXIIIe Assemblee Generale Kyoto, Japon". In: ().

Ghez, AM, G Neugebauer, and K Matthews (1993). "The multiplicity of T Tauri stars in the star forming regions Taurus-Auriga and Ophiuchus-Scorpius: A 2.2 micron speckle imaging survey". In: *Astronomical Journal* 106(5), pp. 2005–2023.

Girardi, Léo et al. (2008). "Revised bolometric corrections and interstellar extinction coefficients for the ACS and WFPC2 photometric systems". In: *Publications of the Astronomical Society of the Pacific* 120(867), p. 583.

Goldsmith, P. F. et al. (June 2008). "Large-Scale Structure of the Molecular Gas in Taurus Revealed by High Linear Dynamic Range Spectral Line Mapping". In: *The Astrophysical Journal* 680, pp. 428–445. doi: 10.1086/587166. arXiv: 0802.2206.

Gomez, M et al. (1992). "On the ages of pre-main-sequence stars in Taurus". In: *The Astronomical Journal* 104, pp. 762–773.

Gomez, M et al. (1993). "On the spatial distribution of pre-main-sequence stars in Taurus". In: *The Astronomical Journal* 105, pp. 1927–1937.

Gontcharov, GA (2016). "Interstellar Extinction". In: *Astrophysics* 59(4), pp. 548–579.

Gonthier, PL (2005). *Radio-loud and radio-quiet gamma-ray pulsars from the Galactic plane and the Gould Belt*. Tech. rep. Stanford Linear Accelerator Center (SLAC), Menlo Park, CA.

Goodwin, Simon P, Ant P Whitworth, and Derek Ward-Thompson (2004). "An explanation for the unusual IMF in Taurus". In: *Astronomy and Astrophysics* 419(2), pp. 543–547.

Gouliermis, Dimitrios A et al. (2006). “The Star-forming Region NGC 346 in the Small Magellanic Cloud with Hubble Space Telescope ACS Observations. I. Photometry”. In: *The Astrophysical Journal Supplement Series* 166(2), p. 549.

Grosso, Nicolas et al. (2007). “X-ray emission from the young brown dwarfs of the Taurus Molecular Cloud”. In: *Astronomy and Astrophysics* 468(2), pp. 391–403.

Gudel, M, Deborah L Padgett, and Catherine Dougados (2007). “The Taurus molecular cloud: Multiwavelength surveys with XMM-Newton, the Spitzer Space telescope, and the Canada-France-Hawaii telescope”. In: *Protostars and planets V*, pp. 329–344.

Güdel, Manuel, Deborah L Padgett, and Catherine Dougados (2006). “The Taurus Molecular Cloud: Multi-Wavelength Surveys with XMM-Newton, the Spitzer Space Telescope, and CFHT”. In: *arXiv preprint astro-ph/0609520*.

Güdel, Manuel et al. (2007). “The XMM-Newton extended survey of the Taurus molecular cloud (XEST)”. In: *Astronomy & Astrophysics* 468(2), pp. 353–377.

Hacar, A et al. (2013). “Cores, filaments, and bundles: hierarchical core formation in the L1495/B213 Taurus region”. In: *Astronomy and Astrophysics* 554, A55.

Hartigan, John A, Pamela M Hartigan, et al. (1985). “The dip test of unimodality”. In: *The Annals of Statistics* 13(1), pp. 70–84.

Hartigan, Patrick and Scott J Kenyon (2003). “A spectroscopic survey of subarcsecond binaries in the Taurus-Auriga dark cloud with the Hubble Space Telescope”. In: *The Astrophysical Journal* 583(1), p. 334.

Hartmann, L et al. (1991). “A proper motion survey for pre-main-sequence stars in Taurus-Auriga”. In: *The Astronomical Journal* 101, pp. 1050–1062.

Hartmann, Lee (2002). “Flows, fragmentation, and star formation. I. Low-mass stars in Taurus”. In: *The Astrophysical Journal* 578(2), p. 914.

Heiles, C. and G. Katz (Jan. 1976). “The absence of systematic kinematics in dust clouds”. In: *The Astronomical Journal* 81, pp. 37–44. doi: 10.1086/111850.

Herbig, George H (1952). “Emission-line stars in galactic nebulosities”. In: *Journal of the Royal Astronomical Society of Canada* 46, p. 222.

Herbig, GH, FJ Vrba, and AE Rydgren (1986). “A spectroscopic survey of the Taurus-Auriga dark clouds for pre-main-sequence stars having Ca II H, K emission”. In: *The Astronomical Journal* 91, pp. 575–582.

Herbst, W and VS Shevchenko (1999). “A photometric catalog of Herbig Ae/Be stars and discussion of the nature and cause of the variations of UX Orionis stars”. In: *The Astronomical Journal* 118(2), p. 1043.

Herczeg, Gregory J and Lynne A Hillenbrand (2014). “An optical spectroscopic study of T Tauri stars. I. Photospheric properties”. In: *The Astrophysical Journal* 786(2), p. 97.

Hernández, Jesús et al. (2004). “Spectral analysis and classification of Herbig Ae/Be stars”. In: *The Astronomical Journal* 127(3), p. 1682.

Heyer, Mark and TM Dame (2015). “Molecular clouds in the milky way”. In: *Annual Review of Astronomy and Astrophysics* 53, pp. 583–629.

Hou, Wen et al. (2015). “A large sample of metallic-line star candidates from LAMOST Data Release 1”. In: *Monthly Notices of the Royal Astronomical Society* 449(2), pp. 1401–1407.

Hoyle, Fred (1953). “On the Fragmentation of Gas Clouds Into Galaxies and Stars.” In: *The Astrophysical Journal* 118, p. 513.

Johnson, Dean RH and David R Soderblom (1987). “Calculating galactic space velocities and their uncertainties, with an application to the Ursa Major group”. In: *The Astronomical Journal* 93, pp. 864–867.

Jones, BF and GH Herbig (1979). “Proper motions of T Tauri variables and other stars associated with the Taurus-Auriga dark clouds”. In: *The Astronomical Journal* 84, pp. 1872–1889.

Katz, D and AGA Brown (2017). “Gaia: on the road to DR2”. In: *arXiv preprint arXiv:1710.10816*.

Kazarovets, EV et al. (2017). “General catalogue of variable stars: Version GCVS 5.1”. In: *Astronomy Reports* 61(1), pp. 80–88.

Kenyon, Scott J, Mercedes Gomez, and Barbara A Whitney (2008). “Low Mass Star Formation in the Taurus-Auriga Clouds”. In: *arXiv preprint arXiv:0810.1298*.

Kenyon, Scott J and Lee Hartmann (1995). “Pre-main-sequence evolution in the Taurus-Auriga molecular cloud”. In: *The Astrophysical Journal Supplement Series* 101, p. 117.

Kenyon, Scott J et al. (1994). “New pre-main-sequence stars in the Taurus-Auriga molecular cloud”. In: *The Astronomical Journal* 108, pp. 251–261.

Kenyon, SJ, M Gómez, and BA Whitney (2008). “Handbook of Star Forming Regions, Vol. I, ed”. In: *B. Reipurth (San Francisco, CA: ASP)* 405.

Kirk, Jason Matthew et al. (2013). “First results from the Herschel Gould Belt Survey in Taurus”. In: *Monthly Notices of the Royal Astronomical Society* 432(2), pp. 1424–1433.

Kolmogorov, Andrey (1933). “Sulla determinazione empirica di una lgge di distribuzione”. In: *Giornale dell’Istituto Italiano degli Attuari* 4, pp. 83–91.

König, B, R Neuhäuser, and B Stelzer (2001). “X-ray emission of multiple T Tauri stars in Taurus”. In: *Astronomy & Astrophysics* 369(3), pp. 971–980.

Könyves, V et al. (2007). “Catalogue of far-infrared loops in the Galaxy”. In: *Astronomy and Astrophysics* 463(3), pp. 1227–1234.

Kraus, Adam L et al. (2017). “The Greater Taurus–Auriga Ecosystem. I. There is a Distributed Older Population”. In: *The Astrophysical Journal* 838(2), p. 150.

Kroupa, Pavel (2001). “On the variation of the initial mass function”. In: *Monthly Notices of the Royal Astronomical Society* 322(2), pp. 231–246.

Kroupa, Pavel (2002). “The initial mass function of stars: evidence for uniformity in variable systems”. In: *Science* 295(5552), pp. 82–91.

Kruijssen, JM Diederik et al. (2019). “Fast and inefficient star formation due to short-lived molecular clouds and rapid feedback”. In: *Nature* 569(7757), p. 519.

Lada, Charles J (1987). “Star formation: from OB associations to protostars”. In: *Symposium-International astronomical union*. Vol. 115. Cambridge University Press, pp. 1–18.

Li, Chengdong, Gang Zhao, and Chengqun Yang (2019). “Galactic Rotation and the Oort Constants in the Solar Vicinity”. In: *The Astrophysical Journal* 872(2), p. 205.

Li, D. and P. F. Goldsmith (Sept. 2012). “Is the Taurus B213 Region a True Filament?: Observations of Multiple Cyanoacetylene Transitions”. In: *The Astrophysical Journal* 756, 12, p. 12. doi: 10.1088/0004-637X/756/1/12. arXiv: 1207.0044.

Lindegren, L and MAC Perryman (1996). “GAIA: Global astrometric interferometer for astrophysics”. In: *Astronomy and Astrophysics Supplement Series* 116(3), pp. 579–595.

Lindegren, L et al. (2018). “Gaia Data Release 2-The astrometric solution”. In: *Astronomy and Astrophysics* 616, A2.

Lindegren, Lennart (2005). “The astrometric instrument of Gaia: Principles”. In: *The three-dimensional universe with Gaia*. Vol. 576, p. 29.

Loinard, Laurent (2012). “The Gould’s Belt Distances Survey”. In: *Proceedings of the International Astronomical Union* 8(S289), pp. 36–43.

Loinard, Laurent et al. (2007). “VLBA determination of the distance to nearby star-forming regions. I. The distance to T Tauri with 0.4% accuracy”. In: *The Astrophysical Journal* 671(1), p. 546.

Long, Feng et al. (2018). “Gaps and Rings in an ALMA Survey of Disks in the Taurus Star-forming Region”. In: *The Astrophysical Journal* 869(1), p. 17.

Luhman, KL (2018). “The Stellar Membership of the Taurus Star-forming Region”. In: *The Astronomical Journal* 156(6), p. 271.

Luhman, KL et al. (2006). “A survey for new members of Taurus with the Spitzer Space Telescope”. In: *The Astrophysical Journal* 647(2), p. 1180.

Luhman, KL et al. (2009a). “An Infrared/X-Ray Survey for New Members of the Taurus Star-Forming Region”. In: *The Astrophysical Journal* 703(1), p. 399.

Luhman, KL et al. (2009b). “The disk population of the Taurus star-forming region”. In: *The Astrophysical Journal Supplement Series* 186(1), p. 111.

Luri, Xavier et al. (2018). “Gaia Data Release 2: using Gaia parallaxes”. In: *Astronomy and Astrophysics* 616(A9), A9.

Lynds, Beverly T (1962). “Catalogue of Dark Nebulae.” In: *The Astrophysical Journal Supplement Series* 7, p. 1.

Malinen, Johanna et al. (2012). “Profiling filaments: comparing near-infrared extinction and submillimetre data in TMC-1”. In: *Astronomy and Astrophysics* 544, A50.

Manara, Carlo Felice et al. (2018). “Gaia DR2 view of the Lupus V–VI clouds: The candidate diskless young stellar objects are mainly background contaminants”. In: *Astronomy & Astrophysics* 615, p. L1.

Marsh, KA et al. (2016). “A census of dense cores in the Taurus L1495 cloud from the Herschel Gould Belt Survey”. In: *Monthly Notices of the Royal Astronomical Society* 459(1), pp. 342–356.

Martinavarro Armengol, S (2015). “A Herschel study of AGB stars in the Milky Way”. PhD thesis. UCL (University College London).

Maurus, Samuel and Claudia Plant (2016). “Skinny-dip: Clustering in a Sea of Noise”. In: *Proceedings of the 22nd ACM SIGKDD international conference on Knowledge discovery and data mining*. ACM, pp. 1055–1064.

McCuskey, SW (1939). “The Galactic Structure in Taurus. II. The Space Distribution of the Stars.” In: *The Astrophysical Journal* 89, p. 568.

Meeus, Jean H (1991). *Astronomical algorithms*. Willmann-Bell, Incorporated.

Meistas, E and V Straizys (1981). “Interstellar extinction in the Taurus dark clouds. II”. In: *Acta Astronomica* 31, pp. 85–91.

Mignard, François et al. (2018). “Gaia Data Release 2-The celestial reference frame (Gaia-CRF2)”. In: *Astronomy and Astrophysics* 616, A14.

Mizuno, A and Y Fukui (2004). “Milky Way Surveys: The Structure and Evolution of our Galaxy (ASP Conf. Ser. 317)”. PhD thesis. ed. D. Clemens, R. Shah & T. Brainerd (San Francisco, CA: ASP) 59.

Monnier, JD et al. (2008). “Discovery of a circumbinary disk around herbig Ae/Be system V892 tauri”. In: *The Astrophysical Journal Letters* 681(2), p. L97.

Mooley, Kunal et al. (2013). “B-and A-type Stars in the Taurus-Auriga Star-forming Region”. In: *The Astrophysical Journal* 771(2), p. 110.

Mora, A et al. (2001). “EXPORT: Spectral classification and projected rotational velocities of Vega-type and pre-main sequence stars”. In: *Astronomy & Astrophysics* 378(1), pp. 116–131.

Mora, A et al. (2014). “Gaia on-board metrology: basic angle and best focus”. In: *Space Telescopes and Instrumentation 2014: Optical, Infrared, and Millimeter Wave*. Vol. 9143. International Society for Optics and Photonics, p. 91430X.

Nanni, Ambra et al. (2013). “Evolution of thermally pulsing asymptotic giant branch stars–II. Dust production at varying metallicity”. In: *Monthly Notices of the Royal Astronomical Society* 434(3), pp. 2390–2417.

Nanni, Ambra et al. (2014). “Evolution of thermally pulsing asymptotic giant branch stars–III. Dust production at supersolar metallicities”. In: *Monthly Notices of the Royal Astronomical Society* 438(3), pp. 2328–2340.

Narayanan, Gopal et al. (2008). “The five college radio astronomy observatory CO mapping survey of the Taurus molecular cloud”. In: *The Astrophysical Journal Supplement Series* 177(1), p. 341.

Nguyen, Duy Cuong et al. (2012). “Close companions to young stars. I. A large spectroscopic survey in Chamaeleon I and Taurus-Auriga”. In: *The Astrophysical Journal* 745(2), p. 119.

Nutter, D et al. (2008). “SCUBA and Spitzer observations of the Taurus molecular cloud–pulling the bull’s tail”. In: *Monthly Notices of the Royal Astronomical Society* 384(2), pp. 755–763.

Ochsenbein, Francois and Pascal Dubois (1992). “Object classification in Simbad”. In: *European Southern Observatory Conference and Workshop Proceedings*. Vol. 43, p. 405.

O’Donnell, James E (1994). “Rnu-dependent optical and near-ultraviolet extinction”. In: *The Astrophysical Journal* 422, pp. 158–163.

Oh, Semyeong et al. (2017). “Comoving stars in gaia dr1: An abundance of very wide separation comoving pairs”. In: *The Astronomical Journal* 153(6), p. 257.

Oliveira, Isa et al. (2009). “Optical characterization of a new young stellar population in the Serpens molecular cloud”. In: *The Astrophysical Journal* 691(1), p. 672.

Olling, Rob P and Walter Dehnen (2003). “The Oort constants measured from proper motions”. In: *The Astrophysical Journal* 599(1), p. 275.

Oort, Jan H et al. (1927). “Observational evidence confirming Lindblad’s hypothesis of a rotation of the galactic system”. In: *Bulletin of the Astronomical Institutes of the Netherlands* 3, p. 275.

Ortiz, Inaki et al. (2008). “Ivoa astronomical data query language version 2.0”. In: *IVOA Recommendation* 20081030.

Ortiz-León, Gisela N et al. (2017). “THE GOULD’S BELT DISTANCES SURVEY (GOBELINS). I. TRIGONOMETRIC PARALLAX DISTANCES AND DEPTH OF THE OPHIUCHUS COMPLEX”. In: *The Astrophysical Journal* 834(2), p. 141.

Ortiz-León, Gisela N et al. (2018). “Gaia-DR2 Confirms VLBA Parallaxes in Ophiuchus, Serpens, and Aquila”. In: *Astrophysical Journal Letters* 869(2), p. L33.

Osuna, Pedro et al. (2008). “IVOA Astronomical Data Query Language Version 2.00”. In: *IVOA Recommendation* 30.

Palmeirim, P. et al. (Feb. 2013). “Herschel view of the Taurus B211/3 filament and striations: evidence of filamentary growth?” In: *Astronomy and Astrophysics* 550, A38, A38. doi: 10.1051/0004-6361/201220500. arXiv: 1211.6360 [astro-ph.SR].

Panopoulou, Georgia Virginia et al. (2014). “13CO filaments in the Taurus molecular cloud”. In: *Monthly Notices of the Royal Astronomical Society* 444(3), pp. 2507–2524.

Papadopoulos, Padelis P et al. (2012). “The Molecular Gas in Luminous Infrared Galaxies. II. Extreme Physical Conditions and Their Effects on the X co Factor”. In: *The Astrophysical Journal* 751(1), p. 10.

Patterer, Robert J et al. (1993). “Lithium line variations in weak-lined T Tauri stars”. In: *The Astronomical Journal* 105, pp. 1519–1524.

Paxton, Bill et al. (2010). “Modules for experiments in stellar astrophysics (MESA)”. In: *The Astrophysical Journal Supplement Series* 192(1), p. 3.

Peacock, JA (1983). “Two-dimensional goodness-of-fit testing in astronomy”. In: *Monthly Notices of the Royal Astronomical Society* 202(3), pp. 615–627.

Péricaud, J et al. (2017). “The hybrid disks: a search and study to better understand evolution of disks”. In: *Astronomy & Astrophysics* 600, A62.

Perryman, M et al. (1997). “The HIPPARCOS catalogue”. In:

Pietrinferni, Adriano et al. (2013). “The BaSTI Stellar Evolution Database: models for extremely metal-poor and super-metal-rich stellar populations”. In: *Astronomy & Astrophysics* 558, A46.

Price, Daniel J and Matthew R Bate (2008). “The effect of magnetic fields on star cluster formation”. In: *Monthly Notices of the Royal Astronomical Society* 385(4), pp. 1820–1834.

Prusti, Timo et al. (2016). “The gaia mission”. In: *Astronomy and Astrophysics* 595, A1.

Qian, Lei, Di Li, and Paul F Goldsmith (2012). “13CO cores in the Taurus molecular cloud”. In: *The Astrophysical Journal* 760(2), p. 147.

Rebull, LM et al. (2010). “The Taurus Spitzer survey: new candidate Taurus members selected using sensitive mid-infrared photometry”. In: *The Astrophysical Journal Supplement Series* 186(2), p. 259.

Reipurth, Bo and Steve Heathcote (1997). “50 Years of Herbig-Haro Research: From Discovery to HST”. In: *Symposium-International Astronomical Union*. Vol. 182. Cambridge University Press, pp. 3–18.

Rey-Raposo, Ramon et al. (2016). “The roles of stellar feedback and galactic environment in star-forming molecular clouds”. In: *Monthly Notices of the Royal Astronomical Society* 464(3), pp. 3536–3551.

Riello, Marco et al. (2018). “Gaia Data Release 2-Processing of the photometric data”. In: *Astronomy and Astrophysics* 616, A3.

Rivière-Marichalar, Pablo et al. (2012). “Detection of warm water vapour in Taurus protoplanetary discs by Herschel”. In: *Astronomy and Astrophysics* 538, p. L3.

Rizzuto, Aaron C et al. (2020). “Dynamical Masses of Young Stars. II. Young Taurus Binaries Hubble 4, FF Tau, and HP Tau/G3”. In: *The Astrophysical Journal* 889(2), p. 175.

Romero, Gisela A et al. (2012). “The nature of transition circumstellar disks. II. Southern molecular clouds”. In: *The Astrophysical Journal* 749(1), p. 79.

Salgado, Jesús et al. (2017). “The ESA gaia archive: Data release 1”. In: *Astronomy and computing* 21, pp. 22–26.

Scelsi, L et al. (2007). “Coronal abundances of X-ray bright pre-main sequence stars in the Taurus molecular cloud”. In: *Astronomy and Astrophysics* 473(2), pp. 589–601.

Schmalzl, Markus et al. (2010). “Star formation in the Taurus filament L 1495: From dense cores to stars”. In: *The Astrophysical Journal* 725(1), p. 1327.

Schneider, N et al. (2011). “The link between molecular cloud structure and turbulence”. In: *Astronomy and Astrophysics* 529, A1.

Schönrich, Ralph, James Binney, and Walter Dehnen (2010). “Local kinematics and the local standard of rest”. In: *Monthly Notices of the Royal Astronomical Society* 403(4), pp. 1829–1833.

Shafranovich, Yakov (2005). “Common format and MIME type for CSV files”. In: *Internet Eng. Task Force draft, Mar*.

Sheehan, Patrick D and Josh A Eisner (2017). “Disk Masses for Embedded Class I Protostars in the Taurus Molecular Cloud”. In: *arXiv preprint arXiv:1712.02378*.

Shimajiri, Y et al. (2019). “Probing accretion of ambient cloud material into the Taurus B211/B213 filament”. In: *Astronomy and Astrophysics* 623, A16.

Simon, M, AM Ghez, and Ch Leinert (1993). “Multiplicity and the ages of the stars in the Taurus star-forming region”. In: *The Astrophysical Journal* 408, pp. L33–L36.

Skiff, BA (2010). “Lowell Observatory”. In: *General Catalogue of Stellar Spectral Classifications ftp://cdsarc. u-strasbg. fr/pub/cats/B/mk*.

Slesnick, Catherine L et al. (2006). “A distributed population of low-mass pre-main-sequence stars near the Taurus molecular clouds”. In: *The Astronomical Journal* 132(6), p. 2665.

Soderblom, David R et al. (2014). “Ages of young stars”. In: *Protostars and Planets VI* 3(1).

Solomon, PM et al. (1987). “Mass, luminosity, and line width relations of Galactic molecular clouds”. In: *The Astrophysical Journal* 319, pp. 730–741.

Soma, Tatsuya et al. (2018). “Complex Organic Molecules in Taurus Molecular Cloud-1”. In: *The Astrophysical Journal* 854(2), p. 116.

Spada, F et al. (2017). “The Yale–Potsdam Stellar Isochrones”. In: *The Astrophysical Journal* 838(2), p. 161.

Stephens, Michael A (1974). “EDF statistics for goodness of fit and some comparisons”. In: *Journal of the American statistical Association* 69(347), pp. 730–737.

Straizys, V and E Meistas (1980). “Interstellar extinction in the dark Taurus clouds. I”. In: *Acta Astronomica* 30, pp. 541–552.

Strom, Karen M et al. (1989). “Circumstellar material associated with solar-type pre-main-sequence stars-A possible constraint on the timescale for planet building”. In: *The Astronomical Journal* 97, pp. 1451–1470.

Sun, Ke-Feng et al. (2003). “Large-scale distribution of Herbig-Haro objects in Taurus”. In: *Chinese Journal of Astronomy and Astrophysics* 3(5), p. 458.

Takita, Satoshi et al. (2010). “A survey of T Tauri stars with AKARI towards the Taurus-Auriga region”. In: *Astronomy & Astrophysics* 519, A83.

Torres, Rosa M et al. (2007). “VLBA determination of the distance to nearby star-forming regions. II. Hubble 4 and HDE 283572 in Taurus”. In: *The Astrophysical Journal* 671(2), p. 1813.

Torres, Rosa M et al. (2009). “VLBA determination of the distance to nearby star-forming regions. III. HP Tau/G2 and the three-dimensional structure of Taurus”. In: *The Astrophysical Journal* 698(1), p. 242.

Tóth, LV et al. (2004). “Very cold cores in the Taurus Molecular Ring as seen by ISO”. In: *Astronomy and Astrophysics* 420(2), pp. 533–546.

Tout, Christopher A, Mario Livio, and Ian A Bonnell (1999). “The ages of pre-main-sequence stars”. In: *Monthly Notices of the Royal Astronomical Society* 310(2), pp. 360–376.

Trümper, J (1985). “X-ray sky surveys and the ROSAT mission”. In: *Bulletin d’Information du Centre de Donnees Stellaires* 28, p. 81.

Van Rossum, Guido et al. (2007). “Python Programming Language.” In: *USENIX annual technical conference*. Vol. 41, p. 36.

Walter, FM et al. (1987). “X-ray sources in regions of star formation. II-The pre-main-sequence G star HDE 283572”. In: *The Astrophysical Journal* 314, pp. 297–307.

Ward-Thompson, Derek et al. (2006). “An observational perspective of low mass dense cores II: Evolution towards the initial mass function”. In: *arXiv preprint astro-ph/0603474*.

Weiler, Michael (2018). “Revised Gaia Data Release 2 passbands”. In: *Astronomy & Astrophysics* 617, A138.

Whittet, DCB et al. (2004). “The ultraviolet extinction curve of intraclump dust in Taurus (TMC-1): constraints on the 2175 Å bump absorber”. In: *The Astrophysical Journal* 602(1), p. 291.

Xiao, Hong Yu et al. (2012). “A Census of Rotation and Variability in L1495: A Uniform Analysis of Trans-atlantic Exoplanet Survey Light Curves for Pre-main-sequence Stars in Taurus”. In: *The Astrophysical Journal Supplement Series* 202(1), p. 7.

Xu, Shuangjing et al. (2019). “Comparison of Gaia DR2 Parallaxes of Stars with VLBI Astrometry”. In: *The Astrophysical Journal* 875(2), p. 114.

Zhang, Zhoujian et al. (2018). “The Pan-STARRS1 Proper-motion Survey for Young Brown Dwarfs in Nearby Star-forming Regions. I. Taurus Discoveries and a Reddening-free Classification Method for Ultracool Dwarfs”. In: *The Astrophysical Journal* 858(1), p. 41.

Zuckerman, B and NJ Evans (1974). “Models of massive molecular clouds”. In: *The Astrophysical Journal* 192, pp. L149–L152.